Thèse n° 4191

THÈSE

présentée à

L'UNIVERSITÉ BORDEAUX 1

par Silke Hey

pour obtenir le grade de

DOCTEUR

Mention: Sciences physiques et de l'Ingénieur

Spécialité: Lasers, matière, nanosciences

Thermothérapies guidées par IRM : développements méthodologiques en thermométrie par IRM et méthodes d'asservissement automatique

Soutenue le: 10 décembre 2010

Devant la Commision d'examen formée de:

M. Luc Darrasse, Directeur de Recherche CNRS	Rapporteur
M. Emmanuel Barbier, Chargé de Recherche INSERM	Rapporteur
M. Bertrand Audoin, Professeur CNRS	Examinateur
Mme. Jenny Benois-Pineau, Professeure CNRS	Examinateur
M. Jean-Michel Franconi, Professeur CNRS	Examinateur

Directeur de thèse: M. Chrit Moonen, Directeur de Recherche CNRS

Imagerie Moléculaire et Fonctionnelle :
de la Physiologie la Thérapie (IMF)
UMR 5231/Universit Bordeaux 2
146, rue Lo Saignat
Case 117
33076 Bordeaux Cedex
France

Resumé

Les ultrasons focalisés de haute intensité (HIFU) guidés par IRM et combinés à la thermométrie basée sur la fréquence de résonance du proton (PRF) sont une technique prometteuse pour l'ablation non invasive de tumeurs, le dépôt local de médicaments et l'activation des transgènes. Ce travail présente de nouveaux développements dans le domaine de la thermométrie PRF en présence de mouvement physiologique périodique associé aux variations du champ magnétique. De nouvelles stratégies de correction sont proposées et exploitent la méthode multi-baseline établie en incluant un modèle de variation de phase. Elles sont illustrées avec des exemples de thermométrie dans le sein et dans le cœur humain. De plus, d'autres facteurs influençant la thermométrie PRF, notamment la présence de graisse dans le sein et le flux sanguin dans le cœur, sont étudiés. Dans la seconde partie de ce travail a été abordée la problématique du contrôle précis de la température. Une première approche propose un algorithme de contrôle proportionel, intégral et dérivatif (PID) amélioré utilisant des paramètres de contrôle adaptatifs. En étendant ce concept à un contrôle 3D de la température, une implémentation de chauffage volumétrique est proposée. Par ailleurs, une nouvelle méthode de repositionnement dynamique de la coupe d'imagerie permet de fournir des informations volumétriques sur l'anatomie et la température en temps réel. La combinaison avec la compensation 2D de mouvement et l'adaptation du faisceau ultrasonore permet la réalisation d'un chauffage volumétrique suivant une courbe de température ou de dose thermique prédéfinie qui fonctionne même en présence de mouvements.

Mots clés: thermométrie PRF, ultrasons focalisés, contrôle de la température, PID

MRI guided thermotherapies: Advances in MR thermometry and feedback control methods

Summary

MR-guided high-intensity focused ultrasound (HIFU) using proton resonance frequency (PRF) based thermometry is a promising technique for non-invasive ablations in tumor therapy as well as for targeted drug delivery and the activation of transgenes. This work presents further developments in the field of PRF thermometry in the presence of periodical physiological motion and the associated magnetic field variations. Using the examples of thermometry in the human breast and the human heart, new correction strategies are presented which extend the established multi-baseline phase correction to include a model of the phase variation and external sensor readings from a pencil-beam navigator. In addition further factors, namely the presence of fat in the breast and blood flow in the heart influencing the performance of MR thermometry in these organs are examined.

In the second part of this work, the issue of precise temperature control has been approached in two ways. First, an improved proportional, integral and derivative (PID) controller using adaptive control parameters is developed. By expanding the concept of temperature control to 3D, an implementation of volumetric heating is presented. A novel slice sweep technique provides volumetric anatomic and temperature information in near-real time. The combination with 2D motion compensation and adaptation of the ultrasound beam position allows to achieve volumetric heating according to a pre-defined target temperature or thermal dose value even in the presence of motion.

Key words: PRF thermometry, focused ultrasound, temperature control, PID

Contents

Part I

Introduction

Introduction

Cancer is one of the leading causes of death in Europe and accounted for 1.7 million deaths in 2008 [1]. Standard cancer therapies rely on a combination of surgery, radiotherapy and chemotherapy, but minimally or noninvasive therapies like radio-frequency [2], laser [3], or high-intensity focused ultrasound (HIFU) thermal ablation [4] have found increasing interest. All three treatment modalities are under investigation for the ablation of liver metastases [5–10] and for breast cancer therapy [11–17]. While radio-frequency-induced ablations are routinely employed for the treatment of cardiac arrhythmias [18], HIFU is being investigated for a variety of different applications. It has become a valuable tool in clinical routine for the non-invasive treatment of uterine leiomyomas [19, 20] and prostate cancer [21–23], and showed promising research results for the ablation of tumors in the kidney [24] and the brain [25, 26], for the treatment of thyroid nodules [27] as well as for cardiac ablation [28, 29] and the palliative treatment of bone metastases [30, 31]. Furthermore, there is interest in the use of HIFU for mild hyperthermia applications like local drug delivery [32–34] and the control of gene therapy using heat-sensitive promoters [35, 36].
For thermal ablations, the efficient and complete destruction of the targeted area with minimal damage to healthy tissue is the main objective, while for mild hyperthermia precise temperature control is mandatory for the success of the treatment. MRI can provide excellent soft-tissue contrast anatomical images, as well as real-time catheter visualization [37]. Moreover, the combination with proton resonance frequency shift (PRFS) based MR thermometry [38, 39] provides continuous temperature monitoring in conjunction with the possibility to estimate the resulting lesion sizes and thus an adequate therapy end point [40, 41]. However, precise temperature measurements using PRF require elaborate correction techniques, if motion and magnetic field variations are present during the treatment [42]. Depending on the target location, tailored approaches adapted to the specific motion pattern and the nature of the magnetic field variations have to be found. Furthermore, the tissue composition, e.g. the presence of fat and blood flow effects have to be taken into account. The objective of this work is to develop and evaluate adapted correction strategies for MR thermometry in the presence of motion and magnetic field variations with emphasis on the breast and the heart. For the specific case of the human breast, alternative techniques for MR thermometry will be explored. In order to address a second important aspect for thermal therapies, refined temperature control strategies, both for high-precision applications as well as for volumetric heating in the presence of motion will be presented.

1 Principles of MR thermometry

1.1 MR thermometry methods

A number of MR parameters have been found to be temperature dependent. The following review will give an overview of the principal methods used for MR thermometry and their physical background.

1.1.1 Temperature dependence of T_1

The dependence of the spin-lattice relaxation time T_1 with temperature is attributed to the dipolar coupling of the rotational and translational motions of free water molecules. In a simple model, this process follows the Boltzmann statistics, where an interaction of the excited spins and the lattice molecules becomes more likely with increasing temperature. Hence, spin-lattice relaxation can be described by [43]

$$T_1(T) \propto \mathrm{e}^{-E_a/kT} \quad , \tag{1.1}$$

where E_a denotes the activation energy of the relaxation process and kT the energy of the lattice at temperature T with the Boltzmann constant k. A more detailed overview of the temperature dependence of T_1 can be found in [44, 45]. Following this derivation, for small temperature changes and a small range of temperatures, the temperature dependence of T_1 can be approximated by [41]

$$T_1(T) = T_1(T_{\mathrm{ref}}) + \beta\,(T - T_{\mathrm{ref}}) \tag{1.2}$$

where $\beta = \mathrm{d}T_1/\mathrm{d}T$ is tissue dependent. Furthermore, for non-fatty tissue the temperature effect on T_1 is not reversible, once the temperature threshold for protein coagulation is exceeded. For the temperature dependence of T_1 in fatty tissues, however, this is not the case, which can be attributed to the stability of its chemical structure even for comparably high temperatures. This will be discussed in more detail in sect. 3.4. T_1-based thermometry has been studied extensively in the past [46, 47] and was successfully applied to monitor thermal thermal therapies [48].

1.1.2 Temperature dependence of T_2/T_2^*

The temperature dependence of the spin-spin relaxation time T_2 is expected to follow an expression similar to eq. (1.1) [44]. In practice, T_2 was observed to increase with temperature, but the T_2 change was found irreversible above a certain temperature threshold potentially due to tissue damage [49]. A linear increase of T_2 with temperature was also found in adipose tissue [50]. In the presence of magnetic field inhomogeneities,

the more complex spin-spin relaxation is described by the time constant T_2^* [51]. For its temperature dependence no consistent results are available, but a behavior similar to T_2 can be expected. However, the contribution of temperature dependent magnetic field changes (sect. 1.2.1) may lead to a more complex behavior.

1.1.3 Temperature dependence of the proton resonance frequency (PRF)

The temperature dependence of the resonance frequency of water was first studied extensively by Hindman [38].
The resonance frequency ω of a nucleus in a molecule depends on the local magnetic field B_{nuc} it experiences

$$\omega = \gamma B_{\mathrm{nuc}} \quad , \tag{1.3}$$

where γ specifies the gyromagnetic ratio of the nucleus (proton: $\gamma = 2\pi\, 42.58\,\mathrm{MHz\,T^{-1}}$). For the following descriptions of the characteristics of the proton resonance frequency, B_{nuc} has to be examined more closely.

Magnetic field at the position of the nucleus The magnetic field at the location of the nucleus is determined by three components [52–54]

$$\vec{B}_{\mathrm{nuc}}(\vec{r}) = \vec{B}_{\mathrm{mac}}(\vec{r}) + \vec{B}_{\mathrm{scr}}(\vec{r}) + \vec{B}_{\mathrm{lor}}(\vec{r}) \quad . \tag{1.4}$$

- $\vec{B}_{\mathrm{mac}}(\vec{r})$: observable external magnetic field in medium of susceptibility $\chi(\vec{r})$

  $$\vec{B}_{\mathrm{mac}}(\vec{r}) = \vec{B}_0(\vec{r}) + \vec{B}_{\mathrm{in}}(\vec{r}) + \vec{B}_{\mathrm{obj}}(\vec{r}) \tag{1.5}$$

  $\vec{B}_0(\vec{r})$: homogeneous main magnetic field, $\vec{B}_0(\vec{r}) = (0, 0, B_0)$
  $\vec{B}_{\mathrm{in}}(\vec{r})$ magnetic field inhomogeneities
  $\vec{B}_{\mathrm{obj}}(\vec{r})$ demagnetizing field of the object

- $\vec{B}_{\mathrm{scr}}(\vec{r})$: screening by the orbital electrons

  $$\vec{B}_{\mathrm{scr}}(\vec{r}) = -s\vec{B}_{\mathrm{mac}}(\vec{r}) \tag{1.6}$$

  with the electron screening coefficient s.

- $\vec{B}_{\mathrm{lor}}(\vec{r})$: effect of the sphere of Lorentz [55–57]. This term accounts for the fact that it is not possible to assume a continuous medium, as done in Maxwell's equations, while thinking microscopically. Rather, the existence of discrete atoms and molecules has to be considered. For this purpose the nucleus is placed inside an imaginary sphere where coincidental magnetic fluctuations lead to an effective zero susceptibility. The resulting magnetic field shift is given by

  $$\vec{B}_{\mathrm{lor}}(\vec{r}) = -\frac{2}{3}\chi(\vec{r})\vec{B}_{\mathrm{mac}}(\vec{r}) \quad . \tag{1.7}$$

Combining the given quantities, the resulting magnetic field at the location of the nucleus is given by

$$\vec{B}_{\mathrm{nuc}}(\vec{r}) = \left(1 - s - \frac{2}{3}\chi(\vec{r})\right) \vec{B}_{\mathrm{mac}}(\vec{r}) \quad . \tag{1.8}$$

As $\chi(\vec{r})$ is a small quantity and $B_{\mathrm{in}}(\vec{r}), B_{\mathrm{obj}}(\vec{r}) \ll B_0(\vec{r})$, higher order terms can be neglected. The same argument holds for the transverse components of the magnetic field. Hence, we can assume $B_{\mathrm{nuc}} \approx B_{\mathrm{nuc,z}}$.

$$B_{\mathrm{nuc}} \approx B_{\mathrm{nuc,z}} \approx B_0 \left(1 - s - \frac{2}{3}\chi(\vec{r})\right) + B_{\mathrm{in,z}} + B_{\mathrm{obj,z}} \quad . \tag{1.9}$$

$\vec{B}_{\mathrm{scr}}(\vec{r})$ and the temperature dependence of the PRF A proton in a free H_2O molecule is shielded by the electron cloud of the molecule, resulting in $\vec{B}_{\mathrm{scr}}(\vec{r})$. If this molecule is connected to another H_2O by a hydrogen bond, the shielding becomes less effective leading to an increased local magnetic field experienced by the nucleus As the temperature increases, the H_2O molecules will spend in average less time in a hydrogen bonded state resulting in an increased apparent screening constant and hence a reduced resonance frequency. Considering only the effect of the electronic screening on B_{nuc}, it follows

$$B_{\mathrm{nuc}} = (1 - s(T))\, B_0 \quad , \tag{1.10}$$

where $s(T)$ denotes the temperature dependent electron screening constant. For protons in pure water, Hindman described a linear relationship over a wide range of temperatures ($-15\,^{\circ}\mathrm{C}$ to $100\,^{\circ}\mathrm{C}$) with

$$s(T) = s_0 + \delta T \tag{1.11}$$

and $\delta = (1.03 \pm 0.02) \times 10^{-8}/^{\circ}\mathrm{C}$. s_0 represents the temperature independent part of the electron screening constant. Lutz et al. found a similar value ($\delta = 1.07 \times 10^{-8}/^{\circ}\mathrm{C}$ [58]). The temperature dependence of the resonance frequency of protons in watery tissue is comparable to that of free water protons and has been studied extensively over the last years yielding values ranging from $0.7 \times 10^{-8}/^{\circ}\mathrm{C}$ to $1.0 \times 10^{-8}/^{\circ}\mathrm{C}$ [59, 60]. Protons in fatty tissue however, have been shown to possess a negligible temperature dependence of the proton resonance frequency ($\delta_{\mathrm{fat}} = (0.019 \pm 0.035) \times 10^{-8}/^{\circ}\mathrm{C}$ [60]).

Thermometry using the temperature dependence of the PRF In order to use the PRF shift for absolute thermometry, $s(T)$ has to be determined for every temperature. Alternatively, the resonance frequency shift can be measured spectroscopically from the chemical shift with respect to an internal reference with known or negligible temperature dependence of the proton resonance frequency with temperature [61]. As these measurements are very time-consuming, in most applications the PRF is directly extracted from the image phase. The image phase is directly proportional to the proton resonance frequency via the echo time of the acquisition T_E

$$\phi = \omega T_E = \gamma B_{\mathrm{nuc}} T_E \quad . \tag{1.12}$$

Thus, using eq. (1.9) neglecting susceptibility effects ($B_{\mathrm{obj,z}} = 0$, $2/3\chi(\vec{r})B_0 = 0$), the measured phase can be expressed as follows

$$\phi = \gamma B_0 T_E \left(1 - s(T)\right) + \gamma B_{\mathrm{in,z}} T_E \quad . \tag{1.13}$$

As a result of the temperature dependence of the electron screening constant (1.11), the measured phase can be separated into a constant part ϕ_0 and a temperature dependent part $\phi_T(T)$

$$\begin{aligned} \phi &= \gamma T_E \left(B_0 \left(1 - s_0\right) + B_{\mathrm{in,z}}\right) - \gamma \delta T B_0 T_E \\ &= \phi_0 + \phi_T(T) \quad . \end{aligned} \tag{1.14}$$

In addition to the temperature independent part of the electron screening constant, the phase offset ϕ_0 depends mainly on the magnetic field inhomogeneities described by $B_{\mathrm{in,z}}$. As magnetic field inhomogeneities vary for every measurement (e.g. main magnetic field shim), this offset has to be eliminated. This is generally accomplished by using the phase difference $\Delta\phi = \phi(T) - \phi_{\mathrm{ref}}$ between the current phase and a reference phase, $\phi_{\mathrm{ref}} = \phi(T_{\mathrm{ref}})$ to extract the temperature change $\Delta T = T - T_{\mathrm{ref}}$ with respect to a reference temperature T_{ref} assuming that $B_{\mathrm{in,z}}(T_{\mathrm{ref}}) = B_{\mathrm{in,z}}(T)$

$$\Delta T_{\mathrm{PRF}} = -\frac{\Delta\phi}{\gamma B_0 T_E \delta} \quad . \tag{1.15}$$

The PRF method is independent of the tissue type (except fat) and yields the highest temperature precision of the known MR temperature measurement methods [62]. Moreover, the linear relationship with temperature and its reversibility within the temperature range used for thermal interventions makes it the method of choice for such applications. For all experiments in this thesis, $\delta = 0.94 \times 10^{-8}/^{\circ}\mathrm{C}$ was used [63, 64].

1.1.4 Alternative MR thermometry methods

The self diffusion coefficient D of water shows a linear temperature dependence with a temperature sensitivity of approximately 2 % per °C [65, 66]. This method has been used successfully to measure temperature in vivo [67].
Alternatively, the proton density can be exploited for MR thermometry via the equilibrium magnetization which is inversely proportional to the temperature [68]. However, the resulting temperature sensitivity of 0.3 % per °C [69, 70] is relatively low. It was furthermore proposed to use the temperature dependent magnetization transfer between water protons and protons of macromolecules for MR thermometry [47, 71].

1.2 Implementation of PRF-based thermometry

1.2.1 Susceptibility effects

In a medium of susceptibility χ, the Lorentz correction B_{lor} and the demagnetizing field of the object B_{obj} introduced in eq. (1.4, 1.7), have to be taken into account. As a

result, changes in the PRF reflect not only temperature variations in the object via a modified screening constant in B_{scr}, but also changes in B_{nuc} resulting from changes of the susceptibility distribution due to motion or respiration via B_{mac} and a heterogeneous temperature dependence of the susceptibility via B_{lor}. Consequently, eq. (1.15) modifies to

$$\Delta T_{\mathrm{meas}} = \Delta T_{\mathrm{PRF}} - \frac{1}{\delta}\left(\frac{\Delta B_{\mathrm{mac},z}}{B_0} - \Delta B_{\mathrm{lor},z}\right) \tag{1.16}$$

with

$$\begin{aligned}\Delta B_{\mathrm{mac},z} &= \Delta B_{\mathrm{in},z} + \Delta B_{\mathrm{obj},z} \\ &= B_{\mathrm{in}}\left(\chi(T)\right) - B_{\mathrm{in}}\left(\chi\left(T_{\mathrm{ref}}\right)\right) + B_{\mathrm{obj}}\left(\chi(T)\right) - B_{\mathrm{obj}}\left(\chi\left(T_{\mathrm{ref}}\right)\right)\end{aligned}$$

and

$$\Delta B_{\mathrm{lor},z} = -\frac{2}{3}\Delta\chi \qquad \text{with} \qquad \Delta\chi = \chi(T) - \chi\left(T_{\mathrm{ref}}\right) \quad .$$

The first correction term $\Delta B_{\mathrm{mac},z}/B_0$, poses severe problems for in vivo PRF thermometry and will be discussed in sect. 1.2.3. For the second correction term, the temperature dependence of the susceptibility of water, muscle and brain tissue have been studied and found to be much smaller than the temperature dependence of the proton resonance frequency shift ($(\mathrm{d}\chi/\mathrm{d}T)_{\mathrm{H_2O}} = 0.20 \times 10^{-8}/^{\circ}\mathrm{C} - 0.26 \times 10^{-8}/^{\circ}\mathrm{C}$, $(\mathrm{d}\chi/\mathrm{d}T)_{\mathrm{brain}} = (0.191 \pm 0.169) \times 10^{-8}/^{\circ}\mathrm{C}$, $(\mathrm{d}\chi/\mathrm{d}T)_{\mathrm{muscle}} = 0.16 \times 10^{-8}/^{\circ}\mathrm{C}$ [52, 60]). For fatty tissue, however, the temperature dependence of the susceptibility is comparable to the temperature dependence of the proton resonance frequency shift of water ($(\mathrm{d}\chi/\mathrm{d}T)_{\mathrm{fat}} = (0.804 \pm 0.145) \times 10^{-8}/^{\circ}\mathrm{C}$ [52, 60]) and thus not negligible. Several studies show that the resulting error in the temperature measurements depends on the susceptibility distribution and has a global effect on the magnetic field even in voxels which do not contain fat and even if fat suppression is applied in the MR sequence [72, 73].

1.2.2 Effects of inter-scan motion

As PRF temperature mapping relies on temperature calculations based on the pixel-wise phase difference with respect to a reference temperature, motion occurring during the intervention causes severe temperature artifacts. For this reason, it has to be ensured that for every dynamic image, the same pixel is chosen for the temperature calculation. This is even more important if the temperature measurements are to be used for thermal dose estimates (sect. 1.3). Details of the applied motion estimation algorithm can be found in sect. 4.5. In this work, every dynamic image is registered to a common reference position.

A second effect of the displacement of objects in an external magnetic field is the modification of the demagnetizing field of the object B_{obj} due to changes in the susceptibility distribution. As described above, these magnetic field variations have a global effect on the measured image phase and thus the temperature and cannot be corrected by motion compensation techniques acting on the images. Suitable correction strategies for these phase deviations will be discussed below.

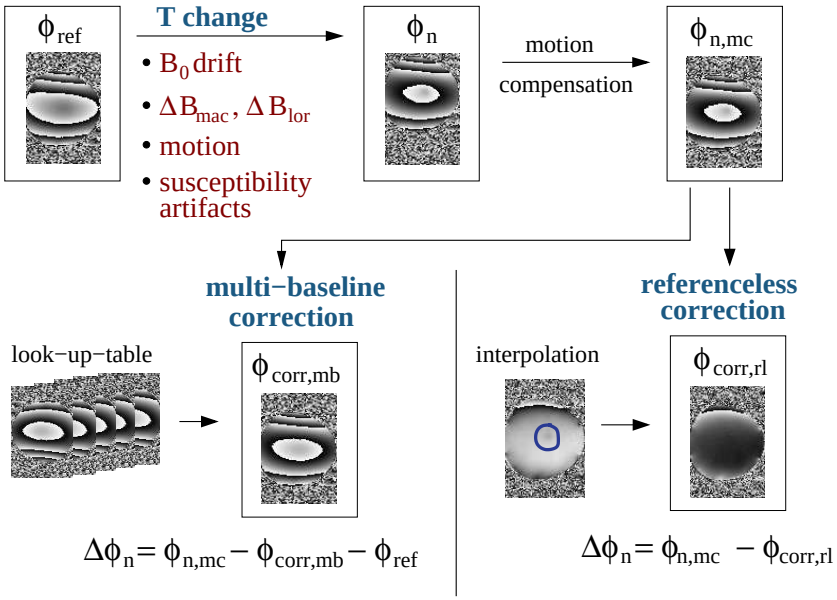

Figure 1.1: Principle of PRF thermometry using multi-baseline (mb) and referenceless (rl) phase correction. Before heating, a reference phase image ϕ_{ref} is acquired. During the treatment, the phase at instant n, ϕ_n is altered by different effects: temperature changes, motion and associated magnetic field variations ΔB_{mac}, variations of the susceptibility via ΔB_{lor}, drift of B_0 which contributes to ΔB_{mac} and possibly susceptibility artifacts induced by ferromagnetic materials. For both correction schemes, the acquired phase images have to be registered to a common reference position first ($\phi_{n,\mathrm{mc}}$). The multi-baseline phase correction algorithm has acquired a collection of phase images during a pre-treatment step without heating. This collection is now used to find the corresponding phase image containing the same motion-related susceptibility variations $\phi_{\mathrm{corr,mb}}$. The phase difference with respect to the reference phase can now be calculated. For the referenceless correction, the background phase $\phi_{\mathrm{corr,rl}}$ in the heated area is extrapolated from an annular ROI surrounding the target area.

1.2.3 Determination of the reference phase

It became obvious that the accurate determination of the reference phase ϕ_{ref} is an important issue for PRF thermometry. If no magnetic field variations or motion are present, the first phase image of the time series can be chosen as reference. However, this method is based on the assumption that phase changes are only caused by temperature changes whereas the magnetic field remains constant. According to equation (1.16), additional magnetic field variations $\Delta B_{\mathrm{mac}}/B_0 + \Delta B_{\mathrm{lor}}$ lead to an apparent artefactual temperature change which is different from the real temperature change depending on the magnetic field deviations present during the acquisition of the current and the reference image. As magnetic field variations in the image can be caused by changes of the susceptibility distribution even outside the field of view (e.g. respiration), they need to be corrected. What is more, the main magnetic field B_0 is not completely stable over time and thus contributes to ΔB_{mac}. Fluctuations caused by heating of the shim

irons induced by eddy currents or mechanical vibrations have been reported to cause field drifts of 0.06 ppm/min up to 1.32 ppm/min for field strengths of 1.5 to 7 T [74]. Different techniques have been developed to correct for such magnetic field variations during PRF thermometry and will be discussed below (Fig. 1.1).

Referenceless approach [75] In referenceless phase correction, the background phase is estimated from the image itself. If only a small region is heated, the area around can be used to determine the background phase. In a first step, the phase in the chosen area has to be unwrapped spatially. In a second step, a polynomial of order m

$$\phi(x,y) \approx \sum_{0 \leq i+j \leq m} a_{ij} x^i y^j \tag{1.17}$$

is fitted to the measured phase where the order m is determined in an initialization step at the beginning of the treatment. Finally the background phase in the heated area ϕ_{extrapol} is determined by extrapolation from the phase fit. The temperature rise can then be calculated using equation (1.15) with $\phi_{\text{ref}} = \phi_{\text{extrapol}}$ for every time point. This method has been successfully applied to monitor thermal ablations in the prostate [76] and has recently been refined by using a re-weighted ℓ_1-regression to identify the background phase in the heated area [77].
Alternatively, the background phase can be estimated by exploiting the harmonic property of the 3D static magnetic field, that is $\Delta H_{nuc} = \Delta B_{nuc}/\mu_0(1+\chi) = 0$ with the magnetic permeability in vacuum μ_0. In the magnetostatic case in the absence of eddy currents, this is also true for the magnetostatic potential, $\Delta\varphi_{\text{magn}} = 0$ [78]. Hence, the background phase data can be derived from the phase values on a surrounding spherical shell using the mean value property of harmonic functions stating that the mean value over a normalized spherical shell S is equal to the value at the center of the shell $\phi_0 = \langle\phi\rangle_S = (S \oplus \phi)_0$ [79, 80]. $\oplus$ denotes the convolution operator. This property has been used for referenceless MR thermometry in phantoms and the kidney of healthy volunteers in 2D [81]. For this application, the harmonic properties of the unwrapped image phase have been used to interpolate the missing parts of the circular border which was then used to solve the inner 2D Dirichlet problem for the background phase. The restriction to 2D resulted in zero and first order error terms.
Referenceless correction is able to correct the majority of phase variations occurring during the intervention, including main magnetic field drift and magnetic field variations due to spontaneous motion. However, the suitable positioning of the ROI for the background phase estimation is crucial for the quality of the correction and requires already a certain knowledge about the position of the heated area. Furthermore, spatial phase unwrapping is time-consuming and complicated close to interfaces between tissues with different susceptibilities. A sufficiently large area around the focal point is necessary to place the ROI, which is not always given for every treatment point. Finally, susceptibility artifacts due to ferromagnetic objects lead to apparent modifications of the background phase and thus to temperature estimation errors [82].

Multi-baseline phase correction [42, 83] For the particular case of periodical magnetic field variations during the intervention, multi-baseline phase correction can be applied. In an initial learning step, phase and magnitude images are stored in a look-up table. During the intervention, the current phase image is matched to a phase image in the look-up table corresponding to the same magnetic field variations. Depending on the character of the magnetic field variations, different techniques can be used to identify the correction phase in the look-up-table. For the general case with complex motion patterns, e.g. in the abdomen, this matching can be achieved by computing and comparing the inter-correlation coefficients between the magnitude images (sect. 4.5). Alternatively, the phase image itself can be used for this comparison [84]. If the source of the magnetic field variations is directly related to a parameter which can be easily detected, like the displacement of the diaphragm with the respiration, a third option can be used. In this case, the phase images are stored together with an external sensor output using a respiratory pressure sensor, a pencil-beam navigator (sect. 3.3), or a cardiac ECG which can be used to identify the current state of motion. A general limitation of this phase correction strategy is that only magnetic field variations, which have been recorded during the learning phase can eventually be corrected. What is more, the sampling density of the look-up table is limited and depends on the temporal resolution of the applied sequence and the period of the magnetic field variations. One solution for this problem is to use the phase images stored during the learning phase to create synthetic phase images based on a model function describing the relationship between phase and magnetic field variations (sect. 4, sect. 3.3). Once the corrected reference phase ϕ_{corr} has been identified, the temperature change with respect to the reference temperature

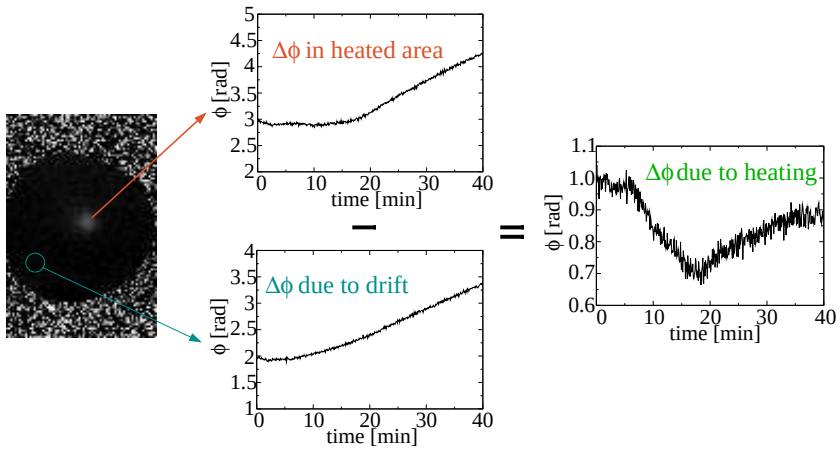

Figure 1.2: Drift correction using a ROI (blue circle) in a non-heated area assuming spatially homogeneous magnetic field drift. The HIFU-induced hot spot and the corresponding phase evolution are connected by the red arrow. The temporal phase changes extracted from this ROI are subtracted from the measured image phase on a pixel-by-pixel basis yielding the temperature-induced phase change in the heated area.

T_{ref} could be calculated using eq. (1.15). Due to the 2π periodicity of the image phase, a slightly modified approach is used which estimates the real temperature change at time index n, ΔT_n^{wrap}, with respect to the previous image [85]

$$\Delta T_n^{\text{wrap}} = \frac{(\phi_n - \phi_{\text{corr}})}{B_0 \gamma \delta T_E} - \Delta T_{n-1} \quad . \tag{1.18}$$

Here, ΔT_{n-1} denotes the previously calculated temperature map. The subscript "wrap" accounts for the fact that this temperature map still has to be temporally unwrapped in case a phase jump occurred in between. Note also, that the look-up table provides a correction map, whereas the reference image remains unchanged. In the implementation presented here, this was always the first acquired phase image in the look-up table.
The multi-baseline approach is suitable to correct periodic magnetic field variations and produces reliable temperature maps even in the presence of susceptibility artifacts caused by ferromagnetic materials, e.g. catheters. However, phase variations as a result of ΔB_{lor} and main magnetic field drift cannot be corrected with this method. This is also the case for phase variations, which have not been recorded during the learning phase, e.g. as a result of spontaneous motion [82].
Drift correction is generally accomplished by evaluating the phase variation in a ROI outside the heated area and subtracting the average phase in the ROI from the phase difference images (Fig. 1.2).

Hybrid approach Recently, the multi-baseline and referenceless approaches have been combined in two different ways. One computes the temperature map at each time step with a direct combination of both methods [86], while the second uses a temporal switch [82]. Initially the multi-baseline method is employed, but as soon as spontaneous motion occurs, for which the look-up-table does not contain a correction phase, the referenceless approach is used.

1.2.4 Temperature precision and sensitivity

The phase precision is inversely proportional to the signal-to-noise-ratio (SNR) of the image [87]. Consequently, the achievable minimal temperature standard deviation σ_T for the multi-baseline approach is always restricted by

$$\sigma_T = \frac{\sqrt{2}}{\text{SNR}_{\text{gauss}} B_0 \gamma \delta T_E} \quad , \tag{1.19}$$

where $\text{SNR}_{\text{gauss}}$ denotes the SNR corrected for the effects of Rician noise [88] in the phase images. The factor $\sqrt{2}$ results from the subtraction of the reference phase from the current phase. A model-based correction method could theoretically improve the temperature precision by a factor $\sqrt{2}$ as it uses synthetic, and hence noise-free reference phase images.
While the phase accumulation increases with the echo time, the signal decreases due to spin-spin relaxation with time constant T_2^*

$$\text{SNR}_{\text{gauss}} \propto M_0 \, \mathrm{e}^{-T_E/T_2^*} \quad , \tag{1.20}$$

assuming a fixed T_R with $T_R \ll T_1$ and a constant equilibrium magnetization M_0. As a result, the maximal temperature precision for a given sequence and magnetic field strength can be achieved if $T_E = T_2^*$ is chosen.
The effect of an increased main magnetic field strength is threefold. First, as indicated by equation (1.13), for the same echo time and temperature change, the phase accumulation is increased proportional to B_0 leading to an increased temperature sensitivity. At the same time in vivo where tissue thermal noise dominates, $M_0 \propto B_0$. As a result, the SNR should increase linearly according to equation (1.20), leading to a theoretically increased temperature precision at higher field strengths. However, this effect is in part compensated by the reduced T_2^* at higher field strengths in addition to complicating factors like the increased main magnetic field drift.

1.3 Thermal dose

An important issue for MR thermometry during hyperthermia treatments is to estimate the degree of tissue destruction. For thermal ablations, the aim of the treatment is to achieve a necrosis in the entire target area without heating adjacent healthy tissue extensively. Other applications like mild hyperthermia, local drug delivery or gene expression, operating in a temperature range up to 46 °C, rely on the non-destructive effect of temperature as an activator.
Lesion estimates can be retrieved from contrast enhanced T_1-weighted MR images post-treatment or alternatively from proton density or T_2-weighted MR images as these parameters are known to be sensitive to changes in the tissue microstructure due to coagulation and oedema [43, 44, 89–91]. However, MR thermometry can provide those estimates already during the treatment enabling adaptations of the treatment protocol and the determination of a suitable therapy endpoint [40, 41]. The thermal dose concept, in analogy to the radiation dose for ionizing radiation, provides a means to estimate cell death from exposure times and tissue temperatures. Very early, the observation of heating-induced effects in tissue showed an exponential relationship between the temperature T and exposure time t for both in vitro and in vivo tissue [92–94]

$$t_{\mathrm{end}} = t_{\mathrm{start}} \mathrm{R}^{(T_{\mathrm{end}} - T_{\mathrm{start}})} \quad , \tag{1.21}$$

with the start and end time t_{start}, t_{end} and corresponding temperatures T_{start}, T_{end}.
In this derivation, R at temperature T is defined following the Arrhenius formalism [95]

$$\mathrm{R} = \mathrm{e}^{AE_a / R_g T(T+1)} \quad , \tag{1.22}$$

where E_a is the activation energy for thermal effects in the tissue, R_g is the universal gas constant which was approximated as $R_g \approx 2$ and the constant $A = 1\,^{\circ}\mathrm{C}$ has been introduced to ensure correct units of the exponent. Sapareto et al. [96] found that the assumption of a constant R results in a negligible error of 2 %. As a result, R was defined as a step function with threshold temperature T_L for the onset of tissue destruction and

the final definition of the thermal dose TD as equivalent minutes reads

$$\mathrm{TD} = \int_0^t \mathrm{R}^{T_L - T(\tau)} \mathrm{d}\tau \quad , \quad \mathrm{R} = \begin{cases} 0.25 & T(t) < T_L \\ 0.5 & T(t) > T_L \end{cases} \quad . \tag{1.23}$$

In general, an equivalent time of 240 min (unity EM=equivalent minutes)) at $T_L = 43\,^\circ\mathrm{C}$ is used as a threshold for tissue necrosis [97]. Several experimental studies found a good correlation between the lesion size and the areas having received a thermal dose $\mathrm{TD} > 240\,\mathrm{EM}$ [98, 99].

2 Principles of Temperature control using HIFU

2.1 Focused ultrasound

2.1.1 Ultrasound properties

Ultrasound is an acoustic wave with a frequency higher than 18 kHz. It is propagated as a mechanical wave by causing oscillations of the atoms in a medium around their rest positions. In tissue, these oscillations occur mainly along the propagation direction corresponding to longitudinal propagation. Transverse shear waves can propagate in solids such as bone, but are quickly attenuated in soft tissues. The velocity of ultrasound in a medium c depends on its density ρ and acoustic impedance Z

$$c = \frac{Z}{\rho} \quad , \tag{2.1}$$

which is directly related to the frequency ν and wave length λ as $c = \lambda\nu$. In biological tissues, e.g. ultrasound propagates with a velocity $c = 1540\,\mathrm{m\,s^{-1}}$ corresponding to a wave length λ of $\sim 1\,\mathrm{mm}$ for a frequency of 1.5 MHz.

2.1.2 Focused ultrasound [100]

Ultrasound can be generated by applying voltage alternating with radio-frequency to a piezo-electric ceramic plate which has the characteristic to react to a electrical polarization with a mechanical contraction or expansion. The resonant frequency of the transducer is then defined by the thickness of the plate $\lambda/2$. Focalization of ultrasound waves can be accomplished by using either curved piezo-electric elements or suitable lenses in order to create constructive interference of the ultrasound waves at the focal point. The size and form of the focal point are then directly related to the shape of the emitting surface. For a spherical transducer, the diameter r and the length l of the resulting ellipsoidally shaped focal point are directly related to the focal length f and the diameter of the transducer d [101] (Fig. 2.1). Theoretically, this allows to adapt the design of the transducer to the required tissue depth [102].

2.1.3 Phased-array transducers [103]

Alternatively, focusing of the ultrasound waves can be achieved electronically by using one- or two-dimensional arrays of transducers which allow to adapt the phase and amplitude of each element independently to steer the position of the focal point [97, 104]. Figure 2.2a shows the numerical solution of the Rayleigh integral to determine the acoustic intensity distribution produced by the 256-element phased array-transducer operating

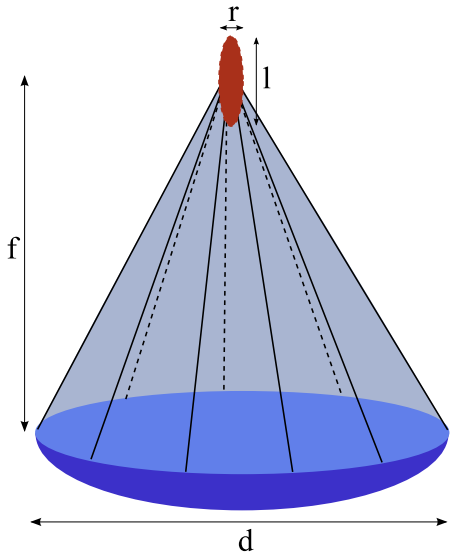

Figure 2.1: Spherical transducer with diameter d and focal length f which produces an ellipsoidal focal point of length l and width r.

at 1.2 MHz used in chapter 6. The effect of the electronic displacement of the focal point is visible in Fig. 2.2b for a 15 mm diameter circle. Displacing the focal point from its natural position leads to a modification of the focal point profile and as a result to a lower maximal acoustic intensity. Due to the production of undesired side lobes, the displacement of the focal point from its natural position is generally limited to a distance corresponding to a maximal acoustic intensity of approximately 50 % of the value achieved in the natural focal point position. This intensity difference can be compensated by increasing the applied acoustic intensity as shown in Fig. 2.2c. However, the additional energy will be distributed over the side lobes as well.

2.1.4 Ultrasound propagation and effects in biological tissue

The ultrasound velocity c in tissue is temperature dependent with a different behaviour for non-fatty and fatty tissues [105]. The attenuation of an ultrasound wave with acoustic intensity I in a medium at depth z follows an exponential relationship

$$I(z) = I_0 \mathrm{e}^{-2\mu z\nu} \tag{2.2}$$

where μ is the amplitude attenuation coefficient per unit path length ($\mu = 5\,\mathrm{Np\,m^{-1}MHz^{-1}}$ for soft tissue [106]) and ν is the ultrasound frequency (Fig. 2.3a). Like the dB, the unit Np (Neper) is used to express the ratio of two acoustic pressures ($p_{1/2}$) based on the natural logarithm (pressure level $L_{Np} = \ln p_1/p_2$, $1\,\mathrm{Np} \approx 8.686\,\mathrm{dB}$). In bone, μ is 10 to 20 times higher than in soft tissue leading to a very rapid absorption of the ultrasound energy and thus to a temperature hot spot on the bone surface [107]. In general, ultrasound attenuation in tissue is a combined effect of scattering and absorption α with

the latter being the dominating process which increases with the ultrasound frequency following the relation

$$\alpha = \alpha_0 \nu^m \quad , \tag{2.3}$$

with α_0 the absorption coefficient at $\nu = 1\,\mathrm{MHz}$ and $m \sim 1 - 1.2$ [108]. This relationship together with an example of the resulting axial heating pattern of a single element transducer operating at 1.5 MHz are shown in Fig. 2.3b,c.
However, scattering may account for the observed broadening of the focal spot in tissue as compared to theoretical predictions [109] (Fig. 2.3b). The absorption coefficients in soft tissues were found to be in the range of $3 - 8$ Np $\mathrm{m}^{-1}\mathrm{MHz}^{-1}$ [108].
As a result of the absorption of the ultrasound energy, the temperature within the tissue increases. This is the major effect, focused ultrasound induced hyperthermia relies on. The spatial and temporal temperature evolution in tissue with diffusion tensor D, absorption coefficient $\alpha(\vec{r})$ and perfusion coefficient ω including a power source $P_w(t)$ with the normalized acoustic intensity distribution $I(\vec{r})$ can be described by the heat transfer equation

$$\frac{\partial T(\vec{r},t)}{\partial t} = \vec{\nabla}\left(D(\vec{r})\vec{\nabla}T(\vec{r},t)\right) + \alpha(\vec{r})I(\vec{r})P_w(t) - \omega(\vec{r})T(\vec{r},t) \quad . \tag{2.4}$$

As a result, the observable temperature effect of focused ultrasound depends heavily on the thermal tissue coefficients. In highly perfused organs like liver and kidney, very high ultrasound intensities are needed to induce necrosis. At this point, cavitation effects might occur due to the formation of small gas bubbles within the tissue at high

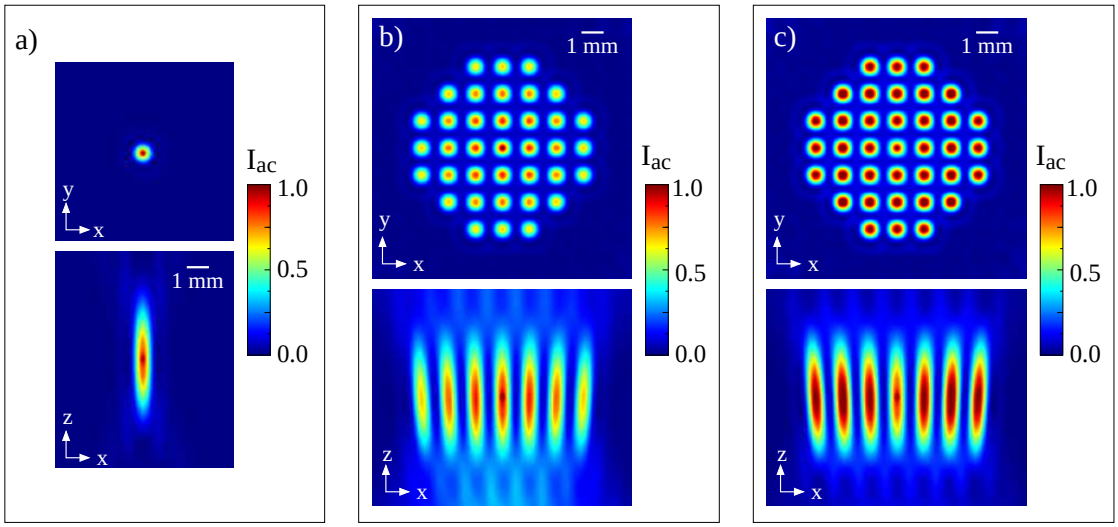

Figure 2.2: Simulation of the acoustic intensity field emitted by a phased-array transducer with $f = 120\,\mathrm{mm}$ and $d = 63.9\,\mathrm{mm}$ operating at 1.2 MHz. Shown are the profiles for $z = 0$ (upper image) and $y = 0$ (lower image). a) Single point at the natural focal point position. b) Sequential single point sonication of a 2D circular disc with diameter 15 mm using electronic displacement of the focal point without intensity compensation. c) with intensity compensation.

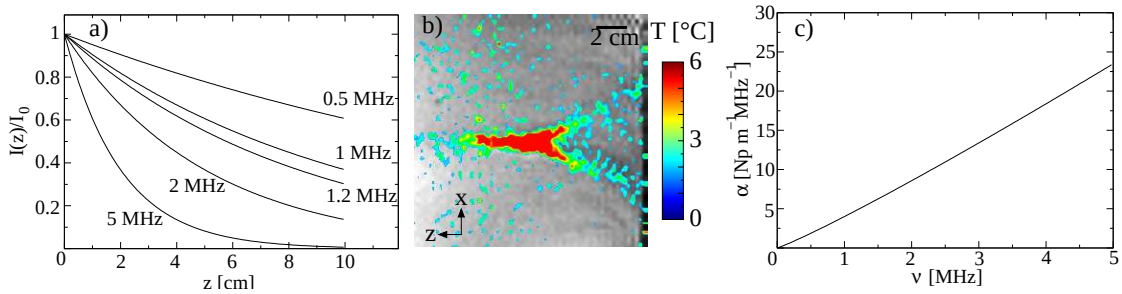

Figure 2.3: a) Attenuation as a function of the operating frequency of the ultrasound transducer for $\mu = 5\,\mathrm{Np\ m^{-1}MHz^{-1}}$. b) Heating pattern of a single element transducer operating at 1.5 MHz for an acoustic power of 80 W at $y = 0$. c) Absorption α as a function of the operating frequency of the ultrasound transducer ν for $\alpha_0 = 4\,\mathrm{Np\ m^{-1}MHz^{-1}}$.

ultrasound pressure levels. The resulting effects on biological tissues range from increased cell membrane permeability to tissue destruction and different values for the threshold pressure necessary for cavitation have been reported in literature [110–113].

2.2 Temperature control

In this context, temperature control is to mean the suitable adaptation of the ultrasound intensity and the location of the heated area to comply with a pre-defined protocol and to react to changes of tissue parameters during the treatment.

2.2.1 Proportional integral derivative (PID) control

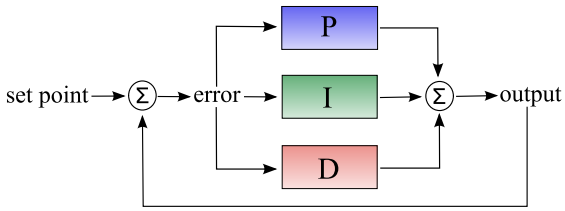

Figure 2.4: Diagram of the PID controller.

Basic principle The PID is the most common implementation of a feedback loop to control a system and is widely used in industry (Fig. 2.4). For every application, where a system variable is to be adjusted to comply with a given target value, a PID controller can be used. In order to understand the basic idea of a PID, a proportional-only controller (P) is a good start point. The entry value for the controller is given by the error, which is the difference between the target value and the current value of the system variable to be adjusted. The output of a P controller will be proportional to the present error and scaled by the proportional gain K_P. This simple implementation already allows

to control the system with a limited precision. However, in the presence of systematic errors, a residual error remains and can be corrected by introducing the integral part which takes into account the error history to compensate these effects. Finally, the derivative part provides a certain degree of anticipation, damping the controller output especially close to the set point.

Theory and implementation Given the desired and the measured temperatures $\theta(t)$ and $T(t)$ in the focal point ($\vec{r}_{\mathrm{fp}}$) the basic components for a classical proportional, integral, derivative controller are defined as follows

$$\begin{aligned} &\text{Proportional:} && \varepsilon(\vec{r}_{\mathrm{fp}}, t) \\ &\text{Integral:} && \int_0^t \varepsilon(\vec{r}_{\mathrm{fp}}, \tau)\mathrm{d}\tau \\ &\text{Derivative:} && \frac{\mathrm{d}\varepsilon(\vec{r}_{\mathrm{fp}}, t)}{\mathrm{d}t} \quad , \end{aligned} \tag{2.5}$$

where $\varepsilon(\vec{r}_{\mathrm{fp}}, t) = (\theta(\vec{r}_{\mathrm{fp}}, t) - T(\vec{r}_{\mathrm{fp}}, t))$ is the temperature error signal. In the ideal case, the following condition is fulfilled

$$K_P\ \varepsilon(\vec{r}_{\mathrm{fp}}, t) + K_I \int_0^t \varepsilon(\vec{r}_{\mathrm{fp}}, \tau)\mathrm{d}\tau + K_D \frac{\mathrm{d}\varepsilon(\vec{r}_{\mathrm{fp}}, t)}{\mathrm{d}t} = 0\,. \tag{2.6}$$

The coefficients K_P, K_I and K_D influence the system's response to changes in P, I or D and can be adapted accordingly.

Bibliography

[1] J. Ferlay, D.M. Parkin, and E. Steliarova-Foucher. Estimates of cancer incidence and mortality in europe in 2008. *Europ. J. Cancer*, 46:765–81, 2010.

[2] A.R. Gillams. The use of radiofrequency in cancer. *Brit. J. Cancer*, 92(10):1825–9, 2005.

[3] A.L. Gough-Palmer and W.M.W. Gedroyc. Laser ablation of hepatocellular carcinoma - A review. *World J. Gastroenterol.*, 14(47):7170–4, 2008.

[4] K. Hynynen. MRI-guided focused ultrasound treatments. *Ultrasonics*, 50(2):221–9, 2010.

[5] J.E. Kennedy, F. Wu, G. R. ter Haar, F.V. Gleeson, R.R. Phillips, M. R. Middleton, and D. Cranston. High-intensity focused ultrasound for the treatment of liver tumours. *Ultrasonics*, 42:931–5, 2004.

[6] B. Quesson, M. Merle, S. Roujol, B. Denis de Senneville, M.O. Köhler, C. Mougenot, and C.T.W. Moonen. A method for MRI guidance of intercostal high intensity focused ultrasound ablation in the liver. *Med. Phys.*, 37(6):2533–41, 2010.

[7] A.B. Holbrook, J.M. Santos, E. Kaye, V. Rieke, and K. Butts-Pauly. Real-time MR thermometry for monitoring HIFU ablations of the liver. *Magn. Res. Med.*, 63(2):365–73, 2010.

[8] S. Clasen and P.L. Pereira. Magnetic resonance guidance for radiofrequency ablation of liver tumors. *J. Magn. Res. Im.*, 27(2):421–33, 2008.

[9] M. Lepetit-Coiffé and H. Laumonier and O. Seror and B. Quesson and M.-B. Sesay and C.T.W. Moonen and N. Grenier and H. Trillaud. Real-time monitoring of radiofrequency ablation of liver tumors using thermal-dose calculation by MR temperature imaging: initial results in nine patients, including follow-up. *Eur. Radiol.*, 20(1):193–01, 2010.

[10] T.J. Vogl, R. Straub, K. Eichler, D. Woitaschek, and M.G. Mack. Malignant Liver Tumors Treated with MR Imaging - guided Laser-induced Thermotherapy: Experience with Complications in 899 Patients (2,520 lesions). *Radiology*, 225:367–77, 2002.

[11] K. Hynynen, O. Pomeroy, D.N. Smith, P.E. Huber, N.J. McDannold, J. Kettenbach, J. Baum, S. Singer, and F.A. Jolesz. MR imaging-guided focused ultrasound

surgery of fibroadenomas in the breast: A feasibility study. *Radiology*, 219:176–185, 2001.

[12] D.B. Zippel and M.Z. Papa. The use of MR imaging guided focused ultrasound in breast cancer patients: A preliminary phase one study and review. *Breast Cancer*, 12:21–38, 2005.

[13] H. Furusawa, K. Namba, S. Thomson, F. Akiyama, A. Bendet, C. Tanaka, Y. Yasuda, and H. Nakahara. Magnetic resonance-guided focused ultrasound surgery of breast cancer: Reliability and effectiveness. *J. Am. Coll. Surg.*, 203:54–63, 2006.

[14] W.E. Burak, D.M. Agnese, S.P. Povoski, T.L. Yanssens, K.J. Bloom, P.E. Wakely, and D.G. Spigos. Radiofrequency ablation of invasive breast carcinoma followed by delayed surgical excision. *Cancer*, 98(7):1369–76, 2003.

[15] F. Izzo, R. Thomas, P. Delrio, M. Rinaldo, P. Vallone, A. Dechiara, G. Botti, G. D'Aiuto, P. Cortino, and S.A. Curley. Radiofrequency ablation in patients with primary breast carcinoma : a pilot study in 26 patients. *Cancer*, 92(8):2036–44, 2001.

[16] H. Mumtaz, M.A. Hall-Craggs, A. Wotherspoon, M. Paley, G. Buonaccorsi, Z. Amin, I. Wilkinson, M.W. Kissin, T.I. Davidson, I. Taylor, and S.G. Bown. Laser therapy for breast cancer: MR imaging and histopathologic correlation. *Radiology*, 200:651–8, 1996.

[17] K. Dowlatshahi, D.S. Francescatti, and K.J. Bloom. Laser therapy for small breast cancers. *Am. J. Surgery*, 184(4):359–63, 2002.

[18] P. Jaïs, B. Cauchemez, L. Macle, E. Daoud, P. Khairy, R. Subbiah, M. Hocini, F. Extramiana, F. Sacher, P. Bordacher, G. Klein, R. Weerasooriya, J. Clémenty, and M. Haïssaguerre. Catheter ablation versus antiarrhythmic drugs for atrial fibrillation: The A4 study. *Circulation*, 118(24):2498–5, 2008.

[19] C.M. Tempany, E.A. Stewart, N.J. McDannold, B.J. Quade, F.A. Jolesz, and K. Hynynen. MR imaging-guided focused ultrasound surgery of uterine leiomyomas: A feasibility study. *Radiology*, 226:897–05, 2003.

[20] F.M. Fennessy, C.M. Tempany, N.J. McDannold, M.J. So, G. Hesley, B. Gostout, H.S. Kim, G.A. Holland, D.A. Sarti, K. Hynynen, F.A. Jolesz, and E.A. Stewart. Uterine leiomyomas: MR imaging-guided focused ultrasound surgery - results of different treatment protocols. *Radiology*, 243:885–893, 2007.

[21] K. Butts-Pauly, C.J. Diederich, V. Rieke, D. Bouley, J. Chen W. Nau, A.B. Ross, A. Kinsey, and G. Sommer. Magnetic Resonance-Guided High-Intensity Ultrasound Ablation of the Prostate. *Top. Magn. Res. Imag.*, 17(3):195–07, 2006.

[22] A. Blana, F.J. Murat, B. Walter, S. Thuroff, W.F. Wieland, C. Chaussy, and A. Gelet. First Analysis of the Long-Term Results with Transrectal HIFU in Patients with Localised Prostate Cancer. *Europ. Urology*, 53:1194–03, 2008.

[23] K. Siddiqui, R. Chopra, S. Vedula, L. Sugar, M. Haider, A. Boyes, M. Musquera, M. Bronskill, and L. Klotz. MRI-guided Transurethral Ultrasound Therapy of the Prostate Gland Using Real-time Thermal Mapping: Initial Studies. *Urology*, 2010. in press.

[24] R.O. Illing, J.E. Kennedy, F. Wu, G.R. ter Haar, A.S. Protheroe, P.J. Friend, F.V. Gleeson, D.W. Cranston, R.R. Phillips, and M.R. Middleton. The safety and feasibility of extracorporeal high-intensity focused ultrasound (HIFU) for the treatment of liver and kidney tumours in a Western population. *Brit. J. Cancer*, 93(8):890–5, 2005.

[25] K. Hynynen and G. Clement. Clinical applications of focused ultrasound - The brain. *Int. J. Hyp.*, 23(2):193–02, 2007.

[26] B. Larrat, M. Pernot, J.-F. Aubry, E. Dervishi, R. Sinkus, D. Seilhean, Y. Marie, A.-L. Boch, M. Fink, and M. Tanter. MR-guided transcranial brain HIFU in small animal models. *Phys. Med. Biol.*, 55(2):365–88, 2010.

[27] O. Esnault, B. Franc, J.-P. Monteil, and J.-Y. Chapelon. High-Intensity Focused Ultrasound for Localized Thyroid-Tissue Ablation: Preliminary Experimental Animal Study. *Thyroid*, 14(12):1072–6, 2005.

[28] N.T. Sanghvi, F.J. Fry, A. Zaitsev, and J. Olgin. Cardiac ablation using high intensity focused ultrasound: a feasibility study. In *Proc. IEEE Ultrasonics Symposium, Toronto, Canada*, 1997. p.1323 - 1326, vol.2.

[29] B. Schmidt, M. Antz, S. Ernst, F. Ouyang, P. Falk, J.K.R. Chun, and K.-H. Kuck. Pulmonary vein isolation by high-intensity focused ultrasound: First-in-man study with a steerable balloon catheter. *Heart Rhythm*, 4(5):575–84, 2007.

[30] R. Catane, A. Beck, Y. Inbar, T. Rabin, N. Shabshin, S. Hengst, R.M. Pfeffer, A. Hanannel, O. Dogadkin, B. Liberman, and D. Kopelman. MR-guided focused ultrasound surgery (MRgFUS) for the palliation of pain in patients with bone metastases - Preliminary clinical experience. *Ann. Oncol.*, 18(1):163–167, 2007.

[31] D. Gianfelice, C. Gupta, W. Kucharczyk, P. Bret, D. Havill, and M. Clemons. Palliative treatment of painful bone metastases with MR imaging - Guided focused ultrasound. *Radiology*, 249(1):355–363, 2008.

[32] J.A. Weinstein, R.L. Margin, M.B. Yatvin, and D.S. Zaharko. Liposomes and local hyperthermia: Selective delivery of methotrexate to heated tumors. *Science*, 204:188–91, 1979.

[33] D. Needham and M.W. Dewhirst. The development and testing of a new temperature-sensitive drug delivery system for the treatment of solid tumors. *Adv. Drug. Deliv. Rev.*, 53(3):285–05, 2001.

[34] R. Deckers, C. Rome, and C.T.W. Moonen. The role of ultrasound and magnetic resonance in local drug delivery. *J. Magn. Res. Im.*, 27(2):400–9, 2008.

[35] D.P. Madio, P. van Gelderen, D. DesPres, A.W. Olson, J.A. de Zwart, T.W. Fawcett, N.J. Holbrook, M. Mandel, and C.T.W. Moonen. On the feasibility of MRI-guided focused ultrasound for local induction of gene expression. *J. Magn. Res. Im.*, 8:101–104, 1998.

[36] R. Deckers, B. Quesson, J. Arsaut, S. Eimer, F. Couillaud, and C.T.W. Moonen. Image-guided, noninvasive, spatiotemporal control of gene expression. *Proc. Natl. Acad. Sci. USA*, 106(4):1175–1180, 2009.

[37] E.J. Schmidt, R. Yoneyama, C.L. Dumoulin, R.D. Darrow, E. Klein, A.J.M. Kiruluta, and M. Hayase. 3D coronary motion tracking in swine models with MR tracking catheters. *J. Magn. Res. Im.*, 29:86–98, 2009.

[38] J. Hindman. Proton resonance shift of water in the gas and liquid states. *J. Chem. Phys.*, 44:4582–4592, 1966.

[39] Y. Isihara, A. Calderon, H. Watanabe, K. Okamoto, Y. Suzuki, K. Kuroda, and Y. Suzuki. A precise and fast temperature mapping using water proton chemical shift. *Magn. Res. Med.*, 34(6):814–23, 1995.

[40] B. Quesson, J.A. de Zwart, and C.T.W. Moonen. Magnetic resonance temperature imaging for guidance of thermotherapy. *J. Magn. Res. Im.*, 12:525–33, 2000.

[41] V. Rieke and K. Butts-Pauly. MR thermometry. *J. Magn. Res. Im.*, 27:376–90, 2008.

[42] B. Denis de Senneville, C. Mougenot, and C.T.W. Moonen. Real time adaptive methods for treatment of mobile organs by MRI controlled high intensity focused ultrasound. *Magn. Res. Med.*, 57:319–330, 2007.

[43] D.L. Parker, V. Smith, P. Sheldon, L.E. Crooks, and L. Fussell. Temperature distribution measurements in two-dimensional NMR imaging. *Med. Phys.*, 10:321–25, 1983.

[44] P.A. Bottomley, T.H. Foster, R.E. Argersinger, and L.M. Pfeifer. A review of normal tissue hydrogen NMR relaxation times and relaxation mechanisms from 1-100 MHz: Dependence on tissue type, NMR frequency, temperature, species, excision, and age. *Med. Phys.*, 11(4):425–48, 1984.

[45] T.R. Nelson and S.M. Tung. Temperature dependence of proton relaxation times in vitro. *Magn. Res. Im.*, 5:189–99, 1987.

[46] M. Peller, H.M. Reinl, A. Weigel, M. Meininger, R.D. Issels, and M. Reiser. T1 relaxation time at 0.2 Tesla for monitoring regional hyperthermia: feasibility study in muscle and adipose tissue. *Magn. Res. Med.*, 47:1194–01, 2002.

[47] I.R. Young, J.W. Hand, A. Oatridge, and M.V. Prior. Modeling and observation of temperature changes in vivo using MRI. *Magn. Res. Med.*, 32:358–69, 1994.

[48] T.J. Vogl, R. Straub, S. Zangos, M.G. Mack, and K. Eichler. MR-guided laser-induced thermotherapy (LITT) of liver tumors: experimental and clinical data. *Int. J. Hyp.*, 20:713–24, 2004.

[49] S.J. Graham, M.J. Bronskill, and R.M. Henkelman. Time and temperature dependence of MR parameters during thermal coagulation of ex vivo rabbit muscle. *Magn. Res. Med.*, 39:198–3, 1998.

[50] S. Gandhi, K. Daniel, and K. Butts. Temperature dependence of relaxation times in bovine adipose tissue. In *Proc. 6th ISMRM meeting, Sydney*, 2001. p. 701.

[51] E.M. Haacke, Brown R.W., Thompson M.R., and Venkatesan R. *Magnetic Resonance Imaging: Physical principles and sequence design*. John Wiley & Sons, New York, 1999.

[52] J. de Poorter. Noninvasive MRI thermometry with the proton resonance frequency method: Study of susceptibility effects. *Magn. Res. Med.*, 34:359–67, 1995.

[53] L. Li. Magnetic susceptibility quantification for arbitrarily shaped objects in inhomogeneous fields. *Magn. Res. Med.*, 46:907–16, 2001.

[54] R. Salomir, B. Denis de Senneville, and C.T.W. Moonen. A fast calculation method for magnetic field inhomogeneity due to an arbitrary distribution of bulk susceptibility. *Conc. Magn. Res. B*, 19B(1):26–34, 2003.

[55] H.A. Lorentz. *The theory of Electrons and its application to the phenomena of light and heat*. New York:Dover, 1915.

[56] R.P. Feynman, R.P. Leighton, and M. Sands. *The Feynman Lectures on Physics Vol.2*. Addison Wesley, 1975.

[57] W.C. Dickenson. The time average magnetic field at the nucleaus in nuclear magnetic resonance experiments. *Phys. Rev.*, 81:717–731, 1950.

[58] K.W. Lutz, A.C. Kuesel, and W.E. Hull. A 1H-NMR method for determining temperature in cell culture perfusion systems. *Magn. Res. Med.*, 29:113–18, 1993.

[59] K. Kuroda, K. Abe, S. Tsutsumi, Y. Isihara, Y. Suzuki, and K. Sato. Water proton magnetic resonance spectroscopic imaging. *Biomed. Thermol.*, 13:43–62, 1993.

[60] R. Stollberger, P.W. Ascher, D. Huber, W. Renhart, H. Radner, and F. Ebner. Temperature monitoring of interstitial thermal tissue coagulation using MR phase images. *J. Magn. Res. Im.*, 8:188–96, 1997.

[61] K. Kuroda, Y. Suzuki, Y. Isihara, K. Okamoto, and Y. Suzuki. Temperature mapping using water proton chemical shift obtain with 3D-MRSI: Feasibility in vivo. *Magn. Res. Med.*, 35:20–29, 1996.

[62] W. Wlodarczyk, M. Hentschel, P. Wust, R. Noeske, N. Hosten, H. Rinneberg, and R. Felix. Comparison of four magnetic resonance methods for mapping small temperature changes. *Phys. Med. Biol.*, 44:607–24, 1999.

[63] J.A. de Zwart, P. van Gelderen, D.J. Kelly, and C.T.W. Moonen. Fast magnetic-resonance temperature imaging. *J. Magn. Res. B*, 112(1):86–90, 1996.

[64] J.A. de Zwart, F.C. Vimeux, C. Delalande, P. Canioni, and C.T.W. Moonen. Fast lipid suppressed MR temperature mapping with echo-shifted gradient echo imaging and spectral-spatial excitation. *Magn. Res. Med.*, 42:52–59, 1999.

[65] D. Le Bihan, J. Delannoy, and R.L. Levin. Temperature mapping with MR imaging of molecular diffusion: Application to hyperthermia. *Radiology*, 171:853–57, 1989.

[66] Y. Zhang, T.W. Samulski, W.T. Joines, J. Mattiello, R.L. Levin, and D. Le Bihan. On the accuracy of noninvasive thermometry using molecular diffusion magnetic resonance imaging. *Int. J. Hyp.*, 8:263–74, 1992.

[67] A.R. Bleier, F.A. Jolesz, and M.S. Cohen. Real-time magnetic resonance imaging of laser heat deposition in tissue. *Magn. Res. Med.*, 21:132–37, 1991.

[68] A. Abragam. *The principles of nuclear magnetism*. Clarendon Press, Oxford, 1983.

[69] F. Johnson, H. Eyring, and B. Stover. *Theory of rate processes in biology and medicine*. John Wiley & Sons, New York, 1974.

[70] J. Chen, B.L. Daniel, and K. Butts-Pauly. Investigation of proton density for measuring tissue temperature. *J. Magn. Res. Im.*, 23:430–34, 2006.

[71] S.J. Graham, G.J. Stanisz, A. Kecojevic, M.J. Bronskill, and R.M. Henkelman. Analysis of changes in MR properties of tissues after heat treatment. *Magn. Res. Med.*, 42:1061–71, 1999.

[72] R.D. Peters, R.S. Hinks, and R.M. Henkelman. Heat-source orientation and geometry dependence in proton resonance frequency shift magnetic resonance thermometry. *Magn. Res. Med.*, 41:909–18, 1999.

[73] S.M. Sprinkhuizen, M.K. Konings, M.J. van der Bom, M.A. Viergever, C.J.G. Bakker, and L.W. Bartels. Temperature-induced tissue susceptibility changes lead to significant temperature errors in PRFS-based MR thermometry during thermal interventions. *Magn. Res. Med.*, 2010. in press.

[74] T. Benner, A.J.W. van der Kouwe, J.E. Kirsch, and A.G. Sorensen. Real-time RF pulse adjustment for B0 drift correction. *Magn. Res. Med.*, 56:204–9, 2006.

[75] V. Rieke, K.K. Vigen, G. Sommer, B.L. Daniel, J.M. Pauly, and K. Butts. Referenceless PRF shift thermometry. *Magn. Res. Med.*, 51(6):1223–31, 2004.

[76] V. Rieke, A.M. Kinsey, A.B. Ross, W.H. Nau, C.J. Diederich, S. Sommer, and K. Butts-Pauly. Referenceless MR thermometry for monitoring thermal ablation in the prostate. *IEEE Trans. Med. Im.*, 26(6):813–21, 2007.

[77] W.A. Grissom, M. Lustig, A.B. Holbrook, V. Rieke, J.M. Pauly, and K. Butts-Pauly. Reweighted l1 referenceless PRF shift thermometry. *Magn. Res. Med.*, 2010. in press.

[78] L. Li and J.S. Leigh. High-precision mapping of the magnetic field utilizing the harmonic function mean value property. *J. Magn. Res.*, 148(2):442–48, 2001.

[79] S.J. Axler, P. Bourdon, and W. Ramey. *Harmonic Function Theory.* Springer Verlag, New York, 2001.

[80] F. Schweser, B.W. Lehr, A. Deistung, and J.R. Reichenbach. A Novel Approach for Separation of Background Phase in SWI Phase Data Utilizing the Harmonic Function Mean Value Property. In *Proc. 18th ISMRM meeting, Stockholm*, 2010. 142.

[81] R. Salomir, M. Viallon, J. Roland, S. Terraz, D. Morel, C. Becker, and P. Gross. Reference-less PRFS MR thermometry using a thin open border and the harmonic function theory: 2D experimental validation. In *Proc. 18th ISMRM meeting, Stockholm*, 2010. 247.

[82] B. Denis de Senneville, S. Roujol, C.T.W. Moonen, and M. Ries. Motion correction in MR thermometry of abdominal organs: A comparison of the referenceless vs. the multibaseline approach. *Magn. Res. Med.*, 2010. in press.

[83] K.K. Vigen, B.L. Daniel, and K. Butts. Triggered, navigated, multi-baseline method for proton resonance frequency temperature mapping with respiratory motion. *Magn. Res. Med.*, 50:1003–10, 2003.

[84] S.M. Sprinkhuizen, N.H.G.M. Peters, K.L. Vinken, C.J.G. Bakker, and L.W. Bartels. Quantification and correction of motion-induced field disturbances for accurate PFRS-based MR thermometry. In *Proc. 6th interv. MRI symp., Leipzig*, 2006. p.113-6.

[85] B. Denis De Senneville, B. Quesson, P. Desbarats, R. Salomir, J. Palussière, and C.T.W. Moonen. Atlas-based motion correction for on-line MR temperature mapping. *IEEE, ICIP*, Vol.III:2571–74, 2004.

[86] W.A. Grissom, A.B. Holbrook, V.A. Rieke, M. Lustig, J.A. Santos, A. Swaminathan, M.V. McConnell, and K. Butts-Pauly. Hybrid Multi-baseline and referenceless PRF-shift thermometry. In *Proc. 18th ISMRM, Stockholm, Sweden*, 2010.

[87] T.E. Conturo and G.D. Smith. Signal-to-noise in phase angle reconstruction: Dynamic range extension using phase reference offsets. *Magn. Res. Med.*, 15(3):420–37, 1990.

[88] H. Gudbjartsson and S. Patz. The Rician distribution of noisy MRI data. *Magn. Res. Med.*, 34(6):910–4, 1995.

[89] C.J. Lewa and Z. Majewska. Temperature relationships of proton spin-lattice relaxation tim T1 in biological tissues. *Bull. Cancer*, pages 525–30, 1980.

[90] K. Hynynen, C.A. Damianou, V. Colucci, E. Unger, H.H. Cline, and F.A. Jolesz. MR monitoring of focused ultrasonic surgery of renal cortex: Experimental and simulation studies. *J. Magn. Res. Im.*, 5:259–66, 1995.

[91] K. Hynynen, N.I. Vykhodtseva, A.H. Chung, V. Sorrentino, V. Colucci, and F.A. Jolesz. Thermal effects of focused ultrasound on the brain: Determination with MR imaging. *Radiology*, 204:247–53, 1997.

[92] W.C. Dewey, L.E. Hopwood, S.A. Sapareto, and L.E. Gerweck. Cellular responses to combinations of hyperthermia and radiation. *Radiology*, 123:463–79, 1976.

[93] K.J. Henle and D.B. Leeper. Interaction of hyperthermia and radiation in cho cells: recovery kinetics. *Radiat. Res.*, 66:505–18, 1976.

[94] J. Overgaard and H.D. Suit. Time-temperature relationship in hypetthermic treatment of malignant and normal tissue in vivo. *Cancer Res.*, 39:3248–53, 1979.

[95] K.J. Laidler. *Chemical Kinetics, Third Edition*. Benjamin-Cummings, 1997.

[96] S.A. Sapareto and W.C. Dewey. Thermal dose determination in cancer therapy. *Int. J. Radiat. Oncol. Biol. Phys.*, 10(6):787–800, 1984.

[97] D.R. Daum and K. Hynynen. Thermal dose optimization via temporal switching in ultrasound surgery. *IEEE Trans. Ultrason. Ferroelect. Frequ. Contr.*, 43:208–15, 1998.

[98] S.J. Graham, L. Chen, M. Leitch, R.D. Peters, M.J. Bronskill, F.S. Foster, R.M. Henkelman, and D.B. Plewes. Quantifying tissue damage due to focused ultrasound heating observed by MRI. *Magn. Res. Med.*, pages 321–28, 1999.

[99] M. Lepetit-Coiffé, H. Laumonier, O. Seror, B. Quesson, M.B. Sesay, C.T.W. Moonen, N. Grenier, and H. Trillaud. Real-time monitoring of radiofrequency ablation of liver tumors using thermal-dose calculation by MR temperature imaging: initial results in nine patients, including follow-up. *Eur. Radiol.*, 20(1):193–1, 1999.

[100] F.A. Jolesz and K. Hynynen. *MR-guided focused ultrasound surgery*. Informa Healthcare USE, Inc., 2008.

[101] H.T. O'Neil. Theory of focusing radiators. *J. Acoust. Soc. Am.*, 21(3):516–26, 1949.

[102] K. Hynynen, D.J. Watmough, and J.R. Mallard. Design of ultrasonic transducers for local hyperthermia. *Ultrasound Med. Biol.*, 7(4):397–2, 1981.

[103] C. Mougenot. *L'asservissement par IRM d'un réseau matriciel ultrasonore et ses applications thérapeutiques.* PhD thesis, L'Université Bordeaux 1, Bordeaux, France, 2005.

[104] D.R. Daum and K. Hynynen. A 256-element ultrasonic phased array system for the treatment of large volumes of deep seated tissue. *IEEE Trans. Ultrason. Ferroelect. Frequ. Contr.*, 46:1254–1268, 1999.

[105] J.C. Bamber and C.R. Hill. Ultrasonic attenuation and propagation speed in mammalian tissues as a function of temperature. *Ultrasound Med. Biol.*, 5:149–57, 1979.

[106] J.F. Debatin and G. Adam. *Interventional magnetic resonance imaging.* Springer-Verlag, Berlin Heidelberg, 1998.

[107] K. Hynynen and D. DeYoung. Temperature elevation at muscle-bone interface during scanned, focused ultrasound hyperthermia. *Int. J. Hyp.*, 4:267–79, 1988.

[108] S.A. Goss, L.A. Frizzell, and F. Dunn. Ultrasonic absorption and attenuation in mammalian tissues. *Ultrasound Med. Biol.*, 5:181–86, 1979.

[109] K. Mahoney, T. Fjield, N.J. McDannold, G. Clement, and K. Hynynen. Comparison of modelled and observed in vivo temperature elevations induced by focused ultrasound: Implications for treatment planning. *Phys. Med. Biol.*, 46(7):1785–98, 192001.

[110] P.P. Lele. Threshold and mechanisms of ultrasonic damage to organized animal tissue. In *Proc. Symp. on Biol. Effects and Charact. of Ultras. Sources, Rockeville, MA*, 1977.

[111] K. Hynynen. The threshold for thermally significant cavitation in dog's thigh muscle *in vivo*. *Ultrasound Med. Biol.*, 17(2):157–69, 1991.

[112] F. Prat, J.Y. Chapelon, A. Fadil, A. Sibille, Y. Theilliere, T. Ponchon, and D. Cathignol. Focused liver ablation by cavitation in the rabbit: A potential new method of extracorporeal treatment. *Gut*, 35:395–00, 1994.

[113] N.T. Sanghvi. Role of cavitation during high intensity focused ultrasound treatment of prostate tissue. In *Proc. Acoust. Soc. Am., Seattle*, 1998. pp 1067-1068.

Part II

MR thermometry in the presence of motion and magnetic field variations

Introduction

Commonly, PRF-based MR-thermometry relies on the voxelwise evaluation of phase differences between sequentially acquired gradient echo images. However, as pointed out in sect. 1.2, this technique is very sensitive to motion artifacts and magnetic field changes. In particular, respiratory induced tissue displacements and the related susceptibility effects can lead to magnetic field changes which may bias MR-thermometry. Respiratory-gating using navigators or pressure sensors [1], or imaging during breathhold offer possible solutions but lead to poor temporal resolution or limited acquisition times. However, due to the periodical character of the respiratory motion, the acquisition of a collection of images representing different respiratory states can be helpful for thermometry correction in the subsequent treatment.
In addition to the mentioned susceptibility variations, the target area itself can be subject to continuous displacements. If no gating or breathold imaging is performed, these motion effects have to be corrected in order to ensure accurate thermometry and thermal dose measurements [2]. However, the influence of motion and susceptibility variations may vary depending on the specific target area. This work will focus on two particular cases which will serve as examples in order to evaluate the performance of different look-up-table based phase correction methods. These examples will also serve to discuss two additional issues which may interfere with MR thermometry: the presence of fatty tissue and blood flow. The static case, where no additional motion compensation is required, will be discussed in sect. 3.3 using the example of MR thermometry in the human breast. This discussion will be followed in sect. 3.4 by the presentation of a novel method for simultaneous PRF thermometry and T_1 mapping using variable flip angles which can be used to perform T_1 thermometry in fatty tissue. As a second example, chapter 4 will deal with thermometry of the heart where, due to the complex motion pattern, robust motion compensation is crucial. Here, emphasis will be put on the choice of the imaging sequence and parameters, and the importance of blood suppression for accurate cardiac thermometry.

3 MR thermometry in the breast: A static target

3.1 Clinical context

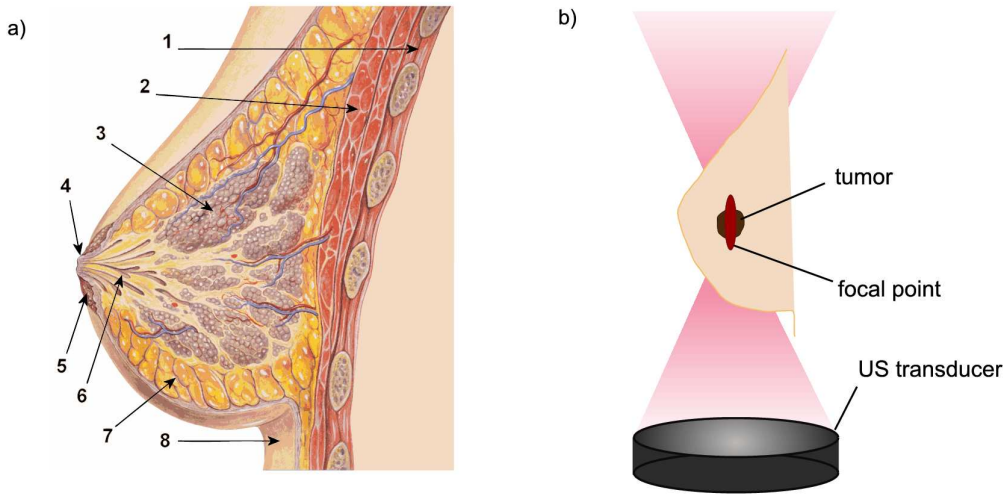

Figure 3.1: a) Breast anatomy: 1 chest wall, 2 pectoralis muscles, 3 lobules, 4 nipple surface, 5 areola, 6 lactiferous duct, 7 fatty tissue, 8 skin. b) Setup for focused ultrasound treatment of a breast tumor.

Breast cancer is the most common form of cancer in women in Europe. In 2008, it accounted for 28 % (421.000 cases) of newly discovered cancer and was with 17 % the leading cause of cancer-related mortality for women in Europe [3]. The standard treatment for breast cancer is surgery, ranging from local resection to total mastectomy, followed by radiation or chemotherapy. However, for early detected breast cancer, there is a trend to prefer breast conservation by choosing minimally invasive or non-invasive techniques such as high-intensity focused ultrasound (HIFU) ablation, cryotherapy, radio-frequency ablation, microwave ablation, or interstitial laser therapy in order to induce necrosis of the tumor tissue [4, 5]. Breast MR is highly sensitive for detecting the presence and

extent of most types of breast tumors with high sensitivities [6, 7]. It has furthermore been suggested that breast cancer treatment using thermal ablation could be improved if guided by an imaging modality providing reliable temperature information [8, 9].

3.2 Experimental considerations

In the particular case of PRF thermometry in the human breast, magnetic field variations induced by the changing lung volume during the respiratory cycle lead to phase fluctuations, which have to be corrected in order to prevent thermometry artifacts. In contrast to organs like kidney or liver, the breast remains stationary during the breathing cycle. As a result, no additional motion compensation in the target area is necessary. For this application, a look-up-table-based multi-baseline correction algorithm [10] can be used to correct for the periodic magnetic field changes.

The second part of this chapter will deal with another important issue for PRF thermometry. Apart from magnetic field variations and motion, the presence of fat in the imaging voxels may lead to incorrect PRF thermometry measurements. This is because the temperature dependence of the proton resonance shift frequency of fat is negligible in contrast to that of water [11, 12]. Consequently, in fat-containing organs like the liver, fat suppression is crucial in order to avoid erroneous temperature measurements due to partial volume signal from fat protons. Since a sufficient number of water protons is present in every voxel, a detectable phase change with temperature can be detected even if fat suppression is applied. On the contrary, in organs like the human breast or the prostate where fatty and non-fatty tissue are compartmentalized, partial volume effects occur only at the interfaces between the tissue types. The same is true if MR thermometry is to be used for temperature monitoring in breast tumors which are known to contain only very little or no fat [13]. In this case, temperature information would only be accessible within the tumor but not in the surrounding tissue.
In fatty tissue, T_1-based thermometry may be used to deliver temperature information as already shown by Hynynen et al. [14]. As T_1 mapping is based on the analysis of the signal amplitude while PRF is assessed from the image phase, dynamic gradient recalled imaging can be used to provide both types of information from magnitude and phase images, simultaneously. Such a combination of T_1 mapping and PRF-based thermometry has been applied successfully to radio-frequency-induced thermo-ablation in muscle and liver [15] and during the release of contrast agents from thermo-sensitive liposomes using the Look-locker technique [16, 17] for T_1 mapping while PRF temperature maps were extracted from the phase images [18]. Alternatively, T_1 mapping using the variable flip angle technique [19–21] has been proposed for T_1 based thermometry in adipose tissue taking into account the contributions from the different fatty acid components determined by a multi-point Dixon acquisition [22].

3.3 Online correction of respiratory-induced field disturbances for continuous MR-thermometry in the breast [23, 24]

3.3.1 Theory

Look-up-table-based correction A multi-baseline phase correction as detailed in sect. 1.2.3 has been implemented. In the case of respiratory-induced field changes a look-up-table-based approach is promising because it exploits the inherent periodical character of the breathing cycle. This is because the look-up-table provides a large set of reference images with each image representing a certain respiratory state. In this implementation, during the learning phase, the respiratory state is continuously monitored with help of a sensor such as a pencil-beam navigator placed on the diaphragm or a pressure sensor measuring thorax expansion. At the same time, phase, magnitude and temperature images are stored in a look-up-table according to the current respiratory state. During the

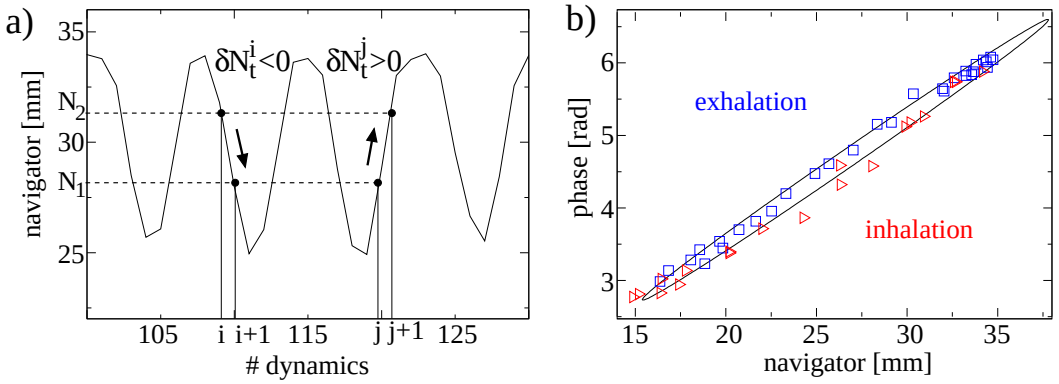

Figure 3.2: a) Separation of the navigator signal according to the current respiratory state shown for a sample of volunteer 5. Even though the navigator signal has the same value at time instants i/j and $i+1/j+1$ they belong to two different breathing phases. A negative (positive) temporal derivative δN_t^i (δN_t^j) of the navigator signal refers to exhalation (inhalation). b) Hysteresis of the respiratory cycle. The phase change in dependence of the navigator signal can be approximated by an ellipse (black solid line) where inhalation (red triangles) and exhalation (blue squares) follow different paths. The shown sample is taken from volunteer 5 for a learning phase length of 100 images.

intervention, for every new image, a correction image is identified in the look-up table by matching the current and the respiratory state pre-recorded during the learning phase. The phase of this matched image is chosen as reference correction phase ϕ_{corr} for the temperature calculation which is calculated using eq. (1.18). For the case of correcting MR-thermometry in the breast, artifactual magnetic field changes can be expected to be mainly caused by lung volume change which can be attributed to a combination of diaphragm displacement and thorax expansion. In general, during free-breathing both factors are not in-phase and can furthermore differ between the inspiration and the ex-

piration phase [25]. Depending on the type of sensor used, the monitored respiratory state is dominated by diaphragm displacements (navigator echo) or thorax expansion (pressure sensor). As an effect, phase shifts and hysteresis of different degrees between the observed respiration and the magnetic field changes can occur. In the proposed algorithm this is accounted for by sorting the navigator data according to the sign of their temporal derivative to identify the different respiratory states (Fig. 3.2a). Subsequently, both types of data are corrected independently with two separate look-up-tables.

Model-based correction A problem arises from the fact that the pre-recorded correction data cannot be sampled with infinite density. Time constraints or particular breathing patterns may lead to a poorly or irregularly populated look-up table, which, in turn, leads to discretization errors in the phase correction. In this case it is possible to extract the phase correction not directly from the look-up table, but from a model function which is calculated on a pixel-by-pixel basis from the table data [26]. In the present work two data models have been evaluated. The first model with two degrees of freedom

$$\phi(x) = ax + b \quad , \tag{3.1}$$

assumes a linear relationship between the image phase ϕ and the diaphragm position x, whereas the second model takes into account the effect of hysteresis and shifts between the values measured by the external sensor and the actual phase change by assuming an ellipsoidal dependence including three degrees of freedom

$$\frac{(x\cos\beta + \phi\sin\beta)^2}{a^2} + \frac{(\phi\cos\beta - x\sin\beta)^2}{b^2} = 1 \quad , \tag{3.2}$$

where a and b denote the minor and major semi-axis of the ellipse and β the tilt angle of the ellipse relative to the x-axis (Fig. 3.2b). An ellipse was chosen as the simplest approach which accounts for the fact that the respiratory induced displacements represent a closed loop.

Postprocessing In general the temperature precision for the presented experiments follows the relations given in sect. 1.2.4. Although the main temperature error is introduced by the magnetic field variations, small movements of the breast itself can contribute to displacements within the plane and also in the slice selection direction. Prior to correction, the images were masked and corrected for in-plane motion. Details of this algorithm can be found elsewhere [10]. Out-of-plane motion could not be compensated and led to small additional artifacts. Finally, the resulting temperature maps have been corrected for temperature offsets and linear main magnetic field drift [2].

Volunteer Experiments All experiments in this chapter were performed on a 1.5 T Achieva MR-scanner (Philips Medical Systems, Best, the Netherlands). Five healthy

female volunteers (age $23-27$) were placed in prone position and a 16-cm-diameter surface coil was used for signal registration. For PRF-thermometry a 2D radio-frequency-spoiled gradient recalled EPI multi-shot sequence ($T_E = 25\,\text{ms}$, $T_R = 72\,\text{ms}$, flip angle $30\,^\circ$, FOV $= 200 \times 160 \times 6\,\text{mm}^3$, matrix $= 128 \times 90$, coronal slice orientation, $15\,k$-space lines per excitation) was applied. In total 500 dynamic images were acquired with an acquisition time of 432 ms per image. The first 10 images were rejected to ensure steady state and the following 50 images were stored in the look-up table (learning phase). MR-thermometry was finally started after 60 images. In order to exclude the influence of fatty tissue on MR-thermometry, a 121 binomial water-selective pulse was applied for each excitation. The respiratory state was monitored by placing the 2D-selective pencil-beam directly on the diaphragm. The navigator signal was measured directly before each RF excitation leading to six navigator echoes per image. For the respiratory control, only the third navigator was used because it was acquired together with the center of k-space.
The imaging parameters were optimized to obtain a high SNR in order to evaluate the accuracy of the proposed correction. As an alternative, the acquisition can be accelerated by increasing the number of k-space lines per excitation in order to fully resolve the respiratory cycle. This was evaluated for two volunteers and leads to a frame rate of 4 images/s but at the cost of a lower SNR of 7 and a resulting increased theoretical temperature standard deviation of $1.8\,^\circ$C. For four volunteers the data sets were corrected in post-processing and for one in real-time. For the latter purpose, the resulting position together with phase and magnitude images were streamed to an in-house developed real-time reconstructor which performed phase corrections and temperature calculations online.

3.3.2 Results

Look-up-table-based correction Periodical magnetic field changes of 0.07 ppm to 0.25 ppm were observed in all volunteers. These values agree well with those reported by Sprinkhuizen et al. [27]. The corresponding artifactual temperature fluctuations show a maximal mag-

vol.	$\sigma_T^{\text{uncorr}}\ [^\circ C]$	$\sigma_T^{\text{corr}}\ [^\circ C]$ atlas-based	$\sigma_T^{\text{corr}}\ [^\circ C]$ linear	$\sigma_T^{\text{corr}}\ [^\circ C]$ ellipse	$\sigma_T^{\text{theor}}\ [^\circ C]$
1	3.5	1.0	0.8	1.0	0.8
2	2.6	1.5	1.5	1.6	1.1
3	3.8	1.1	0.8	0.9	0.7
4	5.4	2.1	2.1	6.1	1.4
5	11.6	2.2	1.7	3.3	0.9

Table 3.1: Temperature precision of the uncorrected images and of the images corrected with the basic look-up-table-based (atlas-based), the first order and second-order model-based approach and theoretical value of the temperature precision for all volunteers. These values were evaluated in ROI's marked by the brown arrows in Fig. 3.3.

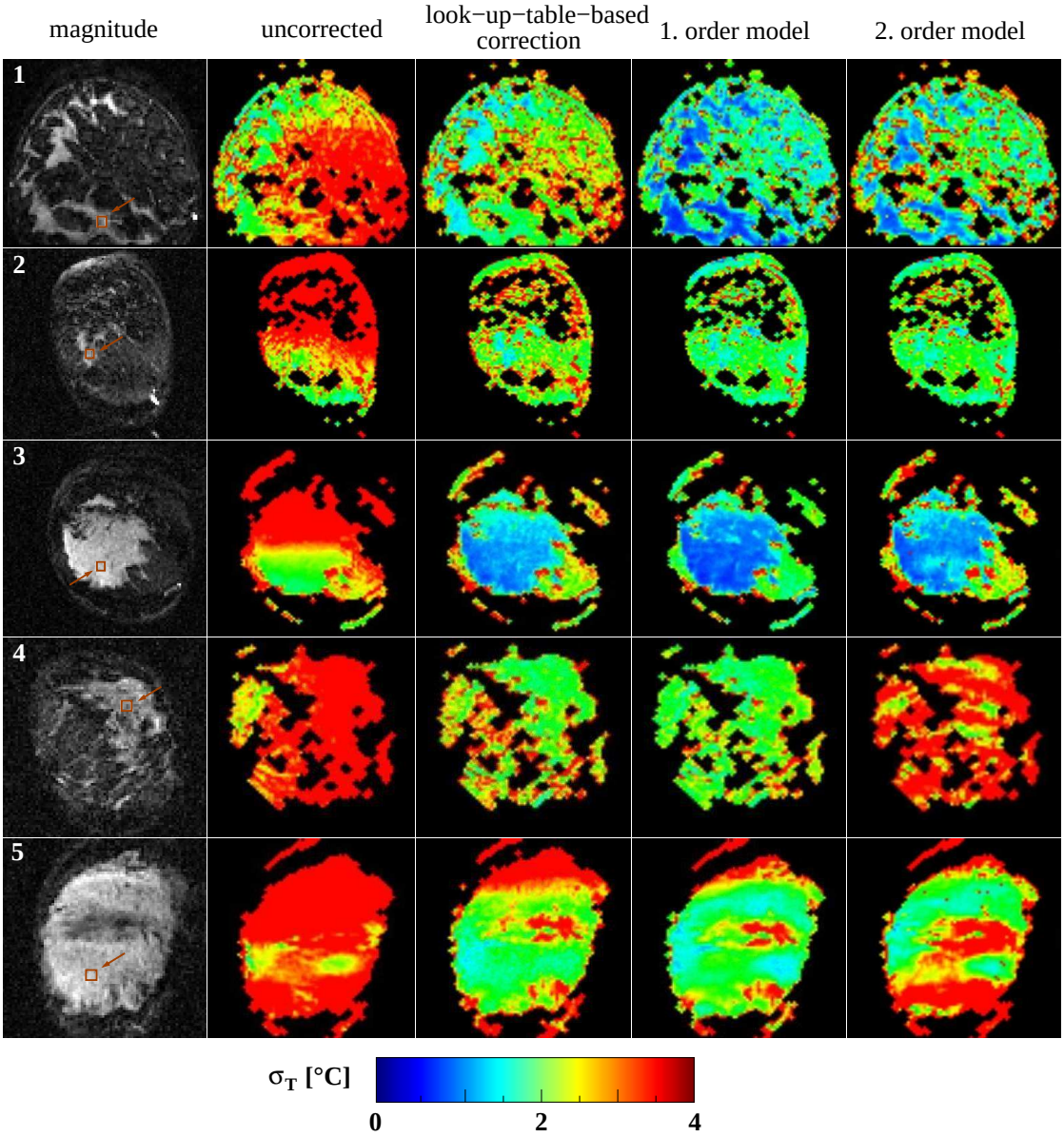

Figure 3.3: T_1-weighted image (first column) and drift and offset compensated maps of the standard deviation of the uncorrected (second column), the corrected temperature using the basic look-up-table-based correction (third column), the first order (fourth column) and second-order (fifth column) model-based correction. The regions of interest used for further evaluation are depicted by brown squares and arrows.

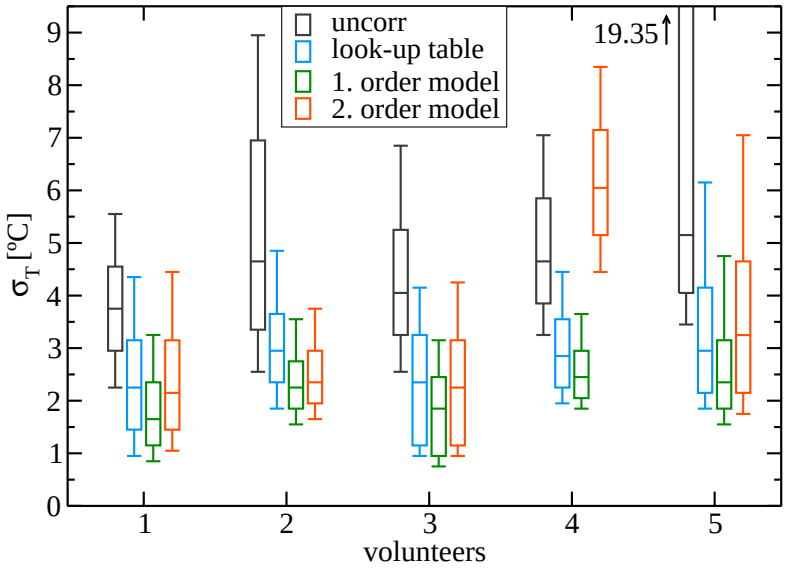

Figure 3.4: Box-Whisker plots of the temperature standard deviation. For each volunteer the given data corresponds to the uncorrected, corrected data using the basic look-up-table-based correction, corrected using the first order, and second-order model-based correction (from left to right). The box margins are given by the median and the values of the temperature standard deviation that comprise 25 % and 75 % of all considered data points. The whiskers are defined by the extreme values that are exceeded by 10 % and 90 % of all data points. The results are given for all five volunteers based on the data provided in Fig. 3.3.

nitude of 9 °C to 30 °C peak to peak across the volunteer data. Using eq. (1.15), the phase changes can be exploited to calculate temperature error maps. Figure 3.3 shows maps of the standard deviation of the uncorrected and corrected temperature along with the magnitude image of the right breast for all volunteers. The degree of thermometry errors differ largely from volunteer to volunteer due to variations of the breathing frequency ($7.0\,\mathrm{min}^{-1} - 20.0\,\mathrm{min}^{-1}$), amplitude (6 mm − 22 mm diaphragm displacement) and pulmonary volume. Furthermore, the position of the slice had to be adapted to the anatomy of the volunteers resulting in different distances from the thoracic cage. Figure 3.4 shows Box-Whisker plots of the temperature standard deviation taken from the maps presented in Fig. 3.3. Both the calculated medians as well as the 10 % and 90 % margins show a statistically significant reduction of the temperature standard deviation of the corrected data sets in comparison to the uncorrected data for all volunteers. A further analysis of the temperature evolution obtained from 5×5 ROIs selected within the breast shows that the proposed method is able to significantly improve the temperature precision by a factor of 1.7 to 5.3 (Table 3.1). In addition the corrections in post-processing (volunteer 1, 2, 3, and 5) and in real-time (volunteer 4) yield identical results. Furthermore, the achieved temperature uncertainty approaches the theoretical limit given by the averaged SNR within the selected ROI (eq. (1.19)). Figure 3.5

shows an example of the evolution of the temperature for the ROI specified in Fig. 3.3. There is a direct correlation between the respiratory state, which is monitored by the navigator, and the observed magnetic field changes and thus the artifactual temperature oscillations. Without any correction the temperature oscillates with a standard deviation of $\pm 3.5\,^{\circ}\mathrm{C}$ and peak-to-peak changes of up to $12\,^{\circ}\mathrm{C}$ following the breathing amplitude. For comparison, the dotted line shows the theoretical temperature precision limit $\sigma_T = 0.8\,^{\circ}\mathrm{C}$ given by the SNR of the image (eq. (1.19)). MR-thermometry with the accelerated data acquisition of 4 images/s resulted in temperature oscillations with a standard deviation of $\pm 1.8\,^{\circ}\mathrm{C}$ without correction and a standard deviation of $1.3\,^{\circ}\mathrm{C}$ when the look-up-table-based correction was applied. For the applied imaging protocol the transport to the external work station and reconstruction of one image data set took 29 ms, whereas phase corrections and temperature calculations required 50 ms. Hence, a maximal frame rate of 12 images/s is possible.

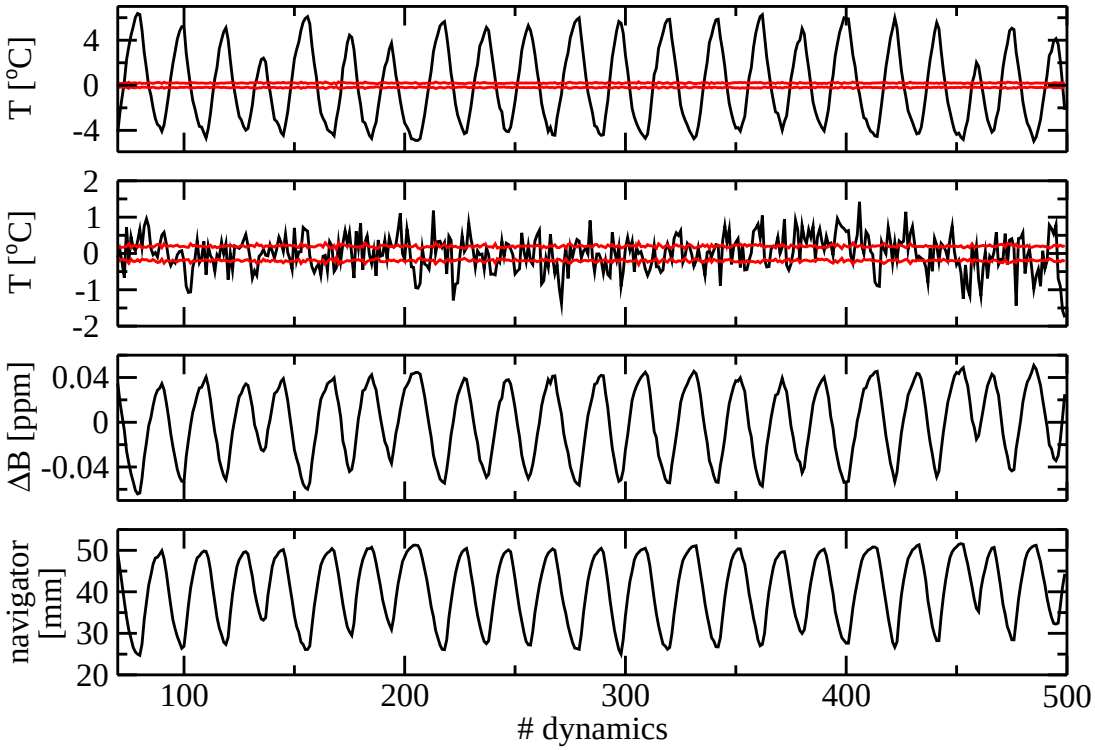

Figure 3.5: Results for Volunteer 1 taken in a representative region of interest (brown arrow in Fig. 3.3). From top to bottom: uncorrected temperature, corrected temperature, estimated magnetic field change, displacement measured by the pencil beam navigator. The red lines in the first two diagrams show the theoretical limit for the temperature accuracy given by the SNR of the image.

Model-based correction The described correction which is based on a phase model derived from the images acquired during the learning phase was applied to the data of all volunteers. The resulting maps of the temperature standard deviation for the first and second order correction are presented in column four and five of Fig. 3.3. A comparison with the look-up-table-based correction in the third row shows an overall improvement of the temperature precision for the linear model. The ellipsoidal model, on the other hand, only achieves comparable or better correction results as the look-up-table based approach for 3 of the 5 volunteer data sets. Similarly, Fig. 3.4 and Table 3.1 prove that a further reduction of the temperature standard deviation can be achieved if the first order model-based approach is applied. Again, the second order model-based approach cannot significantly improve the basic look-up-table-based approach and does even lead to worse

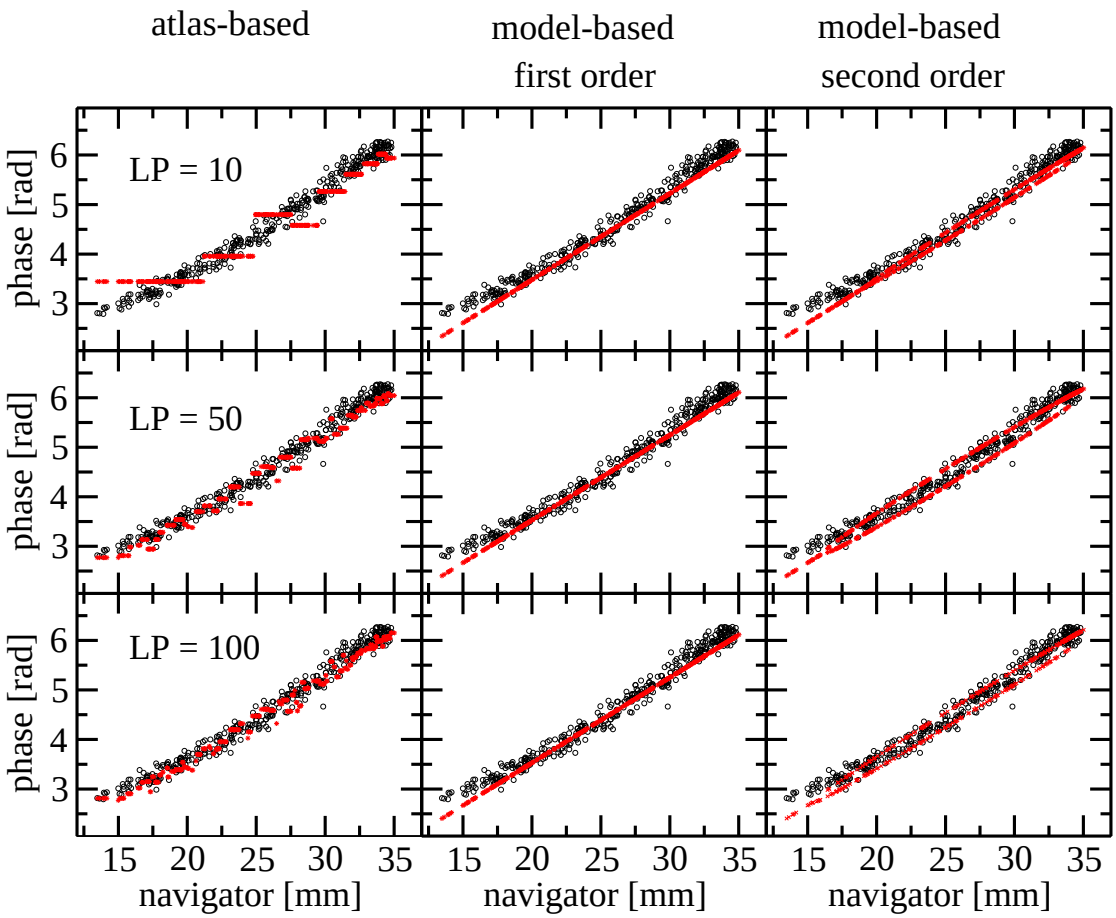

Figure 3.6: Measured phase (grey open circles) and corrected reference phase (red stars) for a characteristic point in the data of volunteer 5 with the purely look-up-table-based (atlas-based) correction (left), first order linear correction (middle) and second order correction based on an ellipsoidal fit (right). The results are shown for learning phase lengths of 10 (top row), 50 (middle row) and 100 (bottom row).

results in 2 cases. Figure 3.6 shows measured and corrected phase values as a function of the navigator displacement for the correction methods based on the conventional look-up-table, the first order linear phase model and the second order ellipsoidal fit of the phase data. All data values were taken from volunteer 5 in the representative ROI shown in Fig. 3.3. The phase values shown in the upper row, which are obtained with a learning phase length of 10 images, demonstrate the effect of a sparsely populated correction-table. In this case in average only one phase correction image per 1.88 mm displacement of the diaphragm is provided. Consequently, in the first diagram of the first row, the same correction phase is chosen for all navigator displacements within this range leading to a poor representation of the true phase behavior. An increased learning phase length of 50 (middle row) and 100 images (bottom row) leads to an improved resolution of 0.40 mm and 0.20 mm, whereas the model-based methods provide continuous correction data for both cases. The median temperature standard deviation given in Fig. 3.4 indicates that the first order model-based correction method is able to significantly improve the temperature precision by 16 % to 36 % for an average learning phase length compared to the purely atlas-based correction. Finally, an improvement by a factor of $\sqrt{2}$ as mentioned in sect. 1.2.4, could be achieved by neither of the two model-based approaches.

3.3.3 Discussion

The proposed correction strategy allows on-line access, calculation and correction of the MR-thermometry images during the treatment. As a result a corrected temperature map is available to the user before every new acquisition enabling direct therapy monitoring. Image acquisition can be carried out under free breathing conditions without the need for respiratory gating or breathhold techniques. Thus, the temporal resolution is significantly increased compared to previously proposed methods [28, 29]. In the presented experiment $20 - 40$ s of learning data providing 50 to 100 sampling points during the respiratory cycle were found to be sufficient to achieve on average a threefold reduction of the artifactual temperature fluctuations. Further improvement of $16 - 36$ % can be achieved by applying a linear data model to the pre-recorded phase data. Since the navigator provided data directly from the diaphragm, the observed phase changes were found to be in-phase with the measured respiratory state. Therefore, for the case of a well populated correction table, a second order correction did not lead to an improvement of the temperature accuracy. However, this might not be the case if the respiratory state is monitored by other means, such as a respiratory bellow or if a short learning phase length is chosen.
Sequences for MR-thermometry during free-breathing are always a compromise between acquisition speed, image quality and temperature precision. In the presented case an increased SNR was preferred, accepting the resulting lower acquisition speed. The use of a dedicated breast coil for signal registration could offer a remedy by allowing a faster acquisition while maintaining a comparable SNR. Furthermore, as breast tumors are known to contain only little or no fat [13] the same sequence parameters applied to MR-thermometry of breast tumors could yield a higher SNR despite the fat-selective

excitation pulse. Apart from this, residual temperature deviations may be due to the following factors. Because of the relatively long acquisition time of the images the k-space data was collected over a comparably long period of the respiratory cycle. As a result discretization errors in the case of a purely look-up-table-based correction are unavoidable. The model-based approach on the other hand requires the estimation of a functional dependence between the measured phase and the respiratory state which may not perfectly represent the true phase behavior. Finally, the assumption of the breast remaining stationary during the breathing cycle is not completely valid. While in-plane-motion could be corrected, out-of-plane-motion cannot be compensated by the applied algorithm. Provided that the employed imaging sequence is able to resolve the respiratory cycle, the proposed method is compatible with different motion sensors and sequence types which offers possibilities for future enhancements. The proposed method has no need for user feedback and can be used without prior knowledge.

3.4 Simultaneous PRF thermometry and T_1-based thermometry for temperature monitoring in the breast using variable flip angles

3.4.1 T_1 mapping techniques

Inversion recovery (IR) A standard inversion recovery sequence can be used to measure the longitudinal relaxation time. For this, several separate inversion recovery acquisitions with varying inversion delays T_I are carried out. The resulting signal in a voxel can be

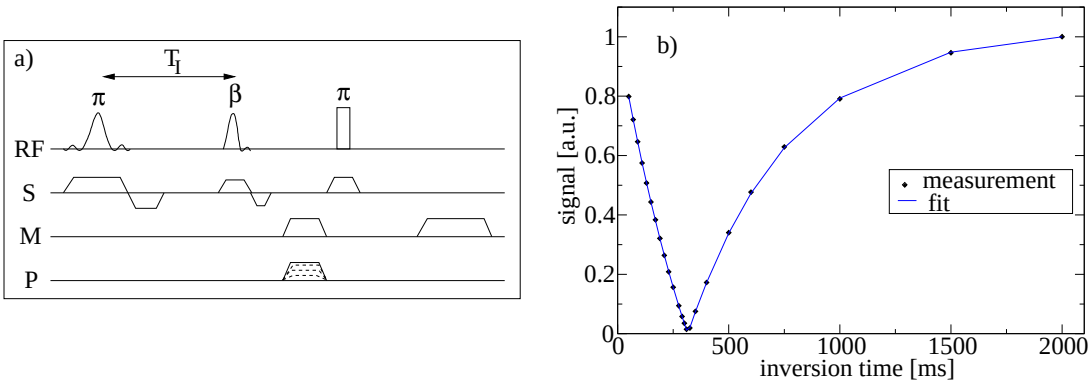

Figure 3.7: a) Inversion recovery spin echo sequence with inversion delay T_I. Shown are the schemes for the radio-frequency excitation pulses (RF) and the gradients in the readout (M), phase encoding (P), and slice select direction (S). b) Sample points of an inversion recovery measurement with $T_I = 50 - 2000$ ms (black squares) together with the fitted function (blue solid line).

described by the following expression

$$S(t) = M_0 \left(1 - \mathrm{e}^{-t/T_1}\right) + M_{ss} e^{-t/T_1} \approx M_0 \left(1 - 2\mathrm{e}^{-t/T_1}\right) \quad , \tag{3.3}$$

where M_0 is the equilibrium magnetization and α is the flip angle of the initial inversion pulse $\alpha = \pi$. M_{ss} is the longitudinal steady state magnetization for the given T_1 and T_R, which for $T_R \gg T_1$ can be approximated by $M_{ss} \approx M_0$. In this case, T_1 can be derived by a simple least squares fit of the form $S = a - b\mathrm{e}^{-t/T_1}$ Fig. 3.7 shows such a recovery curve and the corresponding fit. One disadvantage of this method is that the need for complete relaxation limits the achievable temporal and spatial resolution.

Look-Locker (LL) An improved version of the inversion recovery T_1 mapping technique has been proposed by Look and Locker [30] and was later adapted to MR imaging [16]. This method uses a train of low flip angle interrogation pulses β to create a train of gradient echoes with constant inversion intervals T_{I2} between the excitations (Fig. 3.8a). As a result, the relaxation of the longitudinal magnetization M_z is modified depending

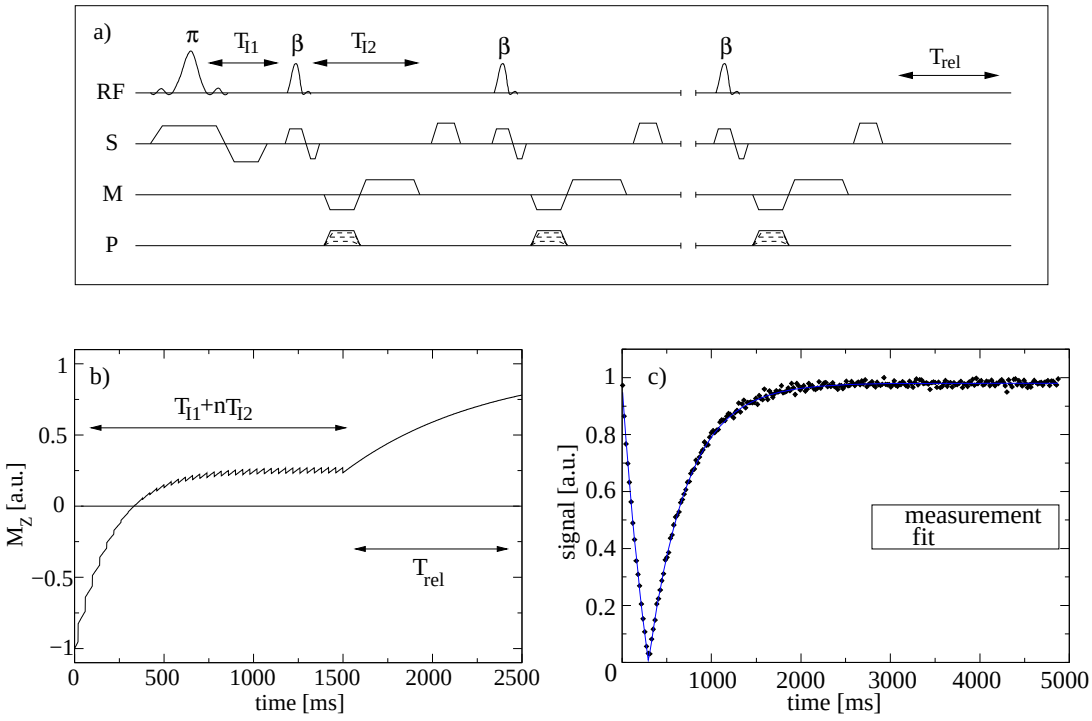

Figure 3.8: a) Look Locker sequence with inversion delays T_{I1} and T_{I2} and undisturbed recovery period T_{rel}. b) Simulation of the temporal evolution of the longitudinal magnetization M_z for a Look Locker sequence with $T_{I1} = 20\,\mathrm{ms}$, $T_{I2} = 40\,\mathrm{ms}$, $T_{\mathrm{rel}} = 500\,\mathrm{ms}$, flip angle $\beta = 30\,^\circ$ and $T_1 = 800\,\mathrm{ms}$. The maximal inversion delay was 1500 ms. c) Sample points of a Look Locker measurement with $T_{I1} = 5.6\,\mathrm{ms}$, $T_{I2} = 19.1\,\mathrm{ms}$, $\beta = 6\,^\circ$ and $T_1 \sim 450\,\mathrm{ms}$. The maximal inversion delay was 4909 ms.

on the flip angle β and the inversion interval T_{I2}. The longitudinal magnetization after the n^{th} excitation is given by [17]

$$M_z^n = M_z^{ss}\left(\cos\beta \mathrm{e}^{-T_{I2}/T_1}\right)\left(M_z^1 - M_z^{ss}\right) \tag{3.4}$$

with the steady state magnetization M_z^{ss} and the longitudinal magnetization just before the first interrogation pulse M_z^1. Figure 3.8b shows a simulation of the temporal evolution of M_z. The continuous application of the interrogation pulse results in a relaxation with an apparent relaxation rate $R_1^* = R_1 - \ln(\cos\beta)/T_{I2}$ [17]. Taking this into account, the longitudinal relaxation time can be derived from a least squares fit of the acquired signal recovery curve as shown for the inversion recovery T_1 mapping technique. An example of such an experimentally acquired relaxation curve and the corresponding fitted function is shown in Fig. 3.8c. The achievable temporal resolution can be significantly reduced compared to inversion recovery methods, and comparable T_1 precisions have been reported [31]. However, the minimal acquisition time is still limited by the need for complete relaxation and the necessary fitting procedure introduces additional computational overhead.

Variable flip angles (VFA) The steady-state signal amplitude S of a spoiled gradient echo sequence for $T_R \gg T_2^*$ is a function of the flip angle α, T_1 and the repetition time T_R

$$S = M_0 \frac{\sin\alpha\,(1 - E_1)\,E_2}{1 - E_1\cos\alpha} \quad , \tag{3.5}$$

with $E_1 = \exp(-T_R/T_1)$ and $E_2 = \exp(-T_E/T_2^*)$. This equation can be parameterized for a linear relation $y = ax + b$ with

$$x = \frac{S}{\tan\alpha} \quad \text{and} \quad y = \frac{S}{\sin\alpha} \quad . \tag{3.6}$$

After the slope $a = \exp(-T_R/T_1)$ has been retrieved by linear regression, the spin-lattice relaxation time can be determined as [19]

$$T_1 = -\frac{T_R}{\ln a} \quad . \tag{3.7}$$

3.4.2 Choice of the optimal T_1 mapping technique

The choice of the respective T_1 mapping technique depends heavily on the application. For the combination with PRF thermometry, the method has to be compatible with gradient echo sequences and sufficiently fast to allow online PRF thermometry and the detection of T_1 changes. Inversion recovery sequences are therefore not suitable since the need for complete relaxation limits the achievable temporal resolution considerably. The Look-Locker approach on the other hand, has already been used for this purpose with a temporal resolution of approximately 4 s [18]. However, as this method relies

also on the observation of the longitudinal relaxation process, the achievable temporal resolution is always limited by the maximal required inversion delay for the given T_1. Moreover, the determination of the temperature requires time-consuming data processing and introduces signal weighting. VFA T_1 mapping is not limited by relaxation and could therefore achieve higher temporal resolutions. Furthermore, a simple gradient echo sequence with optimized parameters can be used for VFA T_1 mapping making it the ideal candidate for the present application.

3.4.3 Optimization of the imaging sequence

In general, a sequence for the monitoring of tissue heating using PRF thermometry has to fulfill certain requirements. A temporal resolution of $1-2\,\mathrm{s}$ or better is desirable to resolve the heating process. An in-plane resolution of $< 2\,\mathrm{mm}$ allows to identify small anatomical details and the exact position of the hot spot. Finally, echo time and SNR are directly related to the temperature precision as described earlier (eq. (1.20)). On the other hand, the determination of T_1 using variable flip angles requires additional conditions to be fulfilled. As a result, the final sequence for simultaneous PRF thermometry and T_1 mapping represents by force a compromise.

Flip angles It has been shown that, for a given range of T_R/T_1, two flip angles with optimized values are sufficient to minimize the error in T_1 [32].
These two optimized flip angles $\alpha_{1,\mathrm{opt}}/\alpha_{2,\mathrm{opt}}$ can be found by maximizing the product of the normalized dynamic range (DR) and the fractional signal (FS) [33] which are given by the following expressions

$$\begin{aligned} \mathrm{DR} &= \frac{S_{\alpha_1}}{M_0 \sin\alpha_1} - \frac{S_{\alpha_2}}{M_0 \sin\alpha_2} \\ \mathrm{FS} &= \frac{S_{\alpha_1} + S_{\alpha_2}}{2S_{\alpha_E}} \quad . \end{aligned} \tag{3.8}$$

Here, S_{α_1} and S_{α_2} represent the signals for each flip angle and S_{α_E} is the maximal signal achievable using the Ernst angle $\alpha_E = \arccos E_1$ [34] with $E_1 = \mathrm{e}^{T_R/T_1}$. For $T_R = 18\,\mathrm{ms}$ and a T_1 range of 100 ms to 800 ms, optimal flip angles of $\alpha_{1,\mathrm{opt}} = 44\,^\circ$ and $\alpha_{2,\mathrm{opt}} = 7\,^\circ$ have been found. After signal optimization, $\alpha_1 = 49\,^\circ$ and $\alpha_2 = 9\,^\circ$ were chosen for the experiments in this work.

Steady state For precise T_1 measurements, steady-state has to be guaranteed by radio-frequency (RF) or gradient spoiling and a sufficient number of start up echoes [35]. Steady state is assumed if

$$\left| \frac{M_z(n) - M_z(n-1)}{M_0} \right| < 0.001 \quad . \tag{3.9}$$

As a result, $n = 12$ to 73 excitations are required for the chosen flip angles and T_1 range.

Slice profile The precise knowledge of the flip angle α has to be ensured for accurate T_1 mapping. B_1 mapping can eliminate the effects of in-plane inhomogeneities of the RF excitation field. For the following experiments a 3D multi-T_R sequence has been used for B_1 mapping [35].
Ideally, the flip angle should be equal for all spins in the selected slice. However, for 2D excitations, this is not the case since the slice profile for a finite excitation pulse will not be rectangular. 3D acquisitions provide in theory a homogeneous flip angle for the central slices. As they are time consuming and prone to motion artifacts, 2D acquisitions are preferable for real-time experiments. For these applications, the excitation pulse can be optimized in order to find a compromise between pulse duration and slice profile. For this reason, several different excitation pulses have been evaluated for their slice profile and the resulting T_1 accuracy in comparison with a standard inversion recovery measurement. All experiments in this chapter were carried out on a 1.5 T Achieva MR-scanner (Philips Healthcare, Best, the Netherlands). In a first experiment, the slice profiles for different excitation pulses were determined. A cylindrical phantom (1 l demineralized water + 770 mg $CuSO_4 \cdot 5H_2O$ + 2000 mg NaCl + 1 ml arquad (1 % solution) + 0.05 ml H_2SO_4 − 0.1N solution) was placed in the MR scanner and a 6-channel-head coil was used for signal registration. The following sequence, taking into account the results obtained above, was used: TFE-EPI (transient field echo with EPI readout), 7 k-space lines per excitation, $T_R = 374 - 376$ ms, $T_E = 23 - 25$ ms, FOV $= 40 \times 102 \times 6\text{mm}^3$, $\alpha_1/\alpha_2 = 49/9°$, voxel $= 0.15 \times 0.15 \times 6\text{mm}^3$, 32 averages. The slice profile was acquired by changing the encoding direction of the readout gradients to the slice select direction.
Figure 3.9 shows the slice profiles for four different excitation pulses (block pulse, four

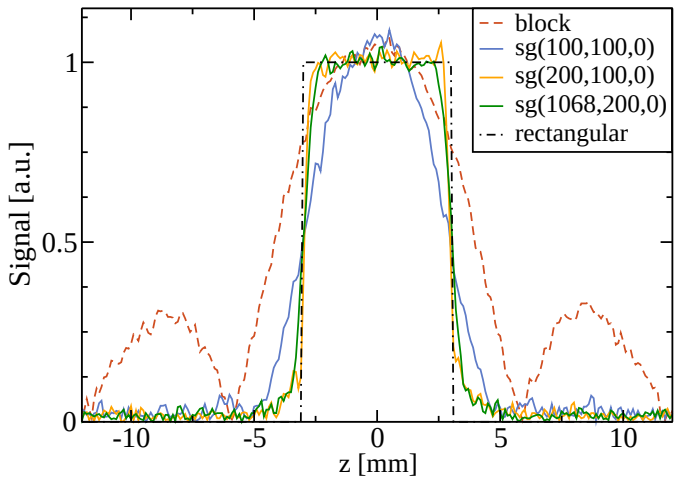

Figure 3.9: Comparison of the slice profiles for four different excitation pulses. sg(α, β, γ) represents a sinc-gaussian excitation pulse with $\alpha/100$ sinc lobes, $\beta/100$ Gauss deviations and a temporal offset γ. The slice thickness was 6 mm.

sinc-gaussian pulses with different truncations and a pulse duration increased by 0.3 ms, 1.7 ms, and 4.8 ms compared to the block pulse). $\mathrm{sg}(\alpha, \beta, \gamma)$ represents a sinc-gaussian excitation pulse with $\alpha/100$ sinc lobes, $\beta/100$ Gauss deviations and a temporal offset γ. For clarity reasons, the $\mathrm{sg}(500, 200, 0)$ slice profile is not shown since it is similar to those for the $\mathrm{sg}(200, 100, 0)$ and the $\mathrm{sg}(1069, 200, 0)$ pulse. The pulse duration for this pulse is increased by 0.6 ms compared to the block pulse. The block pulse leads to apparent side lobes outside the desired slice area and an increased apparent slice thickness of approximately 30 % (full width half maximum (FWHM)). The comparison with the optimal rectangular slice profile (black solid line) and the sinc-gaussian pulses shows good agreement for the slice thickness (FWHM). In particular, there is only little improvement if the $\mathrm{sg}(500, 200, 0)$ or the $\mathrm{sg}(1068, 200, 0)$ pulses are used instead of the $\mathrm{sg}(200, 100, 0)$ pulse.

In a second experiment, the calculated T_1 values for different excitation pulses were compared to a standard inversion recovery T_1 measurement in order to determine the achievable T_1 accuracy. A cylindrical agarose gel phantom (2 % agarose, diameter 2.5 cm, height 4 cm, doped with 20μl Gadolinium (Prohance)) was placed in the MR-scanner and a surface coil (47 mm diameter) was used for signal registration.

In order to meet the requirements of a real-time heating experiment mentioned above, the following sequence parameters were chosen: TFE-EPI, 7 k-space lines per excitation, matrix 256×64, 7 startup echoes, $\alpha_1/\alpha_2 = 49/9\,^\circ$, voxel $1 \times 1 \times 3\mathrm{mm}^3$, 4 averages. RF spoiling (phase increment 150 °) and improved gradient spoiler were applied to destroy residual transverse magnetization. The different repetition times and echo times as a result of the different pulse durations are summarized in the second column of Table 3.2. In order to achieve a sufficient number of excitations, the flip angle was changed only every second dynamic scan. As a result, T_1 maps were calculated only every fourth dynamic scan ($\Delta t_{\mathrm{VFA}} \sim 4\,\mathrm{s}$) while PRF thermometry could be performed every dynamic

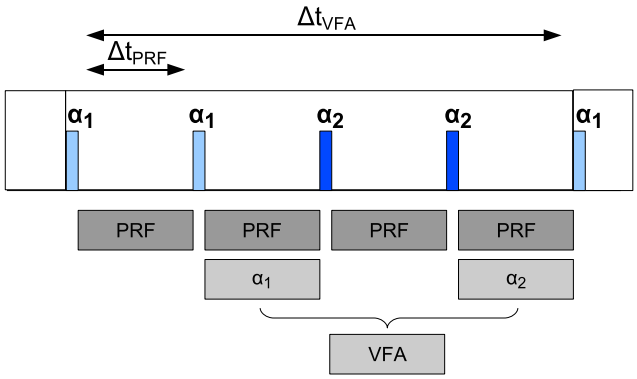

Figure 3.10: Scheme of the applied sequence: The flip angle is varied every two dynamic acquisitions. While every image is used for PRF-based thermometry, only the last image for every flip angle serves for the T_1 calculation according to eq. (3.7) to ensure the steady state.

excitation pulse	T_R/T_E [ms]	$T_{1,\mathrm{meas}}/T_{1,\mathrm{IR}}$
block	16/7.7	0.73
sg(100, 100, 0)	17/8.1	0.44
sg(200, 100, 0)	18/8.8	0.80
sg(500, 200, 0)	22/11.0	0.74
sg(1068, 200, 0)	30/15.0	0.91
3D		1.10

Table 3.2: The second column illustrates the increase in T_R/T_E if more complex excitation pulses are used. The third column shows the ratio between the T_1 values measured by the variable flip angle sequence with each of the excitation pulses and the T_1 values measured by the standard inversion recovery sequence. The T_1 values represent the average values in a ROI in the center of the phantom ($T_{1,\mathrm{IR}} = 287\,\mathrm{ms}$). The last row shows the result for a 3D variable flip angle acquisition.

scan to reach steady state ($\Delta t_{\mathrm{PRF}} \sim 1\,\mathrm{s}$). This principle is also illustrated in Fig. 3.10. An inversion recovery sequence with a multiple-spin-echo readout-train (Turbo spin echo or RARE, $T_R = 5\,\mathrm{s}$, 23 inversion times from 50 to 2000 ms, voxel $1 \times 1 \times 3\,\mathrm{mm}^3$, matrix 256×64) was used as a reference for the T_1 measurements.
In addition, the variable flip angle sequence was tested as a 3D implementation (3 reconstructed slices, $T_R/T_E = 103/51\,\mathrm{ms}$, $\Delta t_{\mathrm{PRF}} = 4.9\,\mathrm{s}$). The resulting T_1 maps are displayed in Fig. 3.11 and in the third column of Table 3.2 the ratio between the values measured by variable flip angle and by the inversion recovery sequence are displayed for

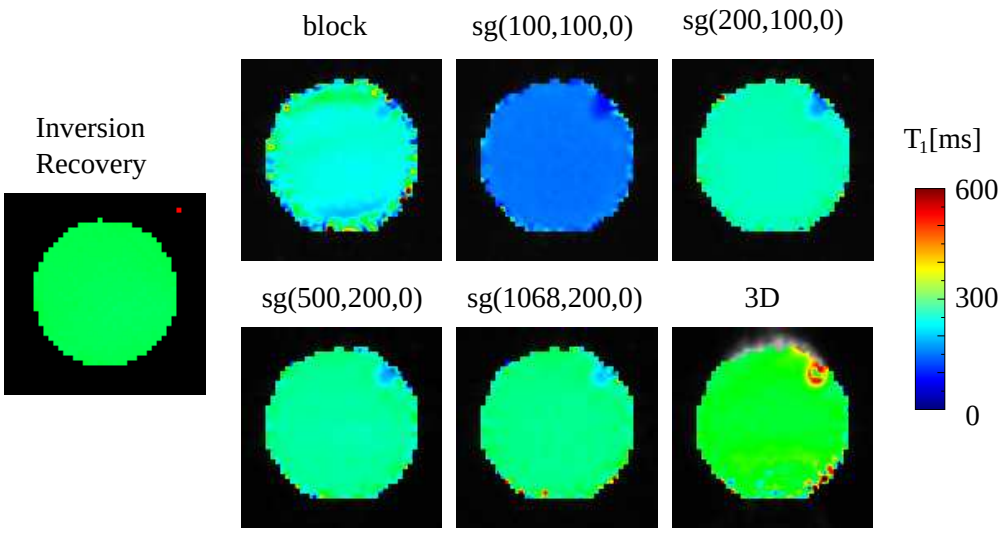

Figure 3.11: T_1 maps for the standard inversion recovery sequence and for the variable flip angle sequences with different excitation pulses including a 3D implementation.

a ROI in the center of the phantom. All variable flip angle sequences underestimate T_1 by 9 % to 27 % for the block pulse which coincides with the deviations from the optimal rectangular slice profile in Fig. 3.9. Only the 3D implementation overestimates T_1 by 10 % .
As expected, the most complex excitation pulse achieved the smallest error even compared to the 3D acquisition. However, both the sg(100, 100, 0) and the sg(500, 200, 0) pulse show remarkable poor T_1 accuracies comparable to or worse than the block pulse. As a compromise between T_1 accuracy and scan time, the sg(200, 100, 0) pulse (1.67 kHz bandwidth) was chosen as excitation pulse for the following experiments.

3.4.4 Calibration of the temperature dependence of T_1 in porcine fat

The temperature dependence of T_1 of the porcine fat sample was determined in a calibration experiment. For this purpose, the porcine fat sample was heated in 5 °C steps in a water bath covering a temperature range of 20 °C to 70 °C. In order to ensure thermal equilibrium, image acquisition was started after 20 min at constant temperature. For T_1 measurements, the VFA sequence described above was adapted to the size of the sample: TFE-EPI sequence, echo train length = 7, T_R/T_E = 18/9.1 ms, bandwidth in readout direction = 777 Hz, matrix = 256 × 256, voxel size = 1 × 1 × 6 mm^3, α_1/α_2 = 49 °/9 °, 7 start up echoes, 4 averages. With a dynamic scan time of 3.1 s, a T_1 map was available every 12.4 s. B_1 inhomogeneity was corrected by acquiring a B_1 map prior to image acquisition using a 3D RF-spoiled multi-T_R gradient echo sequence (T_E = 1.48 ms, T_{R1}/T_{R2} = 23/115 ms, flip angle = 70 °, FOV = 250 × 250 × 42, matrix = 64 × 63, voxel size = 4 × 4 × 6 mm^3, bandwidth in readout direction = 1085 Hz, 7 slices) with increased gradient spoiler amplitudes. In order to evaluate the stability of the T_1 measurements,

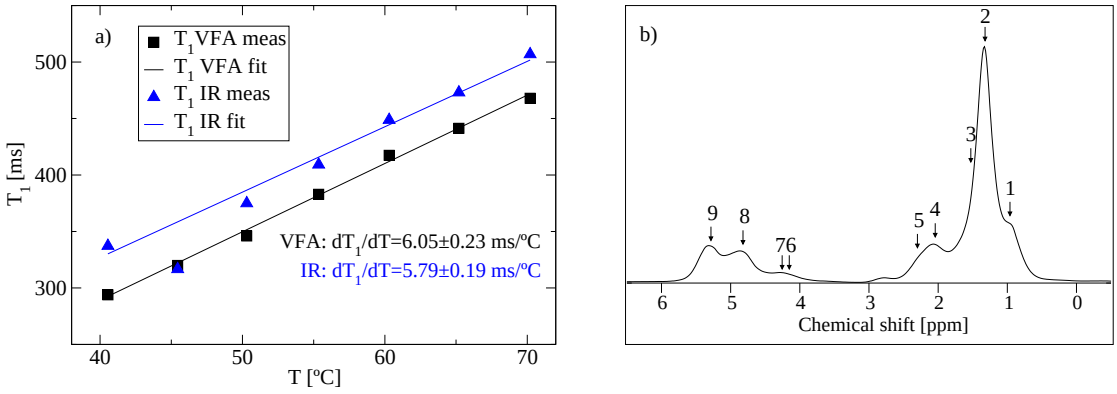

Figure 3.12: a) Results of the calibration experiment: The change of T_1 with temperature is shown for the sequence using variable flip angles (VFA, black squares) in comparison with a standard inversion recovery sequence (IR, blue triangles). A linear regression results in the solid lines with the slopes dT_1/dT as indicated in the image. b) Single voxel spectrum of the porcine fat sample acquired at 1.5 T. 1: CH_3 2: $(CH_2)_n$ 3: O=C-CH_2-CH_2 4: C=C-CH_2 5: C-CH_2-C= 6: CH_20 (left) 7: CH_20 (right) 8: CHO 9: CH=CH

48 images (12 T_1 maps) were acquired. As a reference, T_1 was measured with an inversion recovery sequence using a TSE readout ($T_R/T_E = 5000/26\,\mathrm{ms}$, acceleration factor 32, matrix = 124×107, voxel size = $2 \times 2 \times 6\,\mathrm{mm}^3$, bandwidth in readout direction = 1581 Hz, 23 inversion times between 50 ms and 1750 ms). The change of T_1 with temperature $\mathrm{d}T_1/\mathrm{d}T$ was calculated using linear regression of the measured T_1 values versus temperature.
The results for the calibration of $\mathrm{d}T_1/\mathrm{d}T$ are shown in Fig. 3.12a for a temperature range of 40 °C to 70 °C. The inversion recovery measurement for 45 °C had to be removed due to measurement artefacts. Both the measurements using inversion recovery, as well as those using variable flip angle show a linear dependence of T_1 with temperature. In addition, there is a constant offset of approximately 35 ms between the T_1 values measured with variable flip angle and inversion recovery. The deviation given for $\mathrm{d}T_1/\mathrm{d}T$ represents the quality of the linear regression. For the following experiments, the determined value of $\mathrm{d}T_1/\mathrm{d}T = 6.05\,\mathrm{ms/K}$ was used.
In order to further investigate the nature of the determined temperature dependence, the composition of the fatty parts of the sample was examined in more detail. Fat represents a composite of different fatty acids with varying volume fractions and different relaxation behavior. Especially the main components CH_2 and CH_3 possess a considerable difference in the temperature dependence of T_1 as recently shown at 11 T [36]. A single voxel spectrum of the fatty part of the used sample was acquired using a dedicated PRESS sequence (VOI size = $8 \times 8 \times 8\,\mathrm{mm}^3$, $T_E = 25\,\mathrm{ms}$, $T_R = 2\,\mathrm{s}$, spectral resolution = 2 Hz/point, 512 samples, 128 averages). The resulting spectrum is shown in Fig. 3.12b. Even though not all fatty acid peaks have been resolved at this field strength, the major components can be identified visually. The volume fractions of the

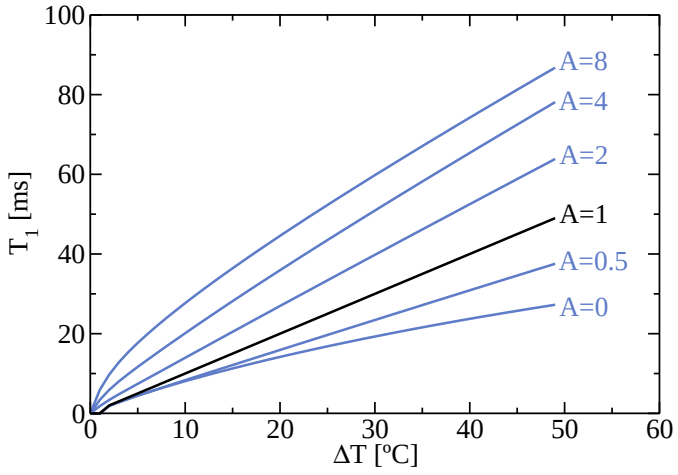

Figure 3.13: T_1 versus temperature measured with the VFA technique for different ratios $A = \dfrac{\mathrm{d}T_1/\mathrm{d}T\,(\mathrm{R})}{\mathrm{d}T_1/\mathrm{d}T\,(\mathrm{CH_2})}$ and $\mathrm{d}T_1/\mathrm{d}T\,(\mathrm{CH_2}) = 1\,\mathrm{ms/°C}$.

different components were determined by fitting a gauss-lorentzian peak profile to the data and evaluating the peak area. For the two main components, volume fractions of $v_{\mathrm{CH_2}} = 0.60$ and $v_{\mathrm{CH_3}} = 0.06$ were found. In analogy to eq. (3.5) for a single component, the observed steady state signal S_{ss} in fat with n different components is formed by the weighted sum of the signal contributions of the different fatty acids i with $T_{1,i}$, $T^*_{2,i}$, and volume fraction v_i

$$S_{ss} = M_0 \sum_{i=0}^{n} v_i \frac{\sin\alpha \left(1 - \mathrm{e}^{-TR/T_{1,i}}\right) \mathrm{e}^{-TE/T^*_{2,i}}}{\left(1 - \mathrm{e}^{-TR/T_{1,i}} \cos\alpha\right)} \quad . \tag{3.10}$$

As a result, the T_1 measured by the VFA technique and the values of $\mathrm{d}T_1/\mathrm{d}T$ derived from these measurements depend heavily on the contributions of every component. Considering CH_2 and CH_3 with $\mathrm{d}T_1/\mathrm{d}T\,(\mathrm{CH_2})$, $\mathrm{d}T_1/\mathrm{d}T\,(\mathrm{CH_3})$, and assuming that the remaining fatty acids show a homogeneous relaxation behavior with $\mathrm{d}T_1/\mathrm{d}T\,(\mathrm{R})$, the temperature dependence of T_1 with temperature observed by the VFA technique can be modeled by three components. For the presented experiment, the contribution of CH_3 is negligible and will thus not be considered in the following. The resulting T_1 versus temperature measured with the VFA technique are displayed in Fig. 3.13 for different ratios $A = \dfrac{\mathrm{d}T_1/\mathrm{d}T\,(\mathrm{R})}{\mathrm{d}T_1/\mathrm{d}T\,(\mathrm{CH_2})}$. If $\mathrm{d}T_1/\mathrm{d}T\,(\mathrm{CH_2})$ is taken as reference value, errors in the determination of $\mathrm{d}T_1/\mathrm{d}T$ of $-46\,\%$ up to $61\,\%$ can be observed for the examined ratios A. In addition, for $A \neq 1$ the temperature dependence of T_1 becomes nonlinear.

3.4.5 Heating in porcine fat and muscle

The ability to perform thermometry in muscle and fatty tissue simultaneously was evaluated using high-intensity focused ultrasound (HIFU) heating. A sample (diameter = 4 cm, height = 2.5 cm) containing both porcine muscle and fat was placed on a single element ultrasound transducer (focal length = 8 cm, aperture = 12 cm, operating frequency = 1.5 MHz, Imasonic, Besançon, France,) which was integrated into a conventional MRI examination bed. The focal point was positioned at the interface between muscle and fatty tissue and two fluoroptic temperature probes (type STB, LumaSense Technologies, Santa Clara, CA, USA, accuracy 0.2 °C, precision 0.1 °C, temporal resolution 1 s) were placed in the muscle and the fatty tissue in a distance of approximately 5 mm from the focal point, respectively, in order to monitor the true temperature rise. Heating was performed by applying 20 W electrical power to the HIFU transducer over a period of 18 min. For simultaneous T_1 measurements and PRF thermometry, the VFA sequence developed in sect. 3.4.3 was used for image acquisition and a circular surface coil with 47 mm diameter was used for signal registration. As described in Fig. 3.10, PRF thermometry was performed with every dynamic scan ($\Delta t_{\mathrm{PRF}} = 1.16\,\mathrm{s}$), while T_1 maps were calculated only every fourth dynamic scan in order to ensure steady state ($\Delta t_{\mathrm{VFA}} = 4.64\,\mathrm{s}$). As B_1 variations over the FOV were found to be negligible, no B_1 correction was performed.

Figure 3.14a shows the T_1 temperature map acquired at the hottest time frame indicating that the temperature rise in the fatty tissue was on the order of 20 °C. Based

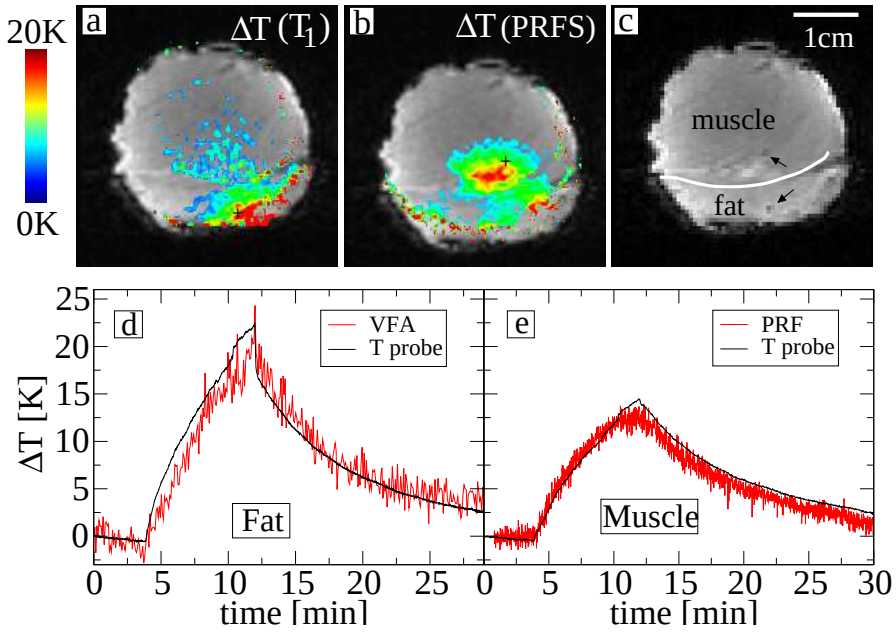

Figure 3.14: Top: Temperature maps taken at the hottest time frame measured with T_1 thermometry (a) and PRF thermometry (b). The distribution of fat and muscle tissue in the sample is displayed in (c) and the positions of the temperature probes are indicated by black arrows. Bottom: Temperature graphs measured by T_1 thermometry in the fatty tissue (d) and by PRF thermometry in the muscle tissue (e) (solid red lines) as indicated by the black crosses, and the corresponding temperatures measured by the temperature probes (solid black line).

on the presented calibration experiment, the value for the temperature dependence of T_1 was chosen as $\mathrm{d}T_1/\mathrm{d}T = 5.8\,\mathrm{ms/°C}$. A comparison of the measured temperature rise using T_1 and the temperature rise measured with the temperature probe at one point is displayed in Fig. 3.14d and shows a good correspondence with an accuracy of $\sigma_T = (2.5 \pm 2.7)$ °C. The temperature map calculated using PRF thermometry is shown in Fig. 3.14b where the focal point position is clearly visible. Moreover, the graph in Fig. 3.14e shows a good correspondence between the measured temperature rise and the values obtained with the temperature probe. The accuracy was found increased compared to T_1 thermometry with a value of $\sigma_T = (1.2 \pm 1.4)$ °C. Finally, Fig. 3.14c allows the identification of the muscle tissue on top and the fatty tissue on the bottom. The precision of the PRF and T_1 temperature measurements for this experiment were found to be 0.6 °C and 1.1 °C respectively.

3.4.6 Discussion

It has been shown that combined PRF-based thermometry and T_1 mapping using VFA is feasible for both simultaneous temperature measurements in fat and muscle, as well as for monitoring temperature-induced release of T_1 contrast agents.

Compared to existing alternative methods for simultaneous T_1 mapping and PRF thermometry, the presented method shows several advantages: While conventional T_1 weighted gradient echo imaging with the assumption of proportionality between the image signal and T_1 [15], can achieve higher temporal resolutions for the T_1 determination, the available T_1 information has only qualitative character. Alternatively, the Look-Locker approach for simultaneous PRF thermometry and T_1 mapping [18] provides precise T_1 information with a temporal resolution of 4.4 s for both thermometry and T_1 mapping. However, the phase has to be extracted from the collection of phase images acquired at different inversion times, leading to additional computational overhead and SNR weighting. This is also the case for the determination of T_1 from the reconstructed recovery curve where fitting is required. The determination of T_1 using VFA, however, can be reduced to a simple arithmetic operation making it suitable for online calculation. Furthermore, for a comparable temporal resolution, the Look Locker sequence provided 7 times less efficient sampling leading to a significantly lower spatial resolution than in the implementation proposed here. In contrast to that, the implementation presented in this work provides a spatial resolution of 1 mm in-plane and 3 mm through-plane in combination with a temporal resolution of $\Delta t_{\mathrm{PRF}} = 1.2\,\mathrm{s}$ for PRF- and $\Delta t_{\mathrm{VFA}} = 4.6\,\mathrm{s}$ for T_1 mapping allowing the detection of spatial details as well as monitoring of temporal trends. For VFA T_1 measurements, B_1 mapping is required prior to the measurements in order to correct for B_1 inhomogeneities. However, assuming a B_1 distribution with only small spatial variations which remains unchanged during the experiment, the acquisition of one low resolution B_1 map at the beginning of the experiment is sufficient introducing only a negligible time penalty. If only T_1 changes are to be measured in a sufficiently homogeneous target area, B_1 mapping may be omitted entirely. Slice profile optimization is crucial for accurate T_1 quantification and for 2D acquisitions errors due to deviations from the optimal rectangular slice profile have to be taken into account.

PRF- and T_1-based thermometry in porcine fat and muscle The achieved temperature accuracies of 2.5 °C and 1.2 °C for T_1- and PRF-based thermometry in biological tissue suggest that the monitoring of the temperature evolution during ablations in breast tumors as well as in the surrounding fatty tissue is possible with the proposed approach. In this study, no fat suppression was applied, which might lead to inaccuracies in the PRF-based temperature measurements. Breast tumors, however, have been reported to contain only negligible quantities of fat [13]. The largest uncertainty for T_1-based temperature measurements arises from the calibration values $\mathrm{d}T_1/\mathrm{d}T$ used for the temperature calculations. In the calibration experiment presented here, a linear behavior of the T_1 of fat and temperature was found with an offset between the T_1 values measured by variable flip angle and inversion recovery. This offset can be attributed to an incomplete B_1 correction or the imperfect slice profile as demonstrated in sect. 3.4.3, but did not bias the determination of the temperature dependence of T_1. Due to the complexity of the relaxation behavior of fat, the volume fractions and relaxation times of the different components have large influence on the measured T_1. For the case where the remaining fatty acids (apart from CH_2 and CH_3) have a considerable different

dT_1/dT than CH_2, errors in the range of $-46\,\%$ to $60\,\%$ occur if dT_1/dT of CH_2 is taken as reference value. Furthermore, the dependence of T_1 with temperature is not linear any more. Comparable effects are to be expected if a high volume fraction of CH_3 is present in the sample as methylene was shown to have a considerably higher dT_1/dT than CH_2 [36]. However, no exact examination of the resulting effects could be carried out as values for the temperature dependence of T_1 of the different components are not available for low field strengths. Future studies should further explore dT_1/dT of the fatty acid components at clinically relevant magnetic field strengths and their variability for different adipose tissue samples. In contrast to the calibration experiment presented here which is not feasible in vivo and in clinical practice, the exact knowledge of the different relaxation times of the fatty acid components may allow to determine the temperature dependence of the measured T_1 in a pre-treatment spectroscopic acquisition.
The heating experiment carried out using the derived calibration value for dT_1/dT showed small deviations between the values measured by T_1- and PRF-based thermometry and the values acquired by the temperature probe. These errors may arise from partial volume effects or spatial mismatch between the actual temperature probe position and the position of the region of interest in the MR images. Furthermore, the temperature dependence of the susceptibility of fat may bias PRF-based temperature calculation in the proximity of fatty tissue (sect. 1.2.1). Finally, small artifacts in the measured T_1 and PRF temperature graphs, and in the graphs measured with the temperature probes can be attributed to interferences due to the switching of the generator used for HIFU heating, and the interaction of the HIFU pressure waves with the temperature probe.

3.5 Simultaneous PRF thermometry and T_1 mapping using variable flip angles to monitor contrast agent release from thermosensitive liposomes

3.5.1 Clinical interest

Current clinical practice for the treatment of malign tumors relies largely on chemotherapy using cytotoxic agents, such as doxorubicin, which target fast-dividing cells, e.g. tumor cells. However, the therapeutic window for this treatment is limited by the undesired drug uptake in vital organs, and the degradation and inactivation of the drug after administration. For this reason, there is growing interest in the development of targeted delivery mechanisms in order to reduce side effects and increase its efficiency by increasing the fraction of drug delivery in the pathological area. Encapsulating the drug into dedicated nanocarriers is a promising approach which reduces the acute toxicity of the administered drug [37, 38]. Especially, thermosensitive liposomes (Fig. 3.15) which enable the heating-induced release of the encapsulated drug are of special interest [39, 40]. In order to verify the release process, co-encapsulated contrast agents like Gadolinium can be used to monitor the release with T_1-weighted MR images or T_1-mapping. The simultaneous acquisition of temperature maps allows furthermore to monitor and control the temperature required for the release [18].

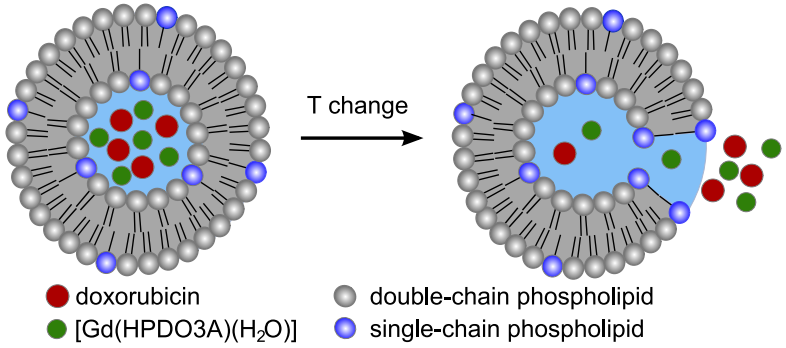

Figure 3.15: Structure and release mechanism of thermosensitive liposomes encapsulating doxorubicin and Gd-HPDO3A. The liposome membrane is formed by a phospholipid bi-layer. Incorporated cholesterol molecules enable the release at a certain transition temperature T_m.

3.5.2 T_1 relaxation of traditional thermo-sensitive liposomes encapsulating Gd-HPDO3A

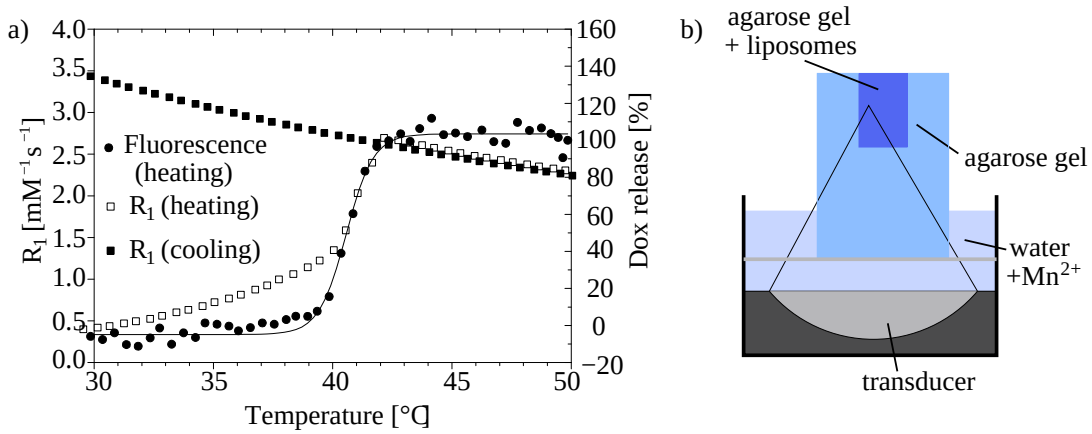

Figure 3.16: a) Relaxivity R_1 during heating and cooling together with the release percentage of co-encapsulated doxorubicin for traditional thermosensitive liposomes encapsulating Gd-HPDO3A. The graph has been adapted from [41]. b) Experimental setup for HIFU-induced contrast agent release from thermo-sensitive liposomes: The agarose phantom, with an agarose gel inset containing thermo-sensitive liposomes, is placed on the single element HIFU transducer in order to create a hot spot within the small agarose gel.

The observable T_1 relaxation time of Gd-HPDO3A encapsulated inside the thermosensitive liposomes is increased as compared to the longitudinal relaxation time of free Gd-HPDO3A as a result of the reduced water exchange with the bulk water outside the liposomes due to the phospholipid bi-layer. As the water permeability of the liposome membrane increases with temperature, a reduced T_1 relaxation time of the liposomes

can already be measured at temperatures below the characteristic phase transition temperature T_m. This behavior is reversible as long as no phase transition of the liposome membrane has occurred (Fig. 3.16a). A more detailed explanation of the release mechanism and the characteristics of the thermo-sensitive liposomes is beyond the scope of this work and can be found elsewhere [39, 40].

3.5.3 Monitoring of HIFU-induced release of contrast agents from thermosensitive liposomes

A cylindrical agarose phantom was manufactured (diameter = 3 cm, height = 3.5 cm, 2 % agarose, 2 % silica). It contained a smaller area of cylindrical agarose gel (diameter = 1 cm, $\approx$ 600 μl, 0.3 % agarose, 2 % silica), in which traditional thermo-sensitive liposomes (50 μl, 250 mM intraliposomal [Gd(HPDO3A)(H_20)] (©ProHance), phase transition temperature $T_m = 40.9\,^{\circ}$C) [40] were introduced (Fig. 3.16b). In order to avoid the thermal release of the contrast agent from the liposomes, the liposomes were added to the gel, once the temperature was sufficiently below T_m. The phantom was placed on the single element ultrasound transducer described above, and HIFU heating was performed by applying 15 W electrical power during 3 min. Simultaneous PRF thermometry and T_1 mapping was performed using the same imaging protocol as described in sect. 3.4.5. The reference temperature of the gel before heating was measured using a fluoroptic temperature probe (LumaSense Technologies, Santa Clara, CA, USA).

Figure 3.17 shows the temperature and T_1 data obtained during the HIFU-induced heating of the thermo-sensitive liposomes. On the right hand side, three magnitude images of the agarose phantom are shown. In the first image, a temperature color map calculated at the hottest time frame using PRF thermometry is superposed on the magnitude image while in the second image the change of T_1 (ΔT_1) with respect to the start of the experiment is visualized by a color overlay. The hot spot is visible in the upper left corner of the gel inset. According to the thermal properties of the used thermo-sensitive liposomes, a noticeable T_1 change is to be expected in the areas exposed to temperatures above 38 °C [40], where release of Gd-HPDO3A sets in, corresponding to a red coloring in the temperature map. Within the gel inlay containing the liposomes (dashed dotted black circle), there is a good correspondence in position and size between the area exceeding the given temperature threshold and the area with a change of T_1 above 50 ms. In the outer gel, however, no noticeably T_1 occurred even though temperatures above 38 °C were achieved. An evaluation of the temporal profiles of the temperature and T_1 is shown on the left hand side of Fig. 3.17. Each graph illustrates the temporal changes of the temperature and T_1 for two different spatial locations, p1 and p2, in the inner agarose gel of the phantom. The first point is located in the center of the hot spot, while the second one is situated outside the directly heated area. In addition, the temperature of 38 °C, where a noticeable change of T_1 is to be expected, is indicated by a dashed line. The temperature measured in the first point exceeds the threshold temperature after 2 min of HIFU heating coinciding well with a drop of T_1 of 50 ms within the following 60 s, which does not recover during the cooling period. Note that a smaller decrease of T_1 of about 30 ms can already be observed above temperatures of

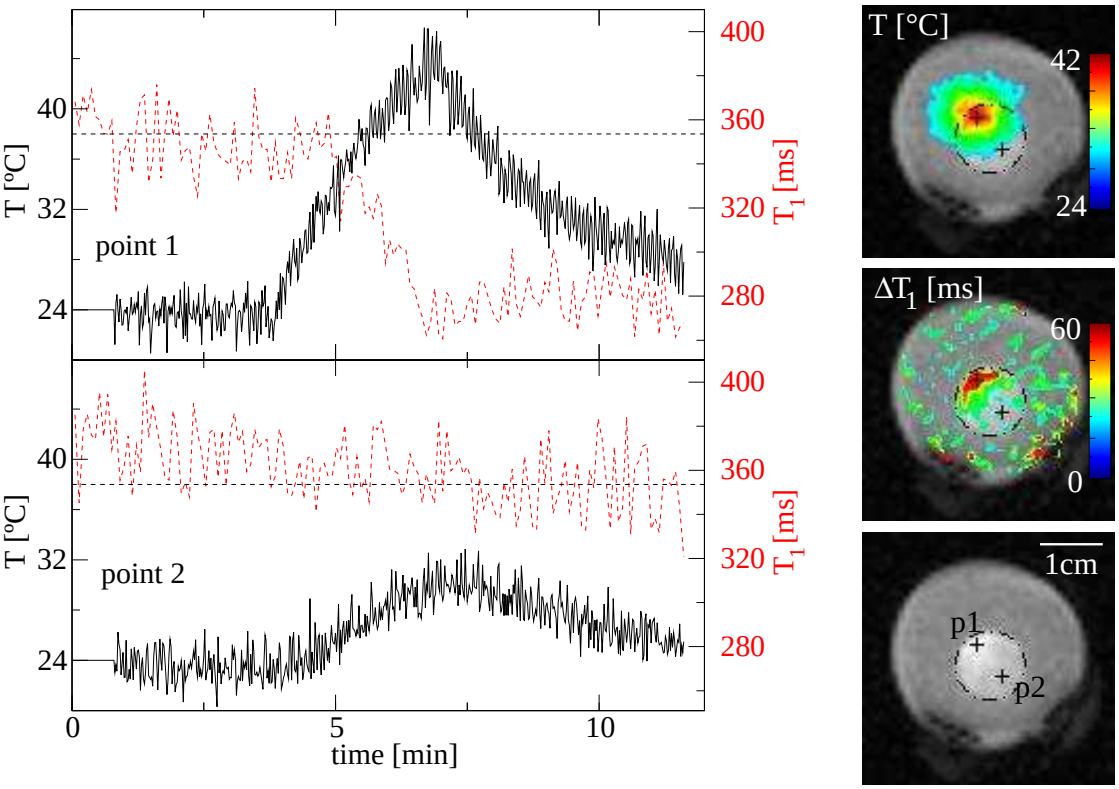

Figure 3.17: Left: Graph of the temperature measured with PRF thermometry (black solid line, scale on the left) and the measured T_1 values (red dashed line, scale on the right) for different spatial locations, p1 and p2, as indicated as black crosses in the images on the right hand side. The black dashed line represents the temperature above which Gd-HPDO3A release from the thermo-sensitive liposomes sets in. Right: PRF temperature map (top) and a map of the T_1 change (center) taken at the hottest time frame. The gel inlay is indicated by a dashed dotted black circle.

36 °C before the threshold temperature for the contrast agent release is achieved. For comparison, the T_1 measured in the central point outside the directly heated area does not show sudden changes but a slow decrease of approximately 20 ms in the course of the experiment (12 min). Furthermore, the measured temperature remains below the threshold temperature with peak values of 31 °C. The precision of the PRF temperature and T_1 measurements for this experiment were found to be 0.9 °C and 13 ms respectively.

3.5.4 Discussion

The application of simultaneous PRF thermometry and T_1 mapping during the HIFU-induced release of a contrast agent from thermo-sensitive liposomes enabled precise temperature monitoring during the heating as well as the simultaneous detection of the T_1 change as a result of the contrast agent release. Furthermore, the employed high spatial

resolution allowed a precise localization of the area which is heated above the necessary threshold temperature for Gd-HPDO3A release. This area corresponded well to the observed T_1 changes. Below the threshold temperature for the Gd-HPDO3A release, a smaller decrease of T_1 with time can be observed as expected due to the increased permeability of the liposome membrane with temperature. The chosen gel inlay which contained the thermo-sensitive liposomes may also affect the release temperature due to changes in the osmotic pressure or interactions with the liposomal membrane, leading to slightly different release behavior compared to results described in literature. Moreover, for the observed time scale, Gd-HPDO3A diffusion was negligible as the clear delineation between the gel containing liposomes and the outer gel containing no liposomes remains intact even after release of Gd-HPDO3A. Finally, the comparison of the temporal temperature and T_1 changes indicated a good correspondence between the time point when the threshold temperature was achieved, and the drop in T_1 due to the contrast agent release within the precision limits of the temperature and T_1 measurements.

4 MR thermometry of the human heart at 3T [42]

4.1 Clinical context

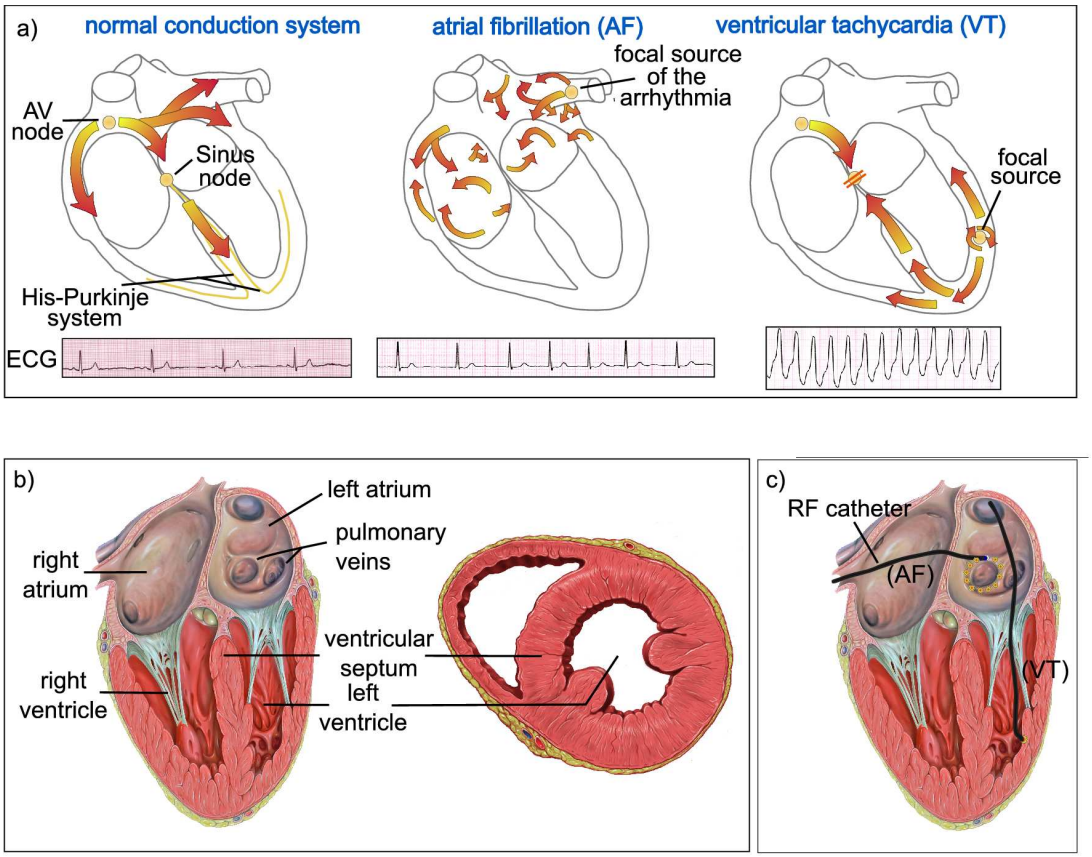

Figure 4.1: a) Conduction system of the heart and corresponding ECG pattern for the normal case, atrial fibrillation (AF), and ventricular tachycardia (VT) (from left to right). The depolarization waves are indicated by orange flashes. b) Heart anatomy in a four chamber and short axis view. c) RF catheter ablation procedure for atrial fibrillation and ventricular tachycardia.

The efficient treatment of cardiac arrhythmias is an important issue in cardiovascular medicine. Atrial fibrillation being the most prevalent form of arrhythmia, affects 1 % of the general population and up to 17 % for people older than 84 years [43]. Cardiac arrhythmias comprise all disturbances or abnormalities in the normal activation sequence of the heart. Figures 4.1a and b give an overview of the conduction system of the heart

and the heart anatomy. In the case of a healthy heart (first image in Fig. 4.1) the sinus node is the origin of a depolarization wave which propagates over the atrium, and in the process depolarizes the atrioventricular (AV) node. This leads in turn to the systematic contraction of the ventricles via the His-Purkinje system. There is a variety of possible perturbations of this process and this introduction will concentrate on two prevalent cases, atrial fibrillation and ventricular tachycardia.
The modified electrical pathways in the case of atrial fibrillation are displayed in the central image of Fig. 4.1a. In this case, the atria are contracting in a disorganized fashion, leading to a substantial reduction of the blood transport efficiency of the heart. The possible cause of atrial fibrillation can be found in the separate or combined occurrence of two effects. First, an additional focal source somewhere in the atrium causes depolarization at very high frequencies leading to a disturbance of the normal electric pathway. Second, there are several circular excitable pathways which lead to a random propagation of the depolarization wave in the atrium.
Ventricular tachycardia on the other hand, affects the ventricles as shown in the third image of Fig. 4.1a. Here, the cause of the disturbance is in general a new electric pathway, possibly due to scar tissue from a recent stroke, which causes asynchronous contractions of the ventricles. Both forms of arrhythmia can lead to symptoms like dizziness, fluttering and shortness of breath, as well as in the worst case to sudden cardiac death. The common treatment of arrhythmias is based on the administration of anti-arrhythmic drugs [44, 45]. However, RF catheter ablation has been used increasingly over the last decade and was shown to achieve comparable or superior results in the treatment of atrial fibrillation and ventricular tachycardia [46, 47]. Figure 4.1b visualizes the RF ablation procedure for atrial fibrillation and ventricular tachycardia. The ablation procedure aims to induce necrosis in the respective tissue in order to disconnect the faulty electric pathways and as a result restore the original functionalities.
The established clinical method for ablation catheter guidance is X-ray fluoroscopy [48]. In addition, echo-cardiography [49], computed tomography [50], and MR imaging [51] can be used separately or in combination [52, 53] to monitor the procedure. MR thermometry may help with the determination of the cut-off point for the energy delivery and improve safety by avoiding damage to adjacent vital structures such as the esophagus or by preventing intratissular explosions and the associated risk of tamponades [54]. Also, information about the transmurality of the myocardial ablation may increase the success rate of the first ablation procedure.

4.2 Experimental considerations

MR thermometry of the heart is challenging due to the combined respiratory and cardiac motion. VCG-triggering (triggering based on a vector cardiogram) and pencil-beam navigator-based slice tracking techniques can reduce heart and respiratory motion artifacts, but additional image processing for the correct calculation of the temperature change at each pixel is required if residual in-plane motion is present [55, 56]. With an average thickness of the myocardial wall of 8 to 15 mm and the limited spatial resolution

of MRI sequences, the contribution of blood signal resulting from partial volume effects at the interface between the cavity and the myocardium may affect MR thermometry. Blood suppression techniques could reduce this effect. The resulting increased contrast between the cavity and the myocardium may also be beneficial for the robustness of motion estimation algorithms based on the analysis of local intensity changes.
In general, MR cardiac imaging at 3 T is challenging, but when compared to lower field strengths, the echo time can be shortened to encode the identical temperature information in the phase signal for PRF MR thermometry. As a result, an increased SNR and potentially shorter acquisition times can be achieved.
In the following chapter, the feasibility of 3 T PRF MR thermometry in the myocardial wall is evaluated using accelerated gradient-echo sequences adapted to cardiac imaging and sophisticated motion compensation and phase correction algorithms. Two options for PRF MR cardiac thermometry sequences will be explored: gradient-echo with parallel imaging with and without EPI readout acceleration. Furthermore, three different blood suppression techniques are tested: multi-slice double inversion recovery (MDIR), motion-sensitized driven equilibrium (MSDE), and inflow saturation (IS). An assessment of the applied sequences and the blood suppression techniques is performed on MR images from eight healthy volunteers in the absence of heating, using the temporal stability of PRF MR thermometry [57], contrast-to-noise (CNR) and signal-to-noise (SNR) -ratios.

4.3 Blood suppression techniques

Several options are available for cardiac blood suppression, but their applicability in combination with MR thermometry sequences remains to be evaluated.

Bipolar flow spoiler gradients A simple method to cancel the signal from moving spins is to apply strong bipolar spoiler gradients after the excitation and before the signal readout in order to dephase the signal from moving spins (Fig. 4.2a). Theoretically, all static spins within the field of view would not be affected by these gradients as the accumulated phases during the application of the bipolar gradients cancel out. If, however, the affected spin is moving with velocity v_{spin}, it will experience different local magnetic fields as a result of the applied gradients and will have accumulated a non-zero phase after the spoiler gradient has been applied

$$\phi = -\gamma \left(G_M + G_P + G_S\right) v_{\text{spin}} \tau^2 \quad . \tag{4.1}$$

According to the Fourier shift theorem [58], this additional phase will lead to an apparent shift of the signal of the respective spin in k-space along the phase encoding direction

$$\Delta k_y = \phi / 2\pi y \quad , \tag{4.2}$$

where k_y denotes the k-space coordinate in the phase encoding direction and y the corresponding spatial position. For sufficiently high spoiler gradient amplitudes and

durations, $k_y > k_{y,\max}$ where $k_{y,\max}$ is the size of k-space in the phase encoding direction. As a result, the moving spins will not contribute to the signal of the image. In cardiac imaging, however, spins in the myocardium do not remain static due to the contraction of the heart. Depending on the velocity of these contractions, the signal of the myocardial spins is either displaced or completely canceled out. Moreover, the additional spoiler gradients severely prolong the echo time and hence the acquisition time. Due to the resulting poor image quality, this blood suppression technique was not further considered for the following experiments.

Multi-slice double inversion recovery (MDIR) A well established method is the double inversion recovery (DIR) technique which was proven to reliably suppress the signal of blood, independent of the blood flow rate [59]. This technique exploits the difference of the longitudinal relaxation times of blood and myocardium (at 3 T: $T_{1,\text{blood}} = 1550\,\text{ms}$, $T_{1,\text{myocard}} = 1115\,\text{ms}$ [60]) as shown in Fig. 4.3. First, a non-selective 180 ° excitation pulse inverts the magnetization of all spins in the imaging volume. This pulse is immediately followed by a slice selective inversion pulse which restores the magnetization of the spins in the selected slice. During the following inversion delay T_{I2} the blood spins in the selected slice are replaced by inflowing spins which have not encountered the second inversion pulse. As a result, if

$$T_{I2} = T_{1,\text{blood}} \ln\left(\frac{2}{1+\exp\left(-T_{R,\text{DIR}}/T_{1,\text{blood}}\right)}\right) \tag{4.3}$$

is chosen [61], the longitudinal magnetization of the blood is zero when the excitation pulse with flip angle α is applied to create detectable transverse magnetization. $T_{R,\text{DIR}}$ is the time between two successive DIR modules (here typically 1 s). Even though, the blood signal can be suppressed very effectively with this technique, it has several

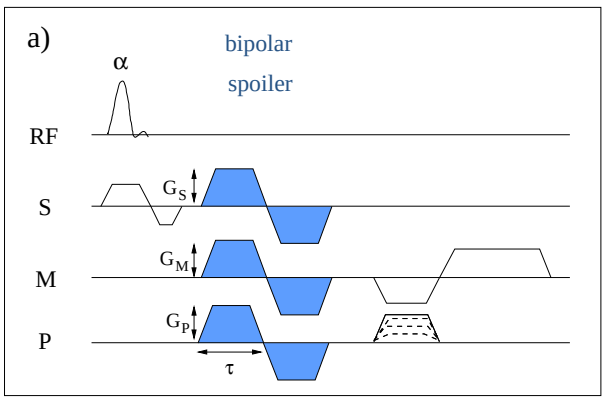

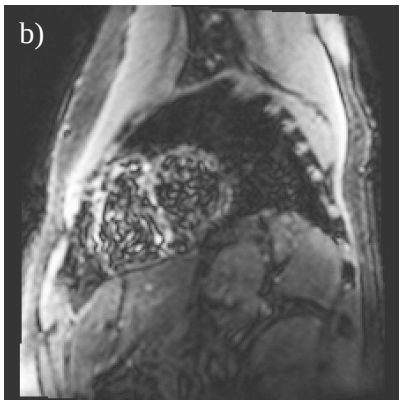

Figure 4.2: a) Diagram of a gradient echo sequence with bipolar spoiler gradients before the readout in all three encoding directions. b) Example of a short axis image of the heart acquired with a TFE sequence and a bipolar flow spoiler along the slice select direction.

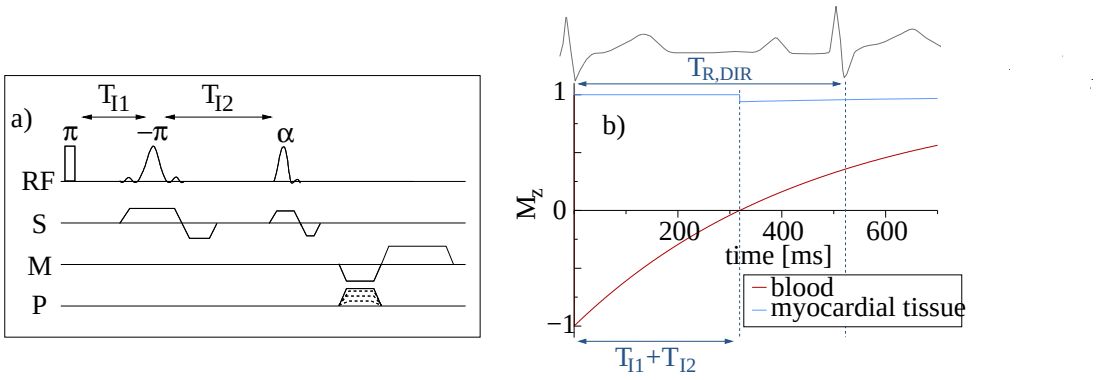

Figure 4.3: a): Diagram of a gradient echo sequence with double inversion recovery (DIR) preparation. Shown are the non-selective inversion pulse, the selective adiabatic inversion pulse and after inversion time $T_{I2} + T_{I2}$ the actual gradient echo sequence. b) Magnetization of the blood spins and the spins in the myocardium during the application of the DIR preparation. The magnetization is initially inverted by a non-selective excitation pulse which is followed by a slice-selective inversion pulse which reinverts the magnetization in the imaging slice. During the inversion delay T_{I2}, the blood spins in the imaging slice are replaced by inflowing spins which have not encountered the reinversion pulse. T_{I2} is chosen such that the magnetization of the blood spins is zero at the moment of the image acquisition. After $T_{R,\mathrm{DIR}}$ (here equal to the length of one cardiac cycle), the next dynamic scan with DIR preparation is started.

disadvantages. The necessary inversion delay (at 3 T: $T_{I2} = 300 - 450$ ms) severely prolongs the actual acquisition time. What is more, optimal blood suppression can only be achieved for the slice which is acquired at T_{I2} fulfilling the condition of zero blood magnetization. Other slices will show contributions from the slightly recovered blood magnetization. Nevertheless, multi-slice implementations have been presented recently [62, 63]. For this work, a standard DIR preparation module was adapted to multi-slice imaging (MDIR). As a compromise between volume coverage (3 slices) within the given cardiac cycle and blood suppression efficiency, inversion times (T_{I1}/T_{I2}) of (4 ms/320 ms) were used.

Inflow saturation (IS) Alternatively, saturation slabs positioned parallel to the image stack can be used to suppress the signal of inflowing spins (Fig. 4.4), a technique known as inflow saturation. Here, the efficacy of blood suppression in each slice depends on the distance of the saturation slabs from the slice and the blood velocity. IS is adapted to VCG-triggered multi-slice cardiac imaging, and was shown to provide efficient suppression of inflowing spins [64]. In this work, inflow saturation was accomplished by placing one saturation slab of 60 to 80 mm thickness between the image stack and the base of the heart at a distance of 5 to 15 mm leading to a maximal increase in acquisition time of 6 ms.

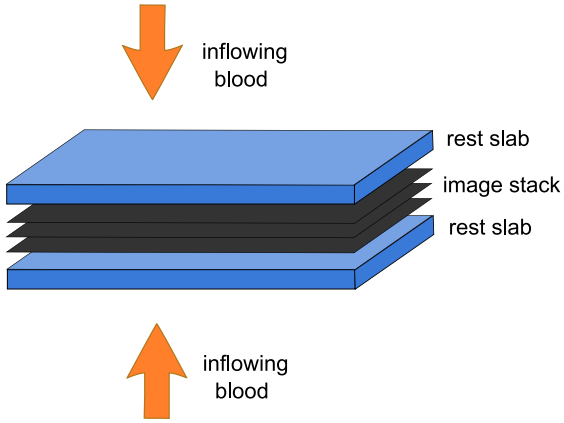

Figure 4.4: Positioning of the saturation slabs (rest slabs) around the image stack. Both saturation slabs will cancel the signal of inflowing spins.

Motion sensitized driven equilibrium (MSDE) A more recent technique using MSDE [65] magnetization preparation, was evaluated [66] and successfully used for black blood carotid imaging [67]. This approach only adds a minimal delay before the acquisition and is compatible with VCG-triggered cardiac multi-slice imaging. There is only a slight increase in scan time, but the preparatory module introduces T_2 weighting, which leads to additional signal loss. Moreover, MSDE may be sensitive to inhomogeneities of the RF excitation (B_1) field, leading to a spatially varying actual flip angle and eddy current effects, especially at high magnetic fields. The implemented blood suppression MSDE preparatory module is detailed in Fig. 4.5a and represents an improved version of the module proposed in [68]. In order to achieve a higher robustness against B_1 inhomogeneities, two composite inversion pulses were used. Adiabatic pulses were tested.

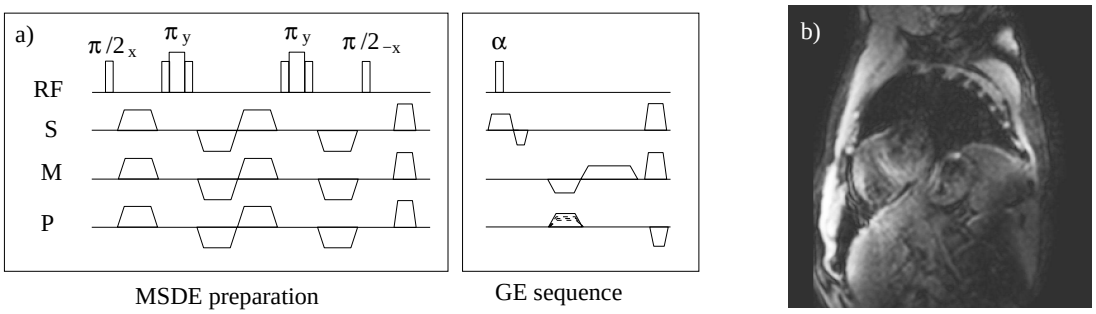

Figure 4.5: a) Illustration of a gradient echo (GE) sequence using the MSDE blood suppression preparation. b) Example of a short axis TFE image of the heart using the MSDE preparation with $v_{\mathrm{enc}} = 20\,\mathrm{cm/s}$ in all three encoding directions. The signal of the lateral part of the myocardium has been severely reduced as a result of the blood suppression.

However, the resulting images showed motion artifacts as a result of the significantly increased duration of the preparation module and thus non-adiabatic pulses were chosen. Furthermore, bipolar gradients were used in order to compensate for eddy current effects. The strength of the applied motion sensitizing gradients was characterized using the definition proposed by Nguyen et al. [66] $v_{\mathrm{enc}} = \pi\gamma/m_1$ where γ is the gyromagnetic ratio and m_1 is defined as the first moment of the applied gradient. In this definition v_{enc} corresponds to the velocity of the blood spins which are dephased by π. This blood suppression technique is therefore velocity selective and an adaptation of v_{enc} is required for each volunteer in order to match the blood velocity. The value of v_{enc} was adjusted on each volunteer between $20\,\mathrm{cm\,s^{-1}}$ and $40\,\mathrm{cm\,s^{-1}}$ (corresponding to m_1 of $16\,\mathrm{mT\,m^{-1}\,ms}$ to $8\,\mathrm{mT\,m^{-1}ms}$). It was adapted by varying the gradient strength while the length of the preparation module remained fixed at 9 ms. No separate adjustment of v_{enc} for the three different encoding directions was performed as such an approach was considered too time-consuming. Finally, as the myocardium does not remain completely static during the acquisition, the signal of the myocardial spins may be suppressed as well provided that their velocity is comparable to the blood spins to be suppressed. An example of such a case is displayed in Fig. 4.5b.

4.4 Design of the imaging protocol

4.4.1 Choice of sequence and sequence parameters

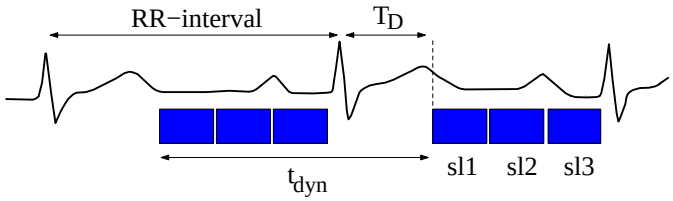

Figure 4.6: Positioning of the image acquisition within the cardiac cycle (RR-interval) for a pre-defined trigger delay (T_D) and 3 slices leading to a dynamic scan time t_{dyn}.

The work presented in this chapter was performed on a 3 T MR system (Achieva, Philips, Best, The Netherlands) using a 6-channel surface cardiac coil. Emphasis was put on gradient-echo based sequences, even though rapid cine cardiac imaging typically relies on the use of rapid steady state free precession sequences (SSFP) [69, 70]. However, SSFP-based MR thermometry [71] remains time-consuming and is susceptible to motion artifacts limiting its applicability for monitoring cardiac RF ablations. Moreover, SSFP-based sequences are prone to off-resonance artifacts and require a high energy deposition, which can induce undesirable heating of the catheter wires [72] particularly in the case of continuous image acquisition over several minutes.

For real-time PRF-based MR thermometry in the myocardium the final imaging protocol had to be be optimized in order to fulfill certain requirements:

- sufficient volume coverage with spatial resolution in the millimeter range to visualize the temperature distribution in the myocardium
- $T_E \sim T_2^*$ (at 3 T: T_2^*(myocardium) $\sim 15 - 20$ ms [60]) for optimal temperature precision using PRF thermometry [73]
- a SNR of at least 10 to guarantee sufficient phase precision
- short acquisition times per slice (< 300 ms) in order to avoid intra-scan motion

Furthermore, respiratory through-plane motion had to be compensated with a slice-tracking technique that used a pencil-beam navigator placed on the right diaphragm to adjust the image slice position in real-time. All acquisitions were VCG-triggered, with a trigger delay (T_D) set to the longest available value (between 109 ms and 699 ms depending on the used blood suppression technique and the cardiac frequency of the volunteer (50 to 85 beats/min)). Even though fat suppression is necessary for PRF thermometry in organs like liver, this is not the case in the myocardium, as the fat content and chemical shift effects are negligible. However, the signal from subcutaneous fat in the field of view resulted in considerable artifacts in the center of the field of view due to the parallel imaging reconstruction (SENSitiviy Encoding (SENSE) [74]) reconstruction. Consequently, for effective fat suppression in the presence of B_1 inhomogeneities, spectrally-selective adiabatic inversion recovery (SPAIR, inversion time 90 ms) was applied before each slice acquisition. As the gradient-echo steady state is disturbed by the necessary VCG triggering and the fat suppression pulses, a transient field echo sequence (TFE) was used for all experiments. The implemented flip angle ramp accelerates the approach to steady state. A RF-spoiled TFE sequence ($T_R = 7.3$ ms, $T_E = 4.6$ ms, flip angle = $26 - 30\,^\circ$, bandwidth/pixel = 291 Hz, FOV = $350 \times 280 \times 8\,\text{mm}^3$, matrix = 100×80) with parallel imaging acceleration (SENSE) of 4 was tested.
Higher SENSE acceleration factors were not possible due to the limited number of coil elements and signal considerations. In order to further accelerate the acquisition while maintaining a reasonable echo time for MR thermometry phase accumulation, a RF-spoiled TFE-EPI (transient field echo sequence with EPI readout) sequence ($T_R = 11$ ms, $T_E = 6$ ms, flip angle = $26 - 30\,^\circ$, bandwidth/pixel = 217 Hz, FOV = $350 \times 350 \times 8\,\text{mm}^3$, matrix = 100×100) with an echo train length of 3 and a SENSE factor of 3 was chosen in a second experiment. Echo train lengths of 5 or more were tested, but, despite the use of a localized main magnetic field (B_0) shim on the heart, they led to significant image quality degradation on the heart and were not further used.
A PRESTO (principles of echo-shifting with a train of observations) sequence [75] was tested as it would provide a long echo time even for comparably short repetition times. The sequence was found to be very sensitive to intra-scan motion and was, as a result, found to be not suitable for the given application.
With acquisition times of ~ 150 ms and ~ 220 ms for TFE-EPI and TFE respectively, a minimum of 3 slices per cardiac cycle could be acquired without reducing the spatial

resolution. In total, 100 consecutive short axis (mid position) images were acquired dynamically (dynamic scan time $t_{\mathrm{dyn}} = 0.75 - 1.2\,\mathrm{s}$) covering 3 slices per cardiac cycle. The timing of the described sequence within the cardiac cycle is depicted in Fig. 4.6.

4.5 Image processing

4.5.1 Motion compensation

In-plane motion compensation was performed by analyzing local displacements on the magnitude images. For this purpose, the first image in the time series was selected as the reference image, on which a region of interest (ROI) delimiting the left myocardium was manually drawn. A gradient driven descent algorithm maximizing the inter-correlation coefficient between this reference image and each following magnitude image of the time series was performed, assuming an affine displacement restricted to the selected ROI [55]. The 6 coefficients of the affine transformation (two translations, two scales, a rotation, a shear) leading to the highest correlation with the reference image were stored for each image of the time series. Images containing artifacts due to erroneous navigator slice tracking were identified by calculating the Pearson inter-correlation coefficient $C_{0,n}$ [76] between each image and the first image of the time series. A rejection criterion was introduced such that images with $C_{0,n} < 0.7$ were removed for further evaluation.

4.5.2 Evaluation of the image quality

In order to evaluate the efficiency of the different blood suppression techniques, SNR and CNR were evaluated from the motion compensated images. The inhomogeneous noise distribution in the images as a result of the applied parallel imaging technique required a modified definition for both expressions [67]

$$\begin{aligned} \mathrm{SNR} &= \frac{\bar{S}_{\mathrm{sep}}}{\sigma_{\mathrm{sep}}} \\ \mathrm{CNR} &= \frac{\bar{S}_{\mathrm{sep}} - \bar{S}_{\mathrm{cav}}}{0.5\,(\sigma_{\mathrm{sep}} + \sigma_{\mathrm{cav}})} \quad , \end{aligned} \tag{4.4}$$

where $\bar{S}_{\mathrm{sep}}$ denotes the average signal in a small ROI in the ventricular septum, $\bar{S}_{\mathrm{cav}}$ the average signal in a small ROI in the cavity and σ_{sep} and σ_{cav} the respective signal standard deviations in the same ROIs.. As a result, the calculated SNR allows to draw conclusions about the ratio between the measured signal and the corresponding spatial variation of the signal in the chosen ROI, but not about the image noise in general.

4.5.3 Temperature calculation

Susceptibility effects were corrected with a model-based multi-baseline approach [55]. The first 50 images were acquired in a learning phase and the coefficients calculated during the registration were used to create parametric phase maps assuming a linear

relationship between respiratory motion and susceptibility related phase changes [78]. In contrast to the first order model-based phase correction described in sect. 3.3, these synthetic phase images were computed by a Singular Value Decomposition (SVD) of the list of motion registered acquired phase images using the registration coefficients calculated before. For the following 50 images, the coefficients retrieved during the image registration were used to compute a synthetic phase image. Finally, the temperature was calculated by subtracting the synthesized reference phase from the current phase using the PRF method [79]. In order to assess the quality of the temperature measurements in the myocardium, the temporal mean μ_T (reflecting systematic offsets) and standard deviation of temperature σ_T (reflecting precision, or stability) were calculated at each pixel. Since rapid gradient echo-based sequences are prone to artifacts at susceptibility interfaces (myocardium/liver, myocardium/lung), the central region of the myocardium, corresponding to the ventricular septum, was chosen as target area for a detailed statistical analysis. The spatial distribution of σ_T, as well as the spatial average of σ_T in a ROI in the ventricular septum $\bar{\sigma}_T$, as well as the spatial distribution of μ_T and its spatial average $\bar{\mu}_T$, were analyzed. The aim of this evaluation was to find a combination of imaging sequence and blood suppression technique providing minimal σ_T (corresponding to a maximal temperature stability) as well as minimal μ_T.

4.5.4 Statistical Analysis

The significance of the results for the SNR/CNR and the temperature stabilities and temporal averages of temperature were evaluated for each volunteer separately. For this, an analysis of variances (ANOVA) in form of a F-test (sect. A.1.2) was performed on the results for all blood suppression techniques with significance threshold 0.05. If the test was significant, additional independent t-tests (sect. A.1.1) were applied to the data of all pairs of blood suppression techniques for the respective volunteer. A significance of $p = 0.05$ was used and corrected with the Bonferroni method (sect. A.1.3).

4.6 Experimental results

4.6.1 TFE sequence

Figures 4.7a-d show typical magnitude images of the middle slice obtained on the same volunteer without blood suppression and using MDIR, MSDE and IS. All three blood suppression techniques in combination with TFE showed a comparable good performance in terms of blood suppression efficiency and image quality. As a criterion for the evaluation of the blood suppression performance, the mean value over all volunteers of the temporal average of the CNR and SNR in the ventricular septum calculated according to eq. (4.4) together with the corresponding temporal standard deviation are displayed in Fig. 4.8. The application of any of the three blood suppression techniques led to an increased CNR between the septum and the cavity. For each volunteer, the achieved average CNR for every blood suppression method was compared with the other three methods. On average, MDIR showed a CNR which was approximately 30 % higher than

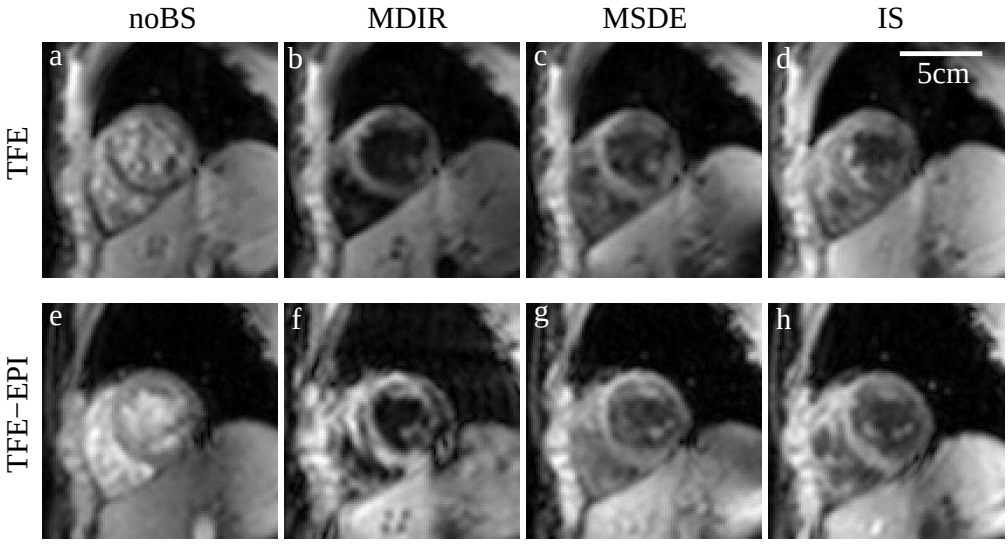

Figure 4.7: Magnified magnitude images for TFE (top row) and for TFE-EPI (bottom row) for one volunteer, central slice. From left to right: without blood suppression (noBS), MDIR, MSDE, and IS.

for MSDE or IS. Furthermore, in the acquisitions without blood suppression, for 6 of 8 volunteers the myocardium appeared hypo-intense in comparison to the signal of the blood in the cavity leading to a negative CNR (results not shown). On average, all blood suppression techniques led to an increased SNR in the ventricular septum as compared to the acquisition without blood suppression, but no significant difference between the blood suppression techniques has been observed. According to eq. (4.4), a high SNR is an indication of reduced spatial signal variation in the septum as a result of the applied blood suppression.
For the two remaining slices (results not shown), the results for SNR were similar to those in the central slice. In the last slice, the CNR was higher for all blood suppression techniques and inflow saturation produced a much lower CNR in the first slice than in slices 2 and 3.
As a second comparison criterion, the results of the evaluation of the temperature stability and the temporal mean of temperature in the myocardium are shown in the upper rows of Figures 4.9 and 4.10 as an overlay on the magnified magnitude images for the middle slice. Note that the distributions of the temperature stability and the temporal means of temperature were spatially inhomogeneous, showing a degradation at the interface with the liver and the lungs. However, at the interface between the lung and the myocardium and in the ventricular septum the temperature stability distribution and the distribution of the temporal mean of temperature remained stable. In the ventricular septum a temperature stability of 2.8 °C has been achieved with the TFE sequence. A detailed evaluation of the spatial distribution of the temperature stability in the ventricular septum is presented in Fig. 4.11 for the central slice using the combined data

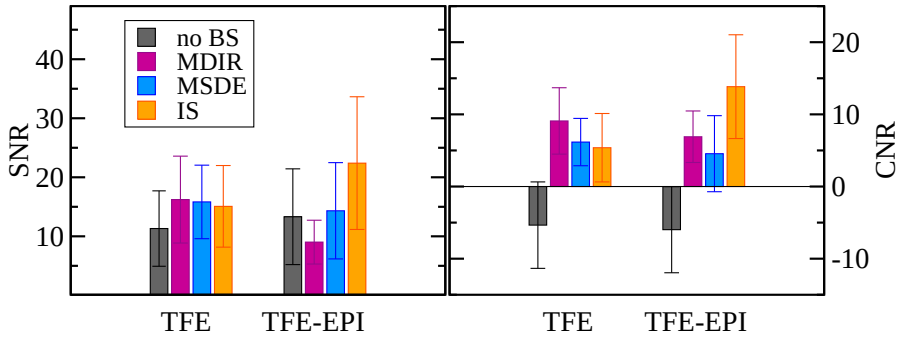

Figure 4.8: Mean values over all volunteers of the temporal average of the SNR and CNR according to eq. (4.4) (boxes) together with the corresponding standard deviations (whiskers) for the different blood suppression techniques and the two different sequences for the central slice. Negative CNR values indicate a hypo-intense myocardial signal as compared to the signal of the blood in the cavity. The size of the ROI's varied between 95 and 294 voxels with an average value of 175 voxels.

from all volunteers in form of Box-Whisker plots. In addition, the average temperature stabilities in the ventricular septum including the corresponding spatial standard deviations are shown in Table 4.1 as the mean, minimal and maximal value over all volunteers for the different blood suppression techniques. Compared to the acquisition without blood suppression the temperature stability was enhanced in 4 out of 8 cases for MDIR, in 5 out of 8 cases for IS, and in 6 out of 8 cases for MSDE ($p < 0.05$, data not shown). In the cases with a reduced temperature stability as compared to the results achieved without blood suppression, especially high deviations were found for MDIR for 2 volunteers and for MSDE and IS for 3 volunteers. No obvious correlation between the

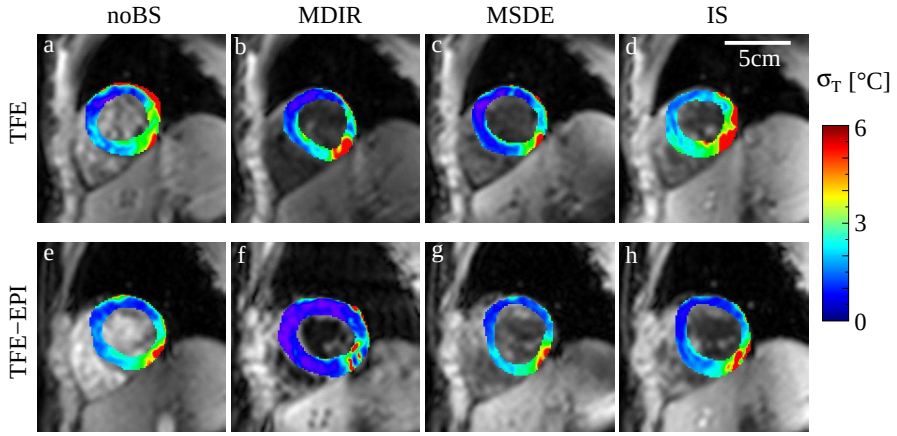

Figure 4.9: Magnified magnitude images with an overlay of the temperature stability σ_T for TFE (top row) and for TFE-EPI (bottom row) for one volunteer, central slice.

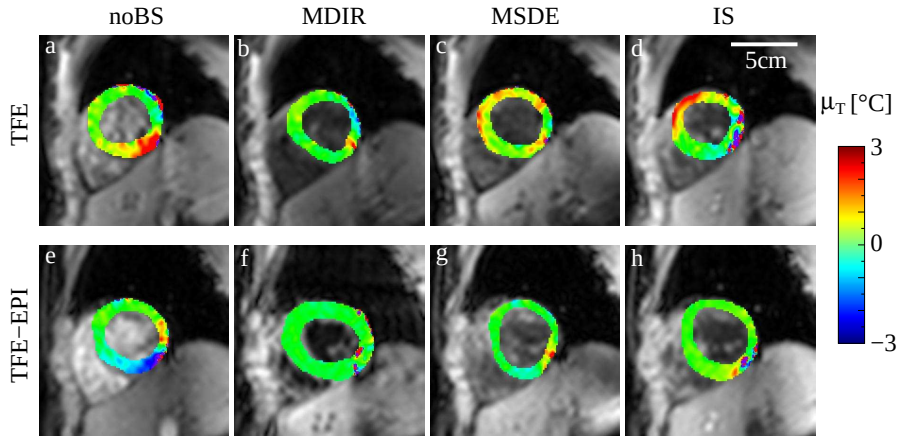

Figure 4.10: Magnified magnitude images with an overlay of the temporal average of temperature μ_T for TFE (a-d) and for TFE-EPI (e-h) for one volunteer, central slice. From left to right: without blood suppression (noBS), MDIR, MSDE and IS.

measured CNR in the ventricular septum as shown in Fig. 4.8 and the temperature stabilities were found. Finally, Table 4.1 shows the spatial average and standard deviations of the temporal mean of temperature in the ventricular septum as the mean, minimal and maximal value over all volunteers for all blood suppression methods. On average, a positive temperature offset of 0.0 °C to 0.7 °C has been measured without statistically significant difference between the blood suppression methods. This has been verified by ANOVA with significance $p = 0.05$. For the two remaining slices, the results for the temporal average of temperature and temperature stability were comparable. Only MDIR showed a decreased temperature stability in the last slice.
In general, the average blood suppression performance of the three blood suppression techniques was found comparable for this sequence type.

4.6.2 TFE-EPI sequence

Figures 4.7e-h show magnitude images of the middle slice obtained on the same volunteer without blood suppression and using the three different blood suppression techniques. The images acquired using MSDE and IS showed a comparable quality and blood suppression efficiency, whereas the image acquired with MDIR suffered from motion-induced blurring. It was found that in terms of SNR, MDIR and MSDE suffered from a reduced or comparable SNR in the ventricular septum as compared to the acquisition without blood suppression, while IS showed a higher SNR indicating that IS achieved a more favorable ratio between myocardial signal and spatial signal homogeneity than MDIR and MSDE (right hand side of Fig. 4.8). As expected, the CNR between the myocardium and the cavity was increased for all blood suppression techniques, with the IS technique performing best in comparison with MDIR and MSDE.
Furthermore, in the acquisitions without blood suppression for 6 of 8 volunteers and for

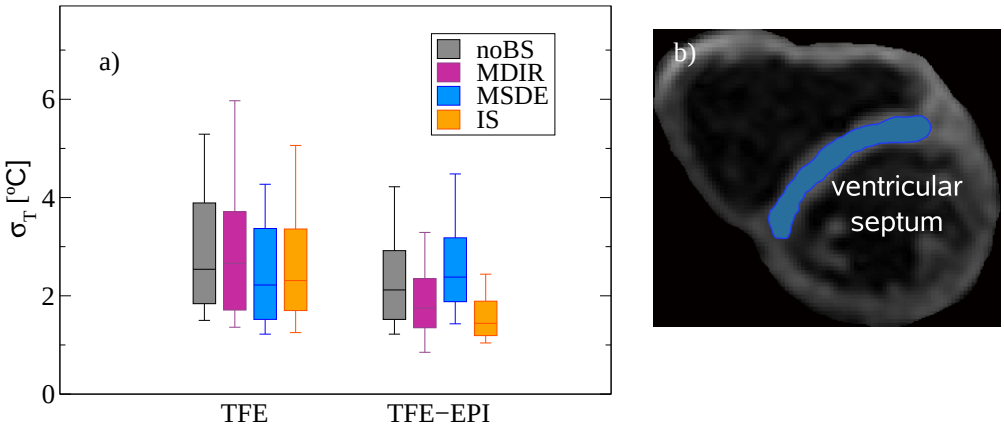

Figure 4.11: a) Box-Whisker plots of the spatial distribution of the temperature stability in the ventricular septum σ_T for the acquisitions without blood suppression (no BS), DIR, MSDE and IS for the central slice. The boxes give the range where 25 % − 75 % of the temperature stabilities are found with the median given by the central horizontal line. The whiskers indicate the temperature stabilities which are exceeded by 10 % and 90 % of the voxels in the chosen ROI. The plots have been created from the combined data of all volunteers. b) Chosen ROI in the ventricular septum. The ROIs were manually drawn for every volunteer and blood suppression technique. The size of the ROI's varied between 95 and 294 voxels with an average value of 175 voxels.

MSDE for 2 volunteers, the myocardium appeared hypo-intense in comparison to the signal of the blood in the cavity leading to a negative CNR (data not shown). For the remaining slices (results not shown) a similar behavior was found. Only IS showed a decreased CNR in the first slice. An evaluation of the different blood suppression techniques in terms of the achieved temperature stability and temporal mean of temperature in the myocardium is displayed in the bottom rows of Figures 4.9 and 4.10 as an overlay on the magnified magnitude images for the same volunteer and the central slice. Similar to the acquisitions using TFE without EPI readout, the temperature stability and temporal mean of temperature were deteriorated at the interface with the lungs and the liver, but improved in the other sections of the myocardium. Despite the apparent blurring in the magnitude images for MDIR, the measured temperature stability and temporal mean of temperature in the myocardium were not affected by these artifacts. A detailed statistical analysis of the spatial distribution of the temperature stability in the ventricular septum for the different blood suppression techniques is shown in Fig. 4.11 and Table 4.1 using the combined data from all volunteers and the central slice. Statistically significant improvements of the temperature stability in comparison to the acquisition without blood suppression have been observed in 3 of 8 cases for MSDE, in 5 of 8 cases for MDIR, and in 7 of 8 cases for IS ($p < 0.05$). Unlike the acquisitions using TFE without EPI readout, IS blood suppression performed significantly better than MDIR in 5 of 8 cases and than MSDE in 7 of 8 cases ($p < 0.05$), as confirmed in the Box-Whisker plots in Fig. 4.11, which represents the combined evaluation over the ROI's

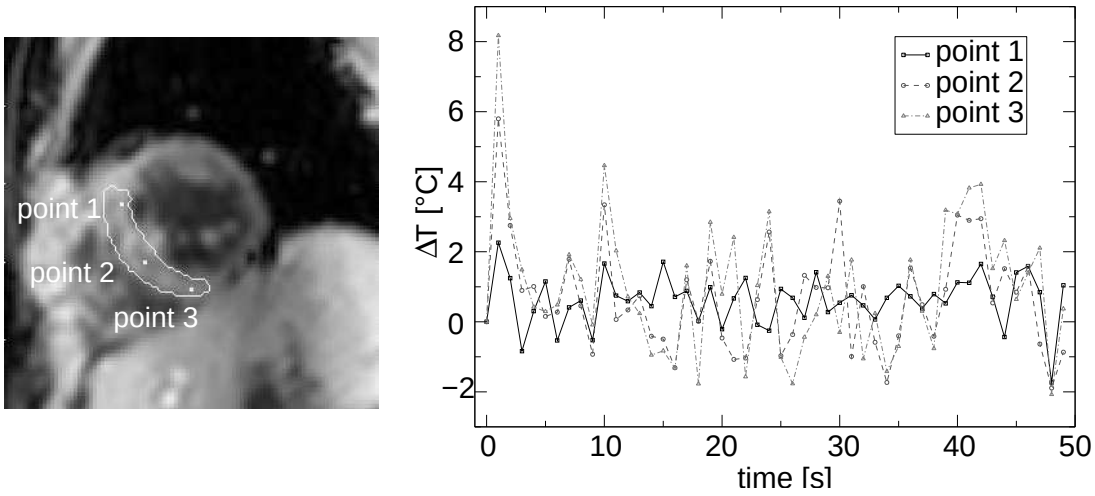

Figure 4.12: Temperature evolution for TFE-EPI with IS for one volunteer, central slice. Shown are the graphs for three different voxels at characteristic locations in the ventricular septum as shown as white points on the magnitude image on the left.

of all volunteers. Among the cases with reduced temperature stability as compared to the acquisition without blood suppression, remarkably poor temperature stabilities were observed for MDIR for 1 volunteer, and for MSDE for 3 volunteers. This manifested itself also in substantially decreased average temperature stabilities, as presented in Table 4.1, where for the mentioned cases values of up to $(16.9 \pm 22.9)\,^{\circ}\mathrm{C}$ were observed. For this sequence, there was a good correspondence between the observed CNR in the ventricular septum as displayed in Fig. 4.8 and the corresponding temperature stability. This was confirmed in the results of MSDE for 2 volunteers, where a hypo-intense signal in the septum was coupled to a significantly decreased temperature stability. A similar observation has been made for 2 volunteers in the cases where no blood suppression was applied. On the other hand a significantly increased CNR for 4 volunteers was coupled to a very high temperature stability in the ventricular septum (data not shown). Figure 4.12 shows the temperature measured at three different characteristic points in the ventricular septum for the IS technique and the central slice of one volunteer. The temperature remained stable and was shifted by approximately $0.7\,^{\circ}\mathrm{C}$, $1.5\,^{\circ}\mathrm{C}$ and $1.9\,^{\circ}\mathrm{C}$ for the three different points. Moreover, the temperature graphs confirm that the temporal standard deviation of temperature was increased for points closer to the interface with the lungs and the liver as already stated above. In addition, Table 4.1 shows the spatial average and standard deviation of the temporal mean of temperature in the ventricular septum as the mean, minimal and maximal value over all volunteers for all blood suppression techniques. In average, mean temperatures of $0.2\,^{\circ}\mathrm{C}$ to $0.4\,^{\circ}\mathrm{C}$ have been measured for the different blood suppression techniques. The last acquired slice showed similar temperature stabilities and temporal averages of temperature. For the first slice, the acquisitions with IS and MSDE produced lower temperature stabilities than for the

TFE

	noBS	MDIR	MSDE	IS
$\bar{\sigma}_T$ [°C]	3.0 ± 1.6	3.1 ± 1.8	2.5 ± 1.2	2.8 ± 1.7
$\bar{\sigma}_{T,\min}$ [°C]	1.7 ± 0.3	1.6 ± 0.6	1.4 ± 0.4	1.5 ± 0.5
$\bar{\sigma}_{T,\max}$ [°C]	4.9 ± 0.8	6.2 ± 1.8	4.1 ± 1.4	4.8 ± 2.4
$\bar{\mu}_T$ [°C]	0.4 ± 1.1	0.6 ± 0.9	0.0 ± 1.0	0.7 ± 1.0
$\bar{\mu}_{T,\min}$ [°C]	-0.5 ± 0.8	-0.4 ± 0.6	-0.8 ± 0.7	-0.3 ± 1.0
$\bar{\mu}_{T,\max}$ [°C]	1.7 ± 0.8	1.5 ± 0.5	1.3 ± 0.4	1.7 ± 0.7

TFE-EPI

	noBS	MDIR	MSDE	IS
$\bar{\sigma}_T$ [°C]	2.4 ± 1.2	2.0 ± 0.9	4.2 ± 9.2	1.6 ± 0.6
$\bar{\sigma}_{T,\min}$ [°C]	1.6 ± 0.4	1.7 ± 0.4	1.4 ± 0.3	1.2 ± 0.2
$\bar{\sigma}_{T,\max}$ [°C]	3.6 ± 1.8	3.6 ± 0.9	16.6 ± 22.7	2.3 ± 0.9
$\bar{\mu}_T$ [°C]	0.2 ± 0.9	0.3 ± 1.0	0.5 ± 13.5	0.4 ± 0.7
$\bar{\mu}_{T,\min}$ [°C]	-0.5 ± 0.7	-1.2 ± 0.5	-1.0 ± 0.6	-0.7 ± 0.4
$\bar{\mu}_{T,\max}$ [°C]	1.0 ± 0.8	1.5 ± 0.6	1.2 ± 0.7	1.1 ± 0.3

Table 4.1: Spatial average of the temperature stability $\bar{\sigma}_T$ and the temporal average of temperature $\bar{\mu}_T$ in the ventricular septum including the spatial standard deviations for blood suppression techniques and the two tested sequences. Shown are the average values for all volunteers, as well as the minimal and maximal values found in the group of volunteers. This data is taken from the central slice. The size of the ROI's varied between 95 and 294 voxels with an average value of 175 voxels.

second and third slice.

4.7 Discussion

4.7.1 Imaging protocol

A direct comparison of the two applied sequences (TFE and TFE-EPI) is not straightforward as several factors have to be taken into account. The TFE sequence is robust against motion artifacts and B_0 inhomogeneities while suffering from longer acquisition times. As a result, the achievable echo times are limited, leading to a reduced temperature precision. Combining this sequence with an EPI readout leads to a significant acceleration, with reduced intra-scan motion, but the EPI readout is intrinsically more sensitive to susceptibility artifacts. For the presented cases the TFE-EPI sequence achieved on average better temperature stabilities in the ventricular septum. In addition, it enabled higher volume coverage and longer echo times due to the intrinsically shorter acquisition times.

The applied imaging protocol for MR thermometry required a compromise between spatial resolution, volume coverage, overall scan time and signal. In this study, a spatial resolution of $3.5 \times 3.5 \times 8\,\mathrm{mm}^3$ covering 3 slices was chosen in order to allow a temporal resolution of one heart beat, yielding an average SNR of 15. Considering the size of a catheter tip and the expected hot spot during a RF ablation procedure, a higher spatial resolution would be desirable. As the SNR directly influences the theoretically achievable temperature precision [57], a further reduction of the voxel size would result in a decreased temperature precision, if the associated signal loss is not compensated by other means. A potentially higher signal could, for example, be achieved by using available 32-channel cardiac coils. Increasing the SENSE acceleration factor could be beneficial, but again, the resulting signal loss would have to be compensated in order to maintain the current temperature precision. Furthermore, longer echo times, corresponding to potentially higher temperature precisions and increased volume coverage, could be achieved by selecting smaller FOVs. However, established inner volume excitation techniques [80, 81] are usually based on inversion techniques which are not compatible with gradient echo imaging for MR thermometry. Other approaches using tailored RF pulses have been successfully tested, for example in 3D carotid imaging [82], but have not yet been applied to MR temperature imaging. The use of saturation slabs for the FOV reduction is possible with gradient echo sequences, but leads to an increased acquisition time.

4.7.2 Blood suppression techniques

IS In terms of blood suppression, inflow saturation appears to be the most robust method yielding a spatial average temperature stability in the ventricular septum of 2 °C or better when combined with the TFE-EPI acquisition. Nevertheless, the application of inflow saturation slabs remains time-consuming and care must be taken when positioning the pencil-beam to avoid saturation of the spins by the IS slabs. Furthermore, as IS is based on the inflow effect, blood suppression efficacy in every slice depends on the distance of the saturation slab from the image stack, the exact blood velocity, and the slice order. In our setup, blood suppression was always more effective in the last acquired slice.

MDIR Multi-slice DIR achieves good blood suppression over all slices, leading to an average temperature stability of 3 °C when used with a TFE sequence. However, it suffers from long scan times as a result of the necessary inversion delay limiting the slice number to 2 to 3 for typical cardiac frequencies (ranging from 0.8 Hz to 1.2 Hz for the presented volunteers). Furthermore, in our implementation, the combination with EPI readout led to severe image artifacts. This may be due to the fact that the EPI phase correction data was acquired prior to the inversion delay. It is acquired once at the beginning of a dynamic series of images by switching off the phase encoding gradients. However, if motion occurs between the acquisition of the phase correction data and the acquisition of the actual image, the resulting images will contain artifacts due to residual phase offsets between the acquired k-space lines. A catheter tip in contact with

the myocardium is likely to cause additional susceptibility artifacts, and hence lead to a further deterioration of the image quality. If these problems are resolved, multi-slice DIR could become a candidate for blood suppression during MR thermometry using TFE sequences with or without EPI acceleration.

MSDE The application of MSDE for blood suppression resulted in an average temperature stability of 3 °C or better. However, due to its sensitivity to B_0 and B_1 inhomogeneities, large variations in the blood suppression performance were observed. This is also because for a chosen gradient strength, only one particular blood velocity is completely suppressed. As this technique also reduces the signal from all bulk motion, in some cases, the signal of the myocardium was reduced as well, leading to a degraded CNR between myocardium and cavity. General signal loss in the myocardium may be overcome by applying B_1 shimming [83] prior to the measurement, and by choosing different gradient amplitudes in the three encoding directions.
The results confirm that blood suppression is beneficial for MR thermometry of the heart as indicated by the improved temperature stability in the myocardium. This is most likely due to reduced partial volume effects at the myocardium-blood interface and to a better performance of the motion correction algorithms when presented with images with improved myocardium-cavity CNR. The evaluation of the temporal mean of temperature shows a small offset of less than 1 °C which may be due to residual displacements or phase variations. Based on the average temperature stabilities and SNR/CNR values in the ventricular septum, IS in combination with TFE-EPI is the preferred combination for the presented implementation.

4.7.3 Image quality

The measured SNR/CNR values in the ventricular septum indicated that the applied blood suppression was able to significantly increase the CNR between the myocardium and the cavity. It was also found that the application of blood suppression typically led to an increased SNR in the ventricular septum. As all blood suppression methods are designed to cancel the signal of moving spins whilst also tissue spins may not remain completely unaffected, this result seems counterintuitive. It may be attributed to a decreased spatial standard deviation of the signal, potentially as a result of reduced partial volume flow effects. Depending on the phase encoding direction, the reduction of flow artifacts should be especially pronounced in the ventricular septum and the lateral part of the myocardium. However, no reliable evidence of this effect has been found when comparing the SNR in the different myocardial regions.

4.7.4 Motion correction

The applied affine algorithm for the compensation of in-plane motion is still limited when applied in the myocardium, as already small deformations or residual flow effects can cause false pixel displacements in the myocardium. The temperature calculation during RF heating may be severely biased by the resulting false displacements. A local

motion estimation algorithm [2] may be helpful, but may produce false corrections when presented with insufficient flow suppression. Hence, the development of more elaborated motion correction techniques will be the subject of future work. In 7 of the 64 dynamic imaging series (100 images each), 2 to 27 images (in average 9 images) containing artifacts from erroneous slice tracking were detected and removed. Without image rejection, temporal standard deviations of temperature above 20 °C were measured proving the necessity of this processing step for accurate thermometry in the heart.

The presented results for the temperature stability in the myocardium result from a combination of several effects including the quality of the motion and phase correction algorithms, the accuracy of the applied navigator slice tracking technique, and the efficiency of the applied blood suppression methods. As a result, they allow only limited statements about the respective contributions of each parameter onto the temperature stability. Finally, the conclusions of this work are based on the precision of MR thermometry in the absence of heating. Hence, future work should further explore the presented method during RF heating.

Bibliography

[1] O. Seror, M. Lepetit-Coiffé, B. Le Bail, B. Denis De Senneville, H. Trillaud, C.T.W. Moonen, and B. Quesson. Real time monitoring of radiofrequency ablation based on MR thermometry and thermal dose in the pig liver in vivo. *Eur. Radiol.*, 18:408–16, 2008.

[2] B. Denis de Senneville, C. Mougenot, and C.T.W. Moonen. Real time adaptive methods for treatment of mobile organs by MRI controlled high intensity focused ultrasound. *Magn. Res. Med.*, 57:319–330, 2007.

[3] J. Ferlay, D.M. Parkin, and E. Steliarova-Foucher. Estimates of cancer incidence and mortality in europe in 2008. *Europ. J. Cancer*, 46:765–81, 2010.

[4] M.A. Hall-Craggs. Interventional mri of the breast: minimally invasive therapy. *Eur. Radiol.*, 10:59–62, 2000.

[5] T.L. Huston and R.M. Simmons. Ablative therapies for the treatment of malignant diseases of the breast. *Am. J. Surgery*, 189:694–01, 2005.

[6] C. Boetes, R.D.M. Mus, R. Holland, J.O. Barentsz, S.P. Strijk, T. Wobbes, J.H. Hendriks, and S.H. Ruys. Breast tumours: comparative accuracy of mr imaging relative to mammography and us for demonstrating extent. *Radiology*, 197:743–7, 1995.

[7] S.G. Orel, M.D. Schnall, C.M. Powell, M.G. Hochman, L.J. Solin, B.L. Fowble, and M.H. Torosian E.F. Rosato. Staging of suspected breast cancer: effect of mr imaging and mr-guided biopsy. *Radiology*, 196:115–22, 1995.

[8] W.A. Kaiser, S.O. Pfleiderer, and P.A. Baltzer. MRI-guided interventions of the breast. *J. Magn. Res. Im.*, 27(2):347–55, 2008.

[9] P.E. Huber, J.W. Jenne, R. Rastert, I. Simiantonakis, H.P. Sinn, H.J. Strittmatter, D. von Fournier, M.F. Wannenmacher, and J. Debus. A new noninvasive approach in breast cancer therapy using magnetic resonance imaging-guided focused ultrasound surgery. *Cancer Res.*, 61(23):8441–7, 2001.

[10] B. Denis De Senneville, B. Quesson, P. Desbarats, R. Salomir, J. Palussière, and C.T.W. Moonen. Atlas-based motion correction for on-line MR temperature mapping. *IEEE, ICIP*, Vol.III:2571–74, 2004.

[11] R. Stollberger, P.W. Ascher, D. Huber, W. Renhart, H. Radner, and F. Ebner. Temperature monitoring of interstitial thermal tissue coagulation using MR phase images. *J. Magn. Res. Im.*, 8:188–96, 1997.

[12] K. Kuroda, K. Oshio, A.H. Chung, and K. Hynynen. Temperature mapping using water proton chemical shift: A chemical shift selective phase mapping method. *Magn. Res. Med.*, 38:845–51, 1997.

[13] A. Cerussi, N. Shah, D. Hsiang, A. Durkin, J. Butler, and B.J. Tromberg. In vivo absorption, scattering, and physiologic properties of 58 malignant breast tumors determined by broadband diffuse optical spectroscopy. *J. Biomed. Opt.*, 11(4):044005, 2006.

[14] K. Hynynen, N.J. McDannold, R.V. Mulkern, and F.A. Jolesz. Temperature monitoring in fat with MRI. *Magn. Res. Med.*, 43:901–4, 2000.

[15] P. Steiner, R. Botnar, B. Dubno, G.G. Zimmermann, G.S. Gazelle, and J.F. Debatin. Radio-frequency-induced thermoablation: Monitoring with T1-weighted and proton-frequency-shift MR imaging in an interventional 0.5 T environment. *Radiology*, 206:803–10, 1998.

[16] R. Graumann, M. Deimling, T. Heilmann, and A. Oppelt. A new method for fast and precise T1 determination. In *Proc. 5th ISMRM meeting, Montreal*, 1986. p.922.

[17] G. Brix, L.R. Schad, M. Deimling, and W.J. Lorenz. Fast and precise T1 imaging using a TOMROP sequence. *Magn. Res. Im.*, 8:351–6, 1990.

[18] C. Bos, M. Lepetit-Coiffé, B. Quesson, and C.T.W. Moonen. Simultaneous monitoring of temperature and T1: Methods and preliminary results of application to drug delivery using thermosensitive liposomes. *Magn. Res. Med.*, 54:1020–4, 2005.

[19] R.K. Gupta. A new look at the method of variable nutation angle for the measurement of spin-lattice relaxation times using fourier transform NMR. *J. Magn. Res.*, 25:231–35, 1977.

[20] J. Homer and M.S. Beevers. Driven-equilibrium single-pulse observation of T1-relaxation: A reevaluation of a rapid new method for determining NMR spin-lattice relaxation times. *J. Magn. Res.*, 63:287–97, 1985.

[21] E.K. Fram, R.J. Herfkens, G.A. Johnson, G.H. Glover, J.P. Karis, A. Shimakawa, T.G. Perkins, and N.J. Pelc. Rapid calculation of T1 using variable flip angle gradient refocused imaging. *Magn. Res. Im.*, 5:201–8, 1987.

[22] K. Kuroda, T. Iwabuchi, M.K. Lam, M. Obara, M. Honda, K. Saito, M. Van Cauteren, and Y. Imai. Fat Temperature Imaging with T1 of Fatty Acid Species Using Multiple Flip Angle Multipoint Dixon Acquisitions. In *Proc. 18th ISMRM, Stockholm*, 2010. 1818.

[23] S. Hey, G. Maclair, B. Denis de Senneville, Y. Berber, B. Quesson, C.T.W. Moonen, and M. Ries. Real-Time Correction of Respiratory-Induced Field Disturbances for PRFS-Based MR-Thermometry in the Human Breast. In *Proc. 16th ISMRM, Toronto*, 2008. p. 198.

[24] S. Hey, G. Maclair, B. Denis de Senneville, M. Lepetit-Coiffé, Y. Berber, M.O. Köhler, B. Quesson, C.T.W. Moonen, and M. Ries. Online correction of respiratory-induced field disturbances for continuous MR-thermometry in the breast. *Magn. Res. Med.*, 61(6):1494–99, 2009.

[25] Y. Seppenwoolde, H. Shirato, K. Kitamura, S. Shimizu, M. van Herk, J.V. Lebesque, and K. Miyasaka. Precise and real-time measurement of 3D tumor motion in lung due to breathing and heartbeat, measured during radiotherapy. *Int. J. Radiat. Oncol. Biol. Phys.*, 53(4):822–34, 2002.

[26] G. Maclair, B. Denis de Senneville, M. Ries, B. Quesson, P. Desbarats, J. Benois-Pineau, and C.T.W. Moonen. PCA-based magnetic field modeling: Application for on-line MR temperature monitoring. *Int. Conf. Med. Image Comput. Comput. Assist. Interv.*, 10(Pt 2):411–19, 2007.

[27] S.M. Sprinkhuizen, N.H.G.M. Peters, K.L. Vinken, C.J.G. Bakker, and L.W. Bartels. Quantification and correction of motion-induced field disturbances for accurate PFRS-based MR thermometry. In *Proc. 6th interv. MRI symp., Leipzig*, 2006. p.113-6.

[28] A.V. Shmatukha and C.J.G. Bakker. Correction of proton frequency shift temperature maps for magnetic field disturbances caused by breathing. *Phys. Med. Biol.*, 51:4689–5, 2006.

[29] K.K. Vigen, B.L. Daniel, and K. Butts. Triggered, navigated, multi-baseline method for proton resonance frequency temperature mapping with respiratory motion. *Magn. Res. Med.*, 50:1003–10, 2003.

[30] D.C. Look and D.R. Locker. Time saving in measurement of NMR and EPR relaxation times. *Rev. Scient. Instr.*, 41(2):250, 1970.

[31] A.P. Crawley and R.M. Henkelman. A comparison of one-shot and recovery methods in T1 imaging. *Magn. Res. Med.*, 7:23–34, 1988.

[32] H.Z. Wang, S.J. Riederer, and J.N. Lee. Optimizing the precision in T1 relaxation estimation using limited flip angles. *Magn. Res. Med.*, 5:399–16, 1987.

[33] S.C. Deoni, B.K. Rutt, and T.M. Peters. Rapid combined T1 and T2 mapping using gradient recalled acquisition in the steady state. *Magn. Res. Med.*, 49(3):515–26, 2003.

[34] R.R. Ernst and W.A. Anderson. Application of Fourier transform spectroscopy to magnetic resonance. *Rev. Scient. Instr.*, 37:93–02, 1966.

[35] R. Treier, A. Steingoetter, M. Fried, W. Schwizer, and P. Boesiger. Optimized and combined T1 quantification in contrast-enhanced abdominal MRI. *Magn. Res. Med.*, 57:568–76, 2007.

[36] K. Kuroda, M. Obara, M. Van Cauteren, M. Honda, and Y. Imai. Temperature dependence of relaxation times in fatty acid components and its consideration for MR thermometry in adipose tissue. In *Proc. 17th ISMRM, Honolulu, Hawaii*, 2009. 2533.

[37] T.M. Allen and P.R. Cullis. Drug delivery systems: entering the mainstream. *Science*, 303(5665):1818–22, 2004.

[38] V.P. Torchilin. Targeted pharmaceutical nanocarriers for cancer therapy and imaging. *AAPS J.*, 9(2):E128–47, 2007.

[39] E. Unger, D.K. Shen, G.L. Wu, and T. Fritz. Liposomes as MR contrast agents: Pros and cons. *Magn. Res. Med.*, 22:304–8, 1991.

[40] M. de Smet, S. Langereis, S. van den Bosch, and H. Grüll. Temperature-sensitive liposomes for doxorubicin delivery under MR guidance. *J. Controlled Release*, 143(1):120–7, 2010.

[41] M. de Smet, E. Heijman, S. Langereis, N. Hijnen, and H. Grüll. Magnetic Resonance Imaging of High Intensity Focused Ultrasound mediated drug delivery from temperature sensitive liposomes: An in vivo proof-of-concept study. *J. Controlled Release*, 2010. in press.

[42] S. Hey, A. Cernicanu, B. Denis de Senneville, S. Roujol, M. Ries, P. Jaïs, C.T.W. Moonen, and B. Quesson. Feasibility of MR-thermometry with blood suppression on the human heart at 3T. In *Proc. 18th ISMRM, Stockholm*, 2010. #289.

[43] M. Reardon and A.J. Camm. Atrial fibrillation in the elderly. *Clin. Cardiol.*, 19:765–75, 1996.

[44] J.B. Taylor and D.J. Triggle. *Comprehensive Medicinal Chemistry II.* Elsevier, 2007.

[45] D. Dobrev and S. Nattel. New antiarrhythmic drugs for treatment of atrial fibrillation. *Lancet*, 375(9721):1212–23, 2010.

[46] A. Chugh and F. Morady. Atrial fibrillation: Catheter ablation. *J. Interv. Card. Electrophysiol.*, 16:15–26, 2006.

[47] P. Jaïs, B. Cauchemez, L. Macle, E. Daoud, P. Khairy, R. Subbiah, M. Hocini, F. Extramiana, F. Sacher, P. Bordacher, G. Klein, R. Weerasooriya, J. Clémenty, and M. Haïssaguerre. Catheter ablation versus antiarrhythmic drugs for atrial fibrillation: The A4 study. *Circulation*, 118(24):2498–5, 2008.

[48] J. Ector, S. de Buck, W. Huybrechts, D. Nuygens, S. Dymarkowski, J. Bogaert, F. Maes, and H. Heidbüchel. Biplane three-dimensional augmented fluoroscopy as single navigation tool for ablation of atrial fibrillation: Accuracy and clinical value. *Heart Rhythm*, 5:957–64, 2008.

[49] Z.M. Hijazi, K. Shivkumar, and D.J. Sahn. Intracardial echocardiography during interventional and electrophysiological cardiac catheterization. *Circulation*, 119:587–96, 2009.

[50] M.J. Lacomis, W. Wigginton, C. Fuhrman, D. Schwarzman, R.D. Armfeld, and K.M. Pealer. Multi-detector row CT of the left atrium and pulmonary veins before radio-frequency catheter ablation for atrial fibrillation. *Radiographics*, 23:S35–S48, 2003.

[51] T. Dickfeld. Magnetic resonance imaging and radiofrequency ablations. *Herzschr. Elektrophys.*, 18:147–56, 2007.

[52] Z.J. Malchano, P. Neuzil, R.C. Cury, G. Holmvang, J. Weichet, E.J. Schmidt, J.N. Ruskin, and V.Y. Reddy. Integration of cardiac CT/MR imaging with three-dimensional electroanatomical mapping to guide catheter manipulation in the left atrium: Implications for catheter ablation of atrial fibrillation. *J. Cardiovasc. Electrophysiol.*, 17:1221–29, 2006.

[53] F. Saremi and M. Tafti. The role of computed tomography and magnetic resonance imaging in ablation procedures for treatment of atrial fibrillation. *Semin. Ultrasound CT MR*, 30(2):125–56, 2009.

[54] A. Berruezo, J.T. Ortiz-Peréz, E. Guasch, D. Tamborero, E. Silva, T.M. de Caralt, R.J. Perea, T. Boussy, L. Mont, and J. Brugada. Noninvasive evaluation of radiofrequency lesions in the human ventricular myocardium by contrast-enhanced cardiac magnetic resonance. *Circulation*, 2:208–11, 2009.

[55] S. Roujol, M. Ries, B. Quesson, C.T.W. Moonen, and B. Denis de Senneville. Real-time MR-thermometry and dosimetry for interventional guidance on abdominal organs. *Magn. Res. Med.*, 63(4):1080–7, 2010.

[56] V. Rieke, K.K. Vigen, G. Sommer, B.L. Daniel, J.M. Pauly, and K. Butts. Referenceless PRF shift thermometry. *Magn. Res. Med.*, 51(6):1223–31, 2004.

[57] C. Weidensteiner, B. Quesson, B. Caire-Gana, N. Kerioui, A. Rullier, H. Trillaud, and C.T.W. Moonen. Real-time MR temperature mapping of rabbit liver in vivo during thermal ablation. *Magn. Res. Med.*, 50(2):322–30, 2003.

[58] E.M. Haacke, Brown R.W., Thompson M.R., and Venkatesan R. *Magnetic Resonance Imaging: Physical principles and sequence design.* John Wiley & Sons, New York, 1999.

[59] R.R. Edelman, D. Chien, and D. Kim. Fast selective black blood MR imaging. *Radiology*, 181:655–60, 1991.

[60] R. Noeske, F. Seifert, K.-H. Rhein, and H. Rinneberg. Human cardiac imaging at 3 T using phased array coils. *Magn. Res. Med.*, 44:978–82, 2000.

[61] I. Koktzoglou, Y.C. Chung, V. Mani, T.J. Carroll, M.D. Morasch, G. Mizsei, O.P. Simonetti, Z.A. Fayad, and D. Li. Multislice dark-blood carotid artery wall imaging: a 1.5 T and 3.0 T comparison. *J. Magn. Res. Im.*, 23(5):699–5, 2006.

[62] H.K. Song, A.C. Wright, R.L. Wolf, and F.W. Wehrli. Multislice double inversion pulse sequence for efficient black-blood MRI. *Magn. Res. Med.*, 47:616–20, 2002.

[63] V.L. Yarnykh and C. Yuan. Multislice double inversion-recovery black-blood imaging with simultaneous slice reinversion. *J. Magn. Res. Im.*, 17:478–83, 2003.

[64] J.P. Felmlee and R.L. Ehman. Spatial presaturation: A method for suppressing flow artifacts and improving depiction of vascular anatomy in MR imaging. *Radiology*, 164:559–64, 1987.

[65] J. Wang, V.L. Yarnykh, T. Hatsukami, B. Chu, N. Balu, and C. Yuan. Improved suppression of plaque-mimicking artifacts in black-blood carotid atherosclerosis imaging using a multislice motion-sensitized driven-equilibrium (MSDE) turbo spin-echo (TSE) sequence. *Magn. Res. Med.*, 58:973–81, 2007.

[66] T.D. Nguyen, L. de Rochefort, P. Spincemaille, M.D. Cham, J.W. Weinsaft, M.R. Prince, and Y. Wang. Effective motion-sensitizing magnetization preparation for black blood magnetic resonance imaging of the heart. *J. Magn. Res. Im.*, 28:1092–0, 2008.

[67] I. Koktzoglou and D. Li. Diffusion-prepared segmented steady-state free precession: Application to 3D black-blood cardiovascular magnetic resonance of the thoracic aorta and carotid artery walls. *J. Cardiovasc. Magn. Res.*, 9:33–42, 2007.

[68] M. Salerno, F.H. Epstein, and C.M. Kramer. Diffusion-prepared dark blood delayed enhancement imaging for improved detection of subendocardial infarcts. In *Proc. 12th SCMR*, 2009. vol. II(Suppl I):O10.

[69] J. Bundy, O. Simonetti, G. Laub, and P. Finn. TrueFISP imaging of the heart. In *Proc. 7th ISMRM, Berkeley (Calif)*, 1999. p 1282.

[70] J.C. Carr, O. Simonetti, J. Bundy, D. Li, S. Pereles, and J.P. Finn. Cine MR angiography of the heart with segmented true fast imaging with steady-state precession. *Radiology*, 219:828–34, 2001.

[71] K. Scheffler. Fast frequency mapping with balanced SSFP: Theory and Application to Proton-Resonance Frequency Shift Thermometry. *Magn. Res. Med.*, 51:1205–11, 2004.

[72] W.R. Nitz, A. Oppelt, W. Renz, C. Manke, M. Lenhart, and J. Link. On the heating of linear conductive structures as guide wires and catheters in interventional MRI. *J. Magn. Res. Im.*, 13:105–14, 2001.

[73] J.A. de Zwart, P. van Gelderen, D.J. Kelly, and C.T.W. Moonen. Fast magnetic-resonance temperature imaging. *J. Magn. Res. B*, 112(1):86–90, 1996.

[74] K.P. Pruessmann, M. Weiger M.B. Scheidegger, and P. Boesiger. SENSE: sensitivity encoding for fast MRI. *Magn. Res. Med.*, 42(5):952–62, 1999.

[75] G. Liu, G. Sobering, J. Duyn, and C.T.W. Moonen. A functional MRI technique combining principles of echo-shifting with a train of observations (PRESTO). *Magn. Res. Med.*, 30:764–8, 1993.

[76] K. Pearson. Mathematical contributions to the theory of evolution. III. Regression, heredity and panmixia. *Philos. Trans. Royal Soc. London Ser. A*, 187:253–318, 1896.

[77] H. Gudbjartsson and S. Patz. The Rician distribution of noisy MRI data. *Magn. Res. Med.*, 34(6):910–4, 1995.

[78] S. Roujol, B.Denis de Senneville, G. Maclair, S. Hey, P. Jaïs, C.T.W. Moonen, and B. Quesson. Advances in real-time MR temperature mapping of the human heart. In *Proc. 17th ISMRM, Hawaii*, 2009. p.443.

[79] Y. Isihara, A. Calderon, H. Watanabe, K. Okamoto, Y. Suzuki, K. Kuroda, and Y. Suzuki. A precise and fast temperature mapping using water proton chemical shift. *Magn. Res. Med.*, 34(6):814–23, 1995.

[80] D.A. Feinberg, J.C. Hoenninger, L.E. Crooks, L. Kaufman, J.C. Watts, and M. Arakawa. Inner volume MR imaging: Technical concepts and their application. *Radiology*, 156:743–7, 1985.

[81] B.J. Wilm, U. Gramper, A. Henning, K.P. Pruessmann, S.S. Kollias, and P. Boesiger. Diffusion-weighted imaging of the entire spinal cord. *NMR Biomed.*, 22(2):174–81, 2009.

[82] A. Bornstedt, P. Bernhardt, V. Hombach, J. Kamenz, J. Spiess, A. Subgang, and V. Rasche. Local excitation black blood imaging at 3T: Application to the carotid artery wall. *Magn. Res. Med.*, 59:1207–11, 2008.

[83] U. Katscher, P. Börnert, C. Leussler, and J. S. van den Brink. Transmit SENSE. *Magn. Res. Med.*, 49:144–50, 2003.

Part III

High precision volumetric temperature control of moving targets

Introduction

An important issue for HIFU-induced thermotherapy is the ability to control the intensity and location of the treatment. Once reliable temperature information is available, there is still need to ensure an immediate response to temperature changes in the targeted tissue. Hence, a direct coupling with the monitoring equipment is desirable. For that purpose, different control strategies are imaginable, such as fuzzy logic [1–3], model predictive control (MPC) [4, 5] or Proportional, Integral and Derivative (PID) control. Especially, temperature feedback loops based on the latter approach have gained interest for temperature control during hyperthermia as early as 1990 [6]. Since then, several modifications have been proposed. However, there is still need for improved algorithms especially for applications requiring high precision temperature control like local drug delivery [7–9] and the control of gene therapy using heat-sensitive promoters [10, 11]. The following chapter 5 will deal with an improved implementation of the conventional PID controller. This is achieved by online adaptation of the controller gains in order to avoid overshoots and to reduce instabilities due to lack of knowledge about the thermal properties of the tissue.
While this algorithm is evaluated on static, single point sonications, chapter 6 will present an advanced strategy for 3D trajectory optimization based on volumetric temperature and thermal dose maps. In order to achieve a pre-defined temperature or thermal dose in a large volume, an efficient control strategy is required. Based on the algorithm developed by Mougenot et al [12], 3D thermal dose maps are employed to compute an optimized trajectory of sonications points. The parallel adaptation of the focal point position to compensate periodical motion ensures spatial accuracy of the heating even with motion amplitudes and frequencies similar to those encountered in vivo.

5 Adaptive Proportional-Derivative-Integral control for improved temperature control

Online temperature control of focused ultrasound tissue ablation using a PID feedback loop has been shown to be feasible both for single point sonications [13] as well as for volume ablations under 3D temperature control [14]. Adaptive feedback loops have also been applied successfully for volumetric HIFU ablations in the prostate [15]. Reliable temperature control requires the algorithm to fulfill certain conditions:

1. The temperature in the focal point should reach the target temperature as fast as possible without oscillations.

2. No temperature overshoot should occur because tissue cooling is only due to diffusion and perfusion processes. As they act on longer time scales than the ultrasound heating, undesired damage in the surrounding tissue can be a result.

3. Once the target temperature is reached, the temperature should remain stable for a pre-defined time.

A powerful tool for the evaluation of the stability and convergence characteristics of a PID controller lies in the analysis of the closed-loop transfer function of the controller. This will allow in the following chapter to find necessary and sufficient conditions which have to be fulfilled by the controller gains to ensure stability and fast convergence. By incorporating a model of the temperature evolution in tissue, uncertainties in the determination of the thermal coefficients of the tissue can be considered in the stability analysis. Nevertheless, the retrieved optimized controller gains suppose ideal conditions such as unlimited power and the ability to cool instantaneously. Under experimental conditions, power restrictions in order to prevent cavitation or as a result of hardware limitations of the ultrasound transducer can lead to overshoots of several degrees Celsius if both proportional and integral control are used. As a potential solution, a modified approach including online adaptation of the controller gains [16, 17] as a function of the temperature error, the measurement noise and an assumed uncertainty in the determination of the absorption coefficient will be explored.

5.1 Transfer function and stability [18, 19]

A very efficient way to evaluate the response of a controller system to certain input values is given by the analysis of the closed-loop transfer function of the system. This formalism uses the Laplace transform (for continuous systems) [20] or Z-transform (for discrete systems) [21] to transform the time domain signal into the frequency domain similarly to the Fourier transform.

5.1.1 Laplace and Z-transform

The Laplace transform is defined as

$$X(s) = \mathcal{L}\{x(t)\} = \int_0^\infty e^{-st} x(t) \mathrm{d}t \quad , s \in \mathbb{C} \quad , \tag{5.1}$$

whereas the unilateral Z-transform (defined for positive times or $n \geq 0$) of a discrete signal $x(n)$ reads

$$X(z) = \mathcal{Z}\{x(n)\} = \sum_{n=0}^{\infty} x(n) z^{-n} \quad , z \in \mathbb{C} \quad . \tag{5.2}$$

By definition, the relationship between Laplace and Z-transform is given by $z = \mathrm{e}^{s\Delta t}$ with the sampling period Δt. The transformation of a continuous time signal into a discrete expression can be achieved using different methods which can be visualized as follows using an example:
The derivative of a time dependent function $f(t)$ can be transformed into frequency space using the Laplace transform

$$\mathcal{L}\left\{\frac{\mathrm{d}f(t)}{\mathrm{d}t}\right\} = sf(s) \quad , f(s) = \mathcal{L}\{f(t)\} \quad . \tag{5.3}$$

Using backward differences, the Z-transform reads

$$\mathcal{Z}\left\{\frac{\mathrm{d}f(t)}{\mathrm{d}t}\right\} = \frac{\left(1 - z^{-1}\right)}{\Delta t} f(z) \quad , f(z) = \mathcal{Z}\{f(t)\} \quad . \tag{5.4}$$

This conversion corresponds to using the method of Euler for the approximation of the derivative and consequently suffers from the same limitations if $\Delta t \ll 1$ is not fulfilled. An alternative method using the trapezoid rule known from integration, is the bilinear transform or *Tustin's rule*. Starting with the Laplace transform, $s = \dfrac{2}{\Delta t} \dfrac{1 - z^{-1}}{1 + z^{-1}}$ is used as a replacement leading to

$$\mathcal{Z}\left\{\frac{\mathrm{d}f(t)}{\mathrm{d}t}\right\} = \frac{2}{\Delta t} \frac{1 - z^{-1}}{1 + z^{-1}} f(z) \quad . \tag{5.5}$$

This conversion represents a better approximation of the continuous case even for comparable large Δt.
As MR measurements represent a time-discrete signal, it would be straight forward to use the Z-transform for their description. However, the complexity of the resulting expressions renders their interpretation difficult. For this reason, it is more intuitive to use the Laplace transform for the following theoretical considerations while for ease of implementation the discrete equations will be derived using backward differences.

5.1.2 Application to a simple PID feedback loop

Figure 5.1 shows the closed loop system for heating in tissue using a PID controller. For each of the three different parts, separate transfer functions G can be defined as

$$G = \frac{\text{output}}{\text{input}} \quad .$$

A PID controller with output $P_w(t)$ at instant t, is defined as follows

$$P_w(t) = K_P \varepsilon(t) + K_I \int_0^t \varepsilon(\tau) \mathrm{d}\tau + K_D \frac{\varepsilon(t)}{\mathrm{d}t} \quad , \tag{5.6}$$

with $\varepsilon(t) = \theta(t) - T_m(t)$ being the error between the target temperature $\theta(t)$ and the measured temperature $T_m(t)$. The corresponding Laplace transform reads

$$P_w(s) = \left(K_P + \frac{K_I}{s} + K_D s \right) \varepsilon(s) \quad , \tag{5.7}$$

with $P_w(s) = \mathcal{L}\{P_w(t)\}$ and $\varepsilon(s) = \mathcal{L}\{\varepsilon(t)\}$. As a result, the transfer function for the PID controller $G_P(s)$ is given by

$$G_P(s) = \frac{P_w(s)}{\varepsilon(s)} = K_P + \frac{K_I}{s} + K_D s \quad . \tag{5.8}$$

The description of the heating process in tissue is complicated (sect. 2.1.4), but can be simplified for this explanation neglecting perfusion and diffusion effects in eq. (2.4)

$$\frac{\mathrm{d}T(t)}{\mathrm{d}t} = \alpha P_w(t) \quad , \tag{5.9}$$

with the absorption coefficient α and the actual tissue temperature $T(t)$. After Laplace transform, it follows

$$sT(s) = \alpha P_w(s) \quad , \tag{5.10}$$

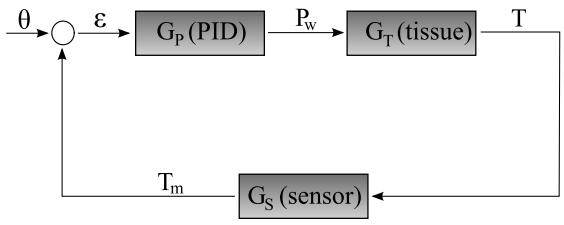

Figure 5.1: Simple closed loop system for heating in tissue using a PID controller. The input of the PID is given by the error ε, the difference between the target temperature θ and the measured temperature T_m. The output of the PID controller is the power P to be applied to heat the tissue. This results in a modified tissue temperature T which is finally measured by a sensor yielding the measured temperature for the next loop. G_P, G_T and G_S are the transfer functions of the PID, the tissue and the sensor.

leading to the transfer function $G_T(s)$ of the tissue

$$G_T(s) = \frac{T(s)}{P_w(s)} = \frac{\alpha}{s} \quad . \tag{5.11}$$

Finally, the measurement process can be described by a transfer function $G_S(s)$ including, e.g. measurement noise and partial volume effects. However, for the following analysis, $G_S(s) = 1$ will be assumed. Hence, as a summary, the following relations have been found

$$\begin{aligned} T(s) &= G_T(s)P_w(s) \\ P_w(s) &= G_P(s)\varepsilon(s) \\ T_m(s) &= G_S(s)T(s) \\ \varepsilon(s) &= \theta(s) - T_m(s) \quad . \end{aligned} \tag{5.12}$$

They can now be used to express the closed-loop transfer function with the derived separate transfer functions

$$\begin{aligned} \varepsilon(s) \overset{G_P(s)}{\longrightarrow} P_w(s) \overset{G_T(s)}{\longrightarrow} T(s) \overset{G_S(s)}{\longrightarrow} T_m(s) \\ \varepsilon(s) = \theta(s) - T_m(s) \quad . \end{aligned} \tag{5.13}$$

The goal is to eliminate $\varepsilon(s)$ in order to evaluate the measured temperature $T_m(s)$ as a result of the input target temperature $\theta(s)$

$$T_m(s)\left(1 + G_S(s)G_T(s)G_P(s)\right) = G_T(s)G_P(s)\theta(s) \quad . \tag{5.14}$$

Hence, the final transfer function of this closed loop system $H(s)$ reads

$$H(s) = \frac{T_m(s)}{\theta(s)} = \frac{G_T(s)G_P(s)}{1 + G_S(s)G_T(s)G_p(s)} \quad . \tag{5.15}$$

The knowledge of $H(s)$ enables to determine the response $T_m(s)$ of the system to an arbitrary input function $\theta(s)$. In the time domain, $h(t) = \mathcal{L}^{-1}\{H(s)\}$ is called the impulse response of the system as it can be used to describe the response of the system to a unit step function $\theta_{\text{step}}(s) = 1/s$. Furthermore, an evaluation of the poles of the transfer function (roots of the denominator) allows a direct analysis of the system stability. For the case of a linear system with input, the formalism of bounded-input-bounded-output (BIBO) stability is applicable [18, 19]. A linear system is BIBO asymptotically stable if its impulse response is absolutely integrable, that means that its ℓ^1 norm exists

$$\int_0^\infty |h(t)| \, \mathrm{d}t = \|h\|_1 < \infty \quad . \tag{5.16}$$

It can be shown that this is fulfilled if the real parts of all poles of the transfer function $H(s)$ lie strictly in the open left half of the complex plane (Fig. 5.2). For the detailed derivation of this characteristic see Appendix A.2.1. For the Z-transform, this is equivalent to the condition that the magnitudes of all poles of the transfer function $H(z)$ must

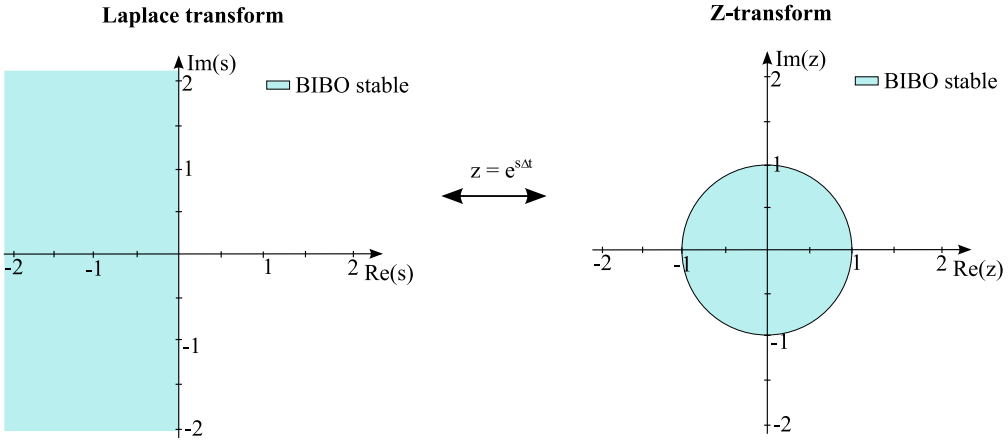

Figure 5.2: Region of convergence (light blue) for BIBO stability. For the Laplace transform, the poles of the transfer function must lie in the open left half of the complex plane, while for the Z-transform, the magnitudes of all poles of the transfer function of the controller have to lie within the unit circle.

lie within the unit circle in the Z-plane (Fig. 5.2). The evaluation of the poles s_p of the retrieved transfer function $H(s)$ yields the characteristic polynome of second order

$$0 = s_p^2 \left(1 + \alpha K_D\right) + s_p \alpha K_P + \alpha K_I \quad , \tag{5.17}$$

and consequently the poles of the transfer function

$$s_{p1/2} = -\frac{1}{2}\frac{\alpha K_P}{\left(1 + \alpha K_D\right)} \pm \sqrt{\frac{1}{4}\left(\frac{\alpha K_P}{1 + \alpha K_D}\right)^2 - \frac{\alpha K_I}{1 + \alpha K_D}} \quad . \tag{5.18}$$

As shown in Appendix A.2.2, this controller is always BIBO stable since $Re\left(s_{p1/2}\right) < 0$ for all K_P, K_I, K_D, α. Furthermore, the condition

$$\frac{1}{4}\left(\frac{\alpha K_P}{1 + \alpha K_D}\right)^2 \geq \frac{\alpha K_I}{1 + \alpha K_D} \tag{5.19}$$

defines the parameter combination for which convergence is achieved without oscillations corresponding to $Im(s_{p1/2}) = 0$ (eq. (A.18)). These characteristics of the PID controller are visualized in Fig. 5.3 for different combinations of K_P and K_I using the corresponding impulse responses (Fig. 5.3a) and the positions of the poles in the Z-plane (Fig. 5.3b). For all displayed cases, the poles remain within the unit circle following the theory. Furthermore, it can be observed that for increasing proportional gains, the real part of the poles increases and approaches the borders of the unit circle without crossing it (Fig. 5.3b). If eq. (5.19) is fulfilled, no oscillations occur as the imaginary part of the poles remains zero (second and third graph of Fig. 5.3a). However, the controller converges faster if high proportional gains coupled to integral gains strictly fulfilling

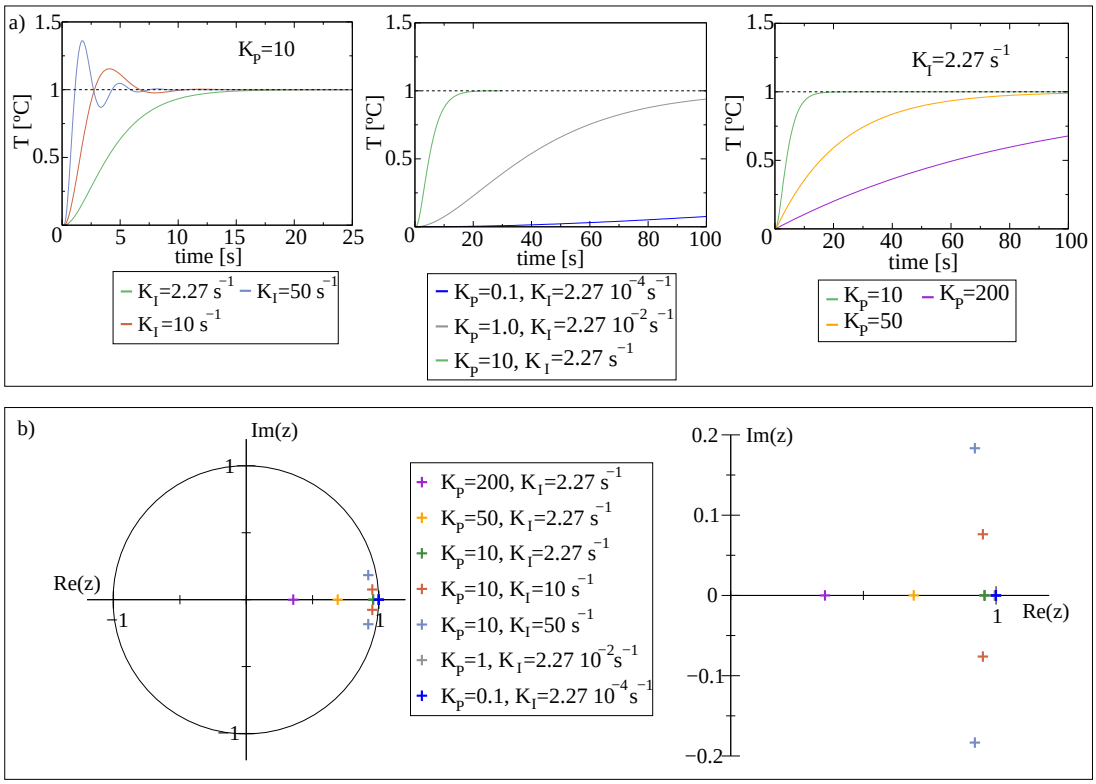

Figure 5.3: Stability evaluation of a simple PID controller: a) Impulse responses for increasing integral gain K_I (left graph), decreased proportional gain (central graph), and for increasing proportional gains (right graph). The other parameters remained fixed at $K_D = 1\,\mathrm{s}$, $\Delta t = 0.1\,\mathrm{s}$, and $\alpha = 0.3\,\mathrm{K\,J^{-1}}$. The input temperature is shown as a black dashed line. b) Position of the poles of $H(z)$ in the Z-plane for the different cases displayed in a). The unit circle is depicted by a black line. A zoom of the left graph is shown in right image.

eq. (5.19) are chosen. In the case, where eq. (5.19) is not fulfilled, damped oscillations occur, visible in a non-zero imaginary part of the poles. These oscillations show increased amplitudes and frequencies proportional to K_I.

5.1.3 Application to heating in tissue

Considering the application of a PID control algorithm to focused ultrasound heating, the classical PID algorithm (sect. 2.2.1) can be combined with a realistic model for the temperature evolution in tissue [22] considering diffusion and perfusion effects in addition to heat absorption. For this purpose, the derivative term of the measured temperature will be replaced by a prediction term which includes the physical model of heat evolution in tissue. Subsequently, the resulting controller equation will be reformulated to be able to define the transfer functions of the different parts of the controller in analogy to the simple PID controller discussed above. As a first step, the classical PID equation

(eq. (2.6)) will be separated into three different parts containing the target temperature $\theta(t)$, the measured temperature $T_m(t)$ and the derivative of the measured temperature

$$\begin{aligned} 0 &= K_P\left(\theta(t) - T_m(t)\right) + K_I \int_0^t \left(\theta(\tau) - T_m(\tau)\right) \mathrm{d}\tau + K_D \frac{\left(\theta(t) - T_m(t)\right)}{\mathrm{d}t} \\ &= K_P\theta(t) + K_I \int_0^t \theta(\tau)\mathrm{d}\tau + K_D \frac{\theta(t)}{\mathrm{d}t} \\ &\quad - \left(K_P T_m(t) + K_I \int_0^t T_m(\tau)\mathrm{d}\tau \right) - K_D \frac{T_m(t)}{\mathrm{d}t} \quad . \end{aligned} \tag{5.20}$$

Finally, the derivative of the temperature is replaced by the HTE (eq. (2.4)) using the measured temperature $T_m(t)$ instead of the tissue temperature $T(\vec{r}_{\mathrm{fp}}, t)$ at the focal point position $\vec{r}_{\mathrm{fp}}$

$$K_D \frac{T_m(t)}{\mathrm{d}t} = K_D \alpha_s P_w(t) + K_D D_s \vec{\nabla}^2 T_m(\vec{r}, t) - K_D \omega_s T_m(t) \quad , \tag{5.21}$$

assuming spatially constant diffusion, absorption and perfusion coefficients $D(\vec{r}) = D_s$, $\alpha(\vec{r}) = \alpha_s$ and $\omega(\vec{r}) = \omega_s$. Here, the index "s" indicates, that these are estimated thermal coefficients used for the prediction of the thermal behavior of the tissue. The final expression for the modified PID controller is then given by

$$\begin{aligned} 0 &= K_P\theta(t) + K_I \int_0^t \theta(\tau)\mathrm{d}\tau + K_D \frac{\theta(t)}{\mathrm{d}t} \\ &\quad - K_P T_m(t) - K_I \int_0^t T_m(\tau)\mathrm{d}\tau \\ &\quad - K_D \alpha_s P_w(t) - K_D D_s \vec{\nabla}^2 T_m(\vec{r}, t) + K_D \omega_s T_m(t) \quad . \end{aligned} \tag{5.22}$$

This equation provides a means to control the output of the ultrasound transducer based on temperature measurements in the tissue and the knowledge of certain tissue properties. After Laplace transformation, the final expression reads

$$0 = \left(K_P + \frac{K_I}{s} + K_D s\right)\theta(s) - \left(K_P + \frac{K_I}{s}\right) T_m(s) \tag{5.23}$$

$$- K_D \mathcal{L}\left\{\alpha_s P_w(t\right\}) - K_D \mathcal{L}\left\{ D_s \vec{\nabla}^2 T_m(\vec{r}, t) - \omega_s T_m(t) \right\} \tag{5.24}$$

Division by the term $\left(K_P + \frac{K_I}{s} + K_D s\right)$ allows to identify the separate terms of the modified controller

$$\begin{aligned} 0 &= \theta(s) - \frac{\left[\left(K_P + \frac{K_I}{s}\right) T_m(s) - K_D \mathcal{L}\left\{D_s \vec{\nabla}^2 T_m(\vec{r}_{\mathrm{fp}}, t) - \omega_s T_m(t)\right\}\right]}{\left(K_P + \frac{K_I}{s} + K_D s\right)} \\ &\quad - \frac{K_D \mathcal{L}\left\{\alpha_s P_w(t)\right\}}{\left(K_P + \frac{K_I}{s} + K_D s\right)} \quad . \end{aligned} \tag{5.25}$$

Temperature evolution and simulation in tissue The Laplace transform of the HTE is not straightforward due to the spatial character of the diffusion term. As an approximation, heat evacuation in the Laplace representation will be modeled by a perfusion-like term with adapted heat evacuation coefficient $B \stackrel{\mathrm{def}}{=} aD + \omega$. In this model, a is an empirically determined constant which ensures correct units and represents a first order approximation of $T(\vec{r}_{\mathrm{fp}}, t)/\vec{\nabla} T(\vec{r}, t)$. Consequently, the Laplace transform of the HTE reads

$$\begin{aligned} \mathcal{L}\left\{\frac{\mathrm{d}T}{\mathrm{d}t}\right\} &= \mathcal{L}\left\{\alpha P_w(t) - D\vec{\nabla}^2 T(\vec{r}_{\mathrm{fp}}, t) - \omega T(t)\right\} \\ T(s)s &= \alpha P_w(s) - BT(s) \quad . \end{aligned} \tag{5.26}$$

The actual heating in tissue can then be described by the transfer function G_{TM}

$$T(s) = \frac{\alpha}{s + B} P_w(s) = G_{TM} P_w(s) \quad . \tag{5.27}$$

For the simulation of the temperature in the PID algorithm, eq. (5.27) has to be modified using $\alpha = \alpha_S$, $B = B_S$ and $T(s) = T_m(s)$.

Closed-loop transfer function of the system and stability analysis Using eq. (5.26) the final form of the modified controller equation (5.25) reads

$$0 = \theta(s) - \frac{\left(K_P + \frac{K_I}{s}\right) - K_D B_s}{\left(K_P + \frac{K_I}{s} + K_D s\right)} T_m(s) - \frac{K_D \alpha_s}{\left(K_P + \frac{K_I}{s} + K_D s\right)} P_w(s) \quad , \tag{5.28}$$

and can be simplified as follows

$$0 = \theta(s) - G_{PM} T_m(s) - G_{AS} P_w(s) \quad . \tag{5.29}$$

The expressions for G_{PM} and G_{AS} are then defined as

$$G_{PM} = \frac{\left(K_P + \frac{K_I}{s}\right) - K_D B_s}{\left(K_P + \frac{K_I}{s} + K_D s\right)} \tag{5.30}$$

$$G_{AS} = \frac{K_D \alpha_s}{\left(K_P + \frac{K_I}{s} + K_D s\right)} \tag{5.31}$$

In analogy to the simple PID controller presented in sect. 5.1.2, the corresponding

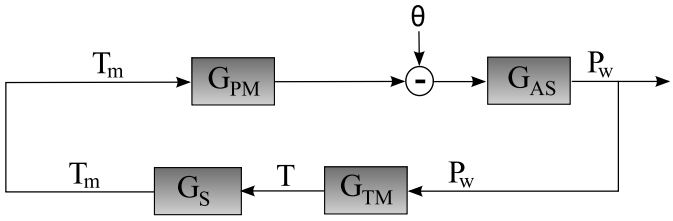

Figure 5.4: Scheme of the modified PID controller including a model of the temperature evolution in the tissue. G_{PM} acts on the measured temperature resulting in a prediction of the tissue temperature. The difference to the target temperature θ gives the output of the controller. After being modified by G_{AS} including an estimation of the tissue absorption, a new power value P_w is calculated. The actual temperature evolution in the tissue T is described by G_{TM} and measured as T_m via G_S.

graphical scheme of this system is displayed in Fig. 5.4. In contrast to the simple PID system with transfer function G_P (eq. 5.8), the modified transfer function of the controller G_{PM} acting on the measured temperature $T_m(s)$ introduces a degree of prediction by including the heat evacuation terms of the HTE. Furthermore, the controller output is modified by G_{AS} taking into account the assumed absorption coefficient of the tissue. Similar to the simple PID controller, the measured temperature is a result of the thermal reaction of the tissue described by an extended version of G_T (eq. 5.11) called G_{TM} and the sensor transfer function G_S. Then, it follows from eq. 5.29

$$P_w(s) = \frac{\theta(s) - G_{PM} T_m(s)}{G_{AS}} \tag{5.32}$$

$$T(s) = G_{TM} P_w(s) \tag{5.33}$$

$$T_m(s) = G_S T(s) \quad . \tag{5.34}$$

For the following considerations, $G_S = 1$ will be assumed. Combining eq. (5.32, 5.33, 5.34), a relationship between $\theta(s)$ and $T(s)$ can be found

$$T(s)\left(G_{AS} + G_{PM} G_{TM} G_S\right) = G_{TM} \theta(s) \quad , \tag{5.35}$$

leading to the closed-loop transfer function of the system

$$\begin{aligned} H(s) &= \frac{T(s)}{\theta(s)} \\ &= \frac{G_{TM}}{G_{AS} + G_{PM} G_{TM} G_S} \\ &= \frac{K_P s + K_I + K_D s^2}{K_P s + K_I + \dfrac{\alpha_s}{\alpha} K_D \left(s^2 + Bs\right) - K_D B_s s} \quad . \end{aligned} \tag{5.36}$$

As shown in Appendix A.2.3, the poles s_p of this function are then given as

$$\begin{aligned} s_{p1/2} &= -\frac{1}{2}\left(\frac{\alpha}{\alpha_s}\frac{K_P}{K_D} + \left(B - \frac{\alpha}{\alpha_s} B_s\right)\right) \\ &\quad \pm\sqrt{\frac{1}{4}\left(\frac{\alpha}{\alpha_s}\frac{K_P}{K_D} + \left(B - \frac{\alpha}{\alpha_s} B_s\right)\right)^2 - \frac{\alpha}{\alpha_s}\frac{K_I}{K_D}} \quad , \end{aligned} \tag{5.37}$$

leading to the following criterion for convergence without oscillations

$$\frac{1}{4}\left(\frac{\alpha}{\alpha_s}\frac{K_P}{K_D} + \left(B - \frac{\alpha}{\alpha_s} B_s\right)\right)^2 \geq \frac{\alpha}{\alpha_s}\frac{K_I}{K_D} \quad . \tag{5.38}$$

Furthermore,

$$-\frac{1}{2}\left(\frac{\alpha}{\alpha_s}\frac{K_P}{K_D} + \left(B - \frac{\alpha}{\alpha_s} B_s\right)\right) < 0 \tag{5.39}$$

has to be fulfilled to ensure stable convergence. For the ideal case, where $\alpha_s = \alpha$ and $B_s = B$, that means a perfect estimation of the heat coefficients used in the simulation, the system remains stable for all possible parameter choices and eq. (5.38) simplifies to

$$\frac{1}{4}\left(\frac{K_P}{K_D}\right)^2 \geq \frac{K_I}{K_D} \quad . \tag{5.40}$$

An interesting characteristic of this system is that its stability and convergence depend only on α/α_s independent of the true value of the absorption coefficient, while this is not the case for the heat evacuation term. The derivative gain K_D acts only as a scaling factor for the convergence and stability characteristics of the PID. Consequently, it is chosen as $K_D = 1\,\mathrm{s}$ for the following considerations. Equation (5.39) suggests further to assume $B_s = 0\,\mathrm{s}^{-1}$ in order to assure system stability. As the estimation of true tissue coefficients is always prone to errors, a good estimation of the upper bounds in eq. (5.38) can be found by neglecting the heat evacuation term entirely

$$\frac{1}{4}\left(\frac{\alpha}{\alpha_s}\frac{K_P}{K_D}\right)^2 \geq \frac{\alpha}{\alpha_s}\frac{K_I}{K_D} \quad . \tag{5.41}$$

5.2 Adaptive PID control

The PID controller described above is superior to the simple PID controller described in sect. 5.1.2 as it takes into account the possible difference between estimated and real heat coefficients of the tissue. This is an important improvement, since the tissue coefficients used as input values for the controller are generally apparent values which have been influenced by the measurement process. For an estimation of this effect, several additional factors have to be taken into account, such as the attenuation of the acoustic power in the tissue, losses during the transformation from electrical into acoustical power, or averaging of the measured temperature as a result of the restricted spatial resolution of the measurement. In contrast to the tissue absorption coefficient, the diffusion coefficient is hardly affected by these factors. Neglecting diffusion and perfusion, the apparent absorption coefficient α_{app} observed in the controlled voxel is given by

$$\alpha_{\mathrm{app}} = \mu \cdot a_{\mathrm{conv}} \frac{1}{P_w(t)} \iiint\limits_{\mathrm{voxel}} \frac{\mathrm{d}T(\vec{r},t)}{\mathrm{d}t} \mathrm{d}^3 r \quad , \tag{5.42}$$

where μ is the acoustic attenuation coefficient of the tissue, a_{conv} the conversion factor from electrical to acoustical power, and the integral covers the volume of the controlled voxel. This equation indicates that the apparent absorption coefficient will always depend on the chosen spatial resolution of the MR temperature images.
Moreover, the PID controller presented above, is based on constant controller gains K_P, K_I and K_D and does not consider hardware limitations which may lead to a maximal applicable power. A closer examination of the response properties of the PID controller suggests a more flexible algorithm based on adaptive coefficients. This concept is not new [16, 17] and has already been adapted for thermotherapy. Lin et al. [6] used a binary controller, which set the output power to the maximal available value if the temperature was below a certain threshold and employed a classical PID controller if the temperature was close to the set point. A more advanced adaptive implementation was presented by Sun et al. [23] where the adaptation function of the controller gains was found during the treatment by comparing the controller performance with a reference controller ensuring controller stability in the process. Working on low resolution MR temperature maps, this approach did not consider the influence of measurement noise which may lead to "unnecessary" adaptations during the treatment. Furthermore, as shown in eq. (5.39), the choice of erroneous heat evacuation coefficients may even lead to controller instabilities, whereas stable convergence without oscillations is assured if they are neglected. Finally, several presented approaches for temperature control used smooth target temperature profiles with rise times of $5 - 10\,\mathrm{min}$ [22, 24] to avoid overshoots. In order to accelerate the convergence towards the target temperature, it would be desirable to be able to choose target temperature profiles with rapid temperature changes. However, especially for step-like target temperature profiles, the cumulative effect of the integral part can lead to an overshoot (Fig 5.5). Here, the limited power and temporal resolution of the measurement results in a high temperature error $\varepsilon(\vec{r}_{\mathrm{fp}}, t)$ during a steep increase of the target temperature (part I in Fig 5.5). When the set point is finally reached the

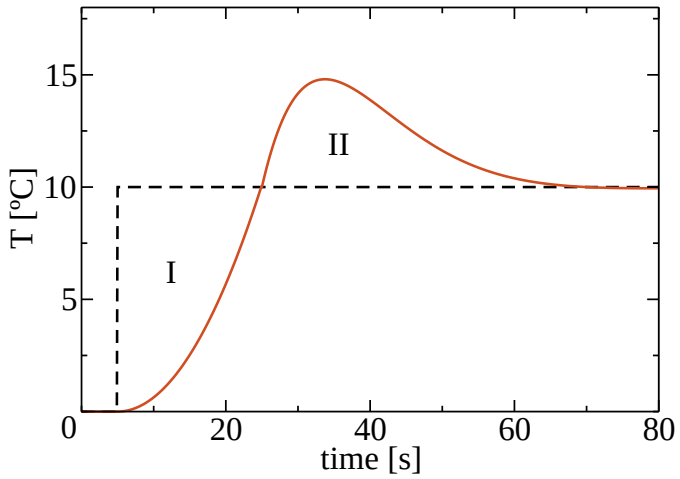

Figure 5.5: Example for a system response to a sharp increase in target temperature (dashed black line). In the beginning the system cannot follow the fast target temperature change and hence accumulates the resulting error in the integral part (part I). As a compensation effect, the system produces an overshoot (part II) after having reached the set point.

accumulated large negative integral part has to be compensated by the system, creating an overshoot (part II in Fig 5.5. This can be prevented if the integral and proportional coefficients K_I and K_P are adapted online as a function of the current error $\varepsilon(\vec{r}_{\mathrm{fp}}, t)$.

Proportional gain

In the following, the parameters defining the transfer functions for the controller gains are derived starting with the proportional gain. For this purpose, the resulting temperature change in the focal point within one time step (from n to $n+1$) $\Delta T = T_{n+1}(\vec{r}_{\mathrm{fp}}, t) - T_n(\vec{r}_{\mathrm{fp}}, t)$ will be examined during the heating phase where $\varepsilon > 0$. Considering proportional-derivative-only control, we can reformulate eq. (2.6) in a discretized form with temporal resolution Δt

$$0 = K_P \varepsilon_n + K_D \frac{\varepsilon_{n+1} - \varepsilon_n}{\Delta t} = K_P \varepsilon_n + K_D \frac{\Delta\theta}{\Delta t} - K_D \frac{\Delta T}{\Delta t} \quad , \tag{5.43}$$

with $\Delta\theta = \theta_{n+1}(t) - \theta_n(t)$. Reordering yields

$$\Delta T = \frac{K_P}{K_D} \varepsilon \, \Delta t + \Delta\theta \quad . \tag{5.44}$$

For optimal convergence, where the temperature change ΔT is equal to the current control error ε, and assuming $\Delta\theta = 0$ (for a step function this is always the case except for one time point), eq. (5.44) gives an estimation of the optimal proportional gain $K_P^{\min}$

$$K_P^{\min} = K_D / \Delta t \quad . \tag{5.45}$$

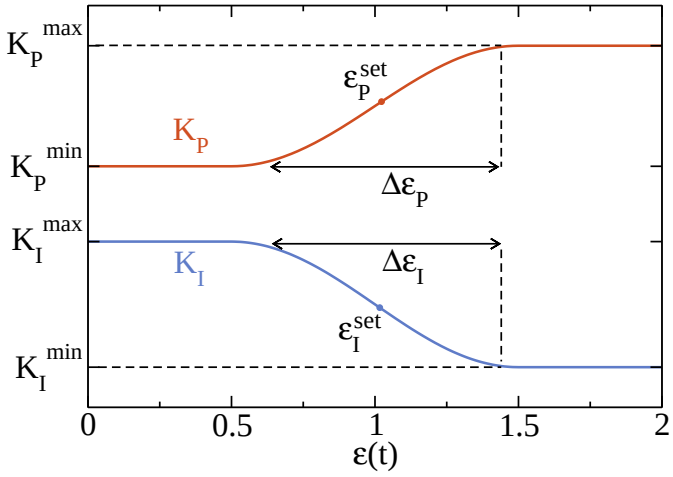

Figure 5.6: Example for transfer functions for K_I and K_P as a function of $\varepsilon(\vec{r}_{\mathrm{fp}}, t)$. $\Delta\varepsilon_{I,P}$ and $\varepsilon_{I,P}^{\mathrm{set}}$ define the characteristic points of the transfer functions as explained in the text. The antagonistic behavior of the two coefficients prevents an overshoot by minimizing the accumulated error in the beginning and by damping the proportional term once the set point is reached.

However, an optimal controller performance is always coupled to the precision of the tissue property determination. In clinical applications, experimental calibrations using test sonications are not feasible and as a result, empirically determined coefficients will be used for different experiments. As shown in sect. 5.1.3, the knowledge of α/α_s can be used to improve the performance of the PID controller and to achieve a faster convergence

$$K_P^{\max} = \frac{\alpha_s}{\alpha} K_P^{\min} \tag{5.46}$$

For the case, where the absorption coefficient is known with high precision ($\alpha_s/\alpha \to 1$), we will find the intuitive behavior $K_P^{\max} \to K_P^{\min}$. To ensure patient safety, overshoots have to be avoided at all cost and as a result the absorption coefficient will preferably be chosen too high ($\alpha/\alpha_s < 1$). This would in practice lead to a slower convergence of the temperature to the set point. Dynamic adaptation of K_P as a function of $\varepsilon(t)$ allows to circumvent this. Hence, for large control errors $\varepsilon(t)$, the maximal possible proportional gain should be applied. As soon as the control error drops below the threshold defined by the measurement noise $\Delta T_{\mathrm{noise}}$, the proportional gain has to be reduced to prevent a possible overshoot and oscillations around the set point. At this point, the previously determined optimal proportional gain from equation (5.45), based on a conservative estimation of α, can be chosen. Following these considerations, a function $K_P(\varepsilon)$ can be defined which continuously adapts the proportional gain K_P as a function of the control error $\varepsilon(t)$ (Fig. 5.6). In order to assure differentiability of $K_P(\varepsilon)$ for all $\varepsilon(t)$ the following

sine function was chosen

$$K_P(\varepsilon) = \begin{cases} K_P^{\min} & , \ \varepsilon < \varepsilon_P^{\text{set}} - \Delta\varepsilon_P/2 \\ K_P^{\max} & , \ \varepsilon > \varepsilon_P^{\text{set}} + \Delta\varepsilon_P/2 \\ f_P(\varepsilon) & , \ \text{elsewhere} \end{cases} \tag{5.47}$$

with

$$f_P(\varepsilon) = K_P^{\min} + \left[0.5 \sin\left(2\pi + \pi(\varepsilon - \varepsilon_P^{\text{set}})/\Delta\varepsilon_P\right) + 0.5\right] \left(K_P^{\max} - K_P^{\min}\right) \quad .$$

$K_P(\varepsilon)$ is characterized by two parameters which have been chosen as follows

$$\begin{aligned} \varepsilon_P^{\text{set}} &= 2\Delta T_{\text{noise}} \\ \Delta\varepsilon_P &= 2\Delta T_{\text{noise}} \quad , \end{aligned} \tag{5.48}$$

where $\Delta\varepsilon_P$ represents the transfer length ensuring a smooth transition between the two control regimes.

Integral gain

The definition of the function $K_I(\varepsilon)$ for the integral gain follows a similar argumentation. For large values of $\varepsilon(t)$, the integral part accumulates an error which later leads to an inverted integral action of the same amplitude (Fig 5.5). In a symmetrical system (tissue cooling and heating are equally possible) this will be partially compensated by the proportional part and can correct for long term error effects. However, in the scenario described here, where tissue cooling is only accomplished by diffusion and perfusion effects, the integral action can cause an undesired overshoot. For this reason, the integral gain is set to zero (or a very small value) for large control errors $\varepsilon(t)$ and increased as $\varepsilon(t)$ approaches the measurement noise of the temperature (Fig. 5.6). The maximal value for the integral gain is given by the stability criterion in (5.41) for $K_D = 1\,\text{s}$

$$K_I^{\max} = \frac{\alpha}{\alpha_s} \frac{\left(K_P^{\min}\right)^2}{4K_D} \quad . \tag{5.49}$$

However, for the preliminary experiments presented in this work, a simplified relationship for K_I was used leading to $K_I^{\max} = \left(K_P^{\min}\right)^2 / 4K_D$ based on eq. (5.38). The function $K_I(\varepsilon)$ is thus chosen antagonistic to $K_P(\varepsilon)$

$$K_I(\varepsilon) = \begin{cases} K_I^{\max} & , \ \varepsilon < \varepsilon_I^{\text{set}} - \Delta\varepsilon_I/2 \\ K_I^{\min} & , \ \varepsilon > \varepsilon_I^{\text{set}} + \Delta\varepsilon_I/2 \\ f_I(\varepsilon) & , \ \text{elsewhere} \end{cases} \tag{5.50}$$

with

$$f_I(\varepsilon) = K_I^{\min} + \left[1 - 0.5 \sin\left(\pi(\varepsilon - \varepsilon_I^{\text{set}})/\Delta\varepsilon_I\right) - 0.5\right] \left(K_I^{\max} - K_I^{\min}\right) \quad .$$

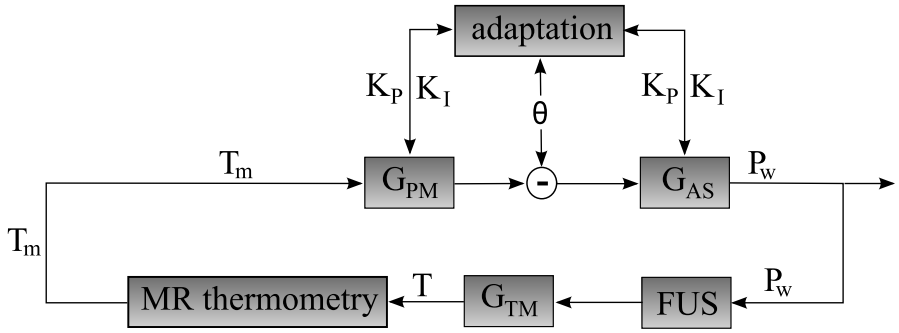

Figure 5.7: Diagram of the adaptive PID control feedback loop. The current tissue temperature is determined by means of MR thermometry. The resulting value T_m is treated by the transfer function G_{PM} (eq. (5.30)) including prediction of heat evacuation in the tissue. The difference with the target temperature θ gives the output P_w which is modified by a model of the tissue absorption represented by G_{AS} (eq. 5.31)). The output power is forwarded to the focused ultrasound device (FUS). Heating in tissue is described by the transfer function G_{TM} (eq. (5.27)) resulting in the tissue temperature T.

The characteristic points for $K_I(\varepsilon)$ have been chosen as follows

$$\begin{aligned} \varepsilon_I^{\text{set}} &= 2\Delta T_{\text{noise}} \\ \Delta\varepsilon_I &= 2\Delta T_{\text{noise}} \end{aligned} \tag{5.51}$$

to prevent oscillations while approaching the target temperature under the influence of measurement noise.

A schematic overview of the resulting adaptive controller is displayed in Fig. 5.7.

5.3 Evaluation of the adaptive PID controller

The performance of the proposed adaptive PID controller was evaluated using simulations of the HTE in tissue as well as US heating experiments on a gel phantom.

5.3.1 Simulations

All simulations were carried out using an in-house developed simulation program written in IDL (RSI, Boulder, CO, USA) and C++. The temperature evolution in the tissue was simulated using the numerical solution of the heat transfer equation (2.4) neglecting perfusion and assuming constant tissue coefficients α_{sim} and D_{sim}

$$\frac{\partial T(\vec{r},t)}{\partial t} = D_{\text{sim}}\vec{\nabla}^2 T(\vec{r},t) + \alpha_{\text{sim}} I(\vec{r}) P_w(t) \quad . \tag{5.52}$$

In order to investigate the system's response to erroneous input parameters, different values for α_{PID} and D_{PID}, the tissue coefficients used in the PID controller, were chosen.

If not stated otherwise $D_{\text{sim}} = 0.14\,\text{mm}^2\text{s}^{-1}$ and $\alpha_{\text{sim}} = 0.06\,\text{K}\,\text{J}^{-1}$ were used for the temperature simulations, while $D_{\text{PID}} = 0.07\,\text{mm}^2\text{s}^{-1}$, $0.14\,\text{mm}^2\text{s}^{-1}$, $0.28\,\text{mm}^2\text{s}^{-1}$ and $\alpha_{\text{PID}} = 0.03\,\text{K}\,\text{J}^{-1}$, $0.06\,\text{K}\,\text{J}^{-1}$, $0.12\,\text{K}\,\text{J}^{-1}$ were chosen as input parameters for the PID controller. The acoustic power field of the transducer was approximated by a 3D Gaussian profile with half widths equal to the focal point dimensions of the single element HIFU transducer described in the experimental section ($\Delta x = 0.7\,\text{mm}$, $\Delta y = 0.7\,\text{mm}$, $\Delta z = 2.8\,\text{mm}$). For the spatial resolution used, the deviation from the true focal point profile is negligible. For demonstration purposes, only a single point sonication was examined, even though the simulation program as well as the PID feedback loop were designed to control a trajectory containing several sonication points. All simulations were carried out using the following controller gains where K_P and K_I have been chosen according to equations (5.41) and (5.45) based on the used sampling time $\Delta t = 1.3\,\text{s}$ and an assumed uncertainty of the absorption coefficient $\alpha/\alpha_s = 0.5$.

$$\begin{aligned} &\text{static PID:} && K_P = 0.77, \quad K_I = 0.145\,\text{s}^{-1} \\ &\text{adaptive PID:} && K_P^{\min} = 0.77, \quad K_P^{\max} = 1.54, \\ & && K_I^{\min} = 0.0\,\text{s}^{-1}, \quad K_I^{\max} = 0.145\,\text{s}^{-1} \end{aligned}$$

Furthermore, a step function with a temperature change of 6 °C was chosen as target temperature profile and Gaussian noise with a standard deviation of 0.3 °C was added to the simulated temperature data to reproduce experimental conditions. Consequently, a value of $\Delta T_{\text{noise}} = 0.3\,^\circ\text{C}$ was chosen in all simulations for the determination of the transfer function. For tissue coefficients of $D = 0.14\,\text{mm}^2\text{s}^{-1}$ and $\alpha = 0.06\,\text{K}\,\text{J}^{-1}$ the temperature evolution was simulated on a grid of $245 \times 245 \times 60$ voxels with a spatial resolution of $0.25 \times 0.25 \times 1.00\,\text{mm}^3$ and a temporal resolution of 1.3 s. As a next step, the acquired temperature values were averaged over volumes of $1.75 \times 1.75 \times 5.00\,\text{mm}^3$ to represent the measurements acquired with MR thermometry.

Fig. 5.8 shows the simulated temperature profile for the conventional (blue dashed-dotted line) and the adaptive PID controller (red dashed line) including the target temperature profile (black solid line) for simulations with varying values for the diffusion and the absorption coefficient. The conventional PID controller produced overshoots of 0.3 °C to 2.2 °C for all parameter combinations with the effect being especially pronounced for an overestimation of the diffusion coefficient and an underestimation of the absorption coefficient as already stated by [22]. In the case of the adaptive algorithm, an overshoot of up to 0.5 °C occurred for an overestimation of the diffusion coefficient in combination with an underestimation of the absorption coefficient and was substantially reduced compared to the conventional PID.

5.3.2 Phantom experiments

All experiments in this chapter were performed on a 1.5 T Achieva MR-scanner (Philips Medical Systems, Best, the Netherlands). A single element ultrasound transducer (focal length = 8 cm, aperture = 12 cm, operating frequency = 1.5 MHz) was integrated in the MR patient bed. All parts were MR compatible. The generator (AG 1006 Series

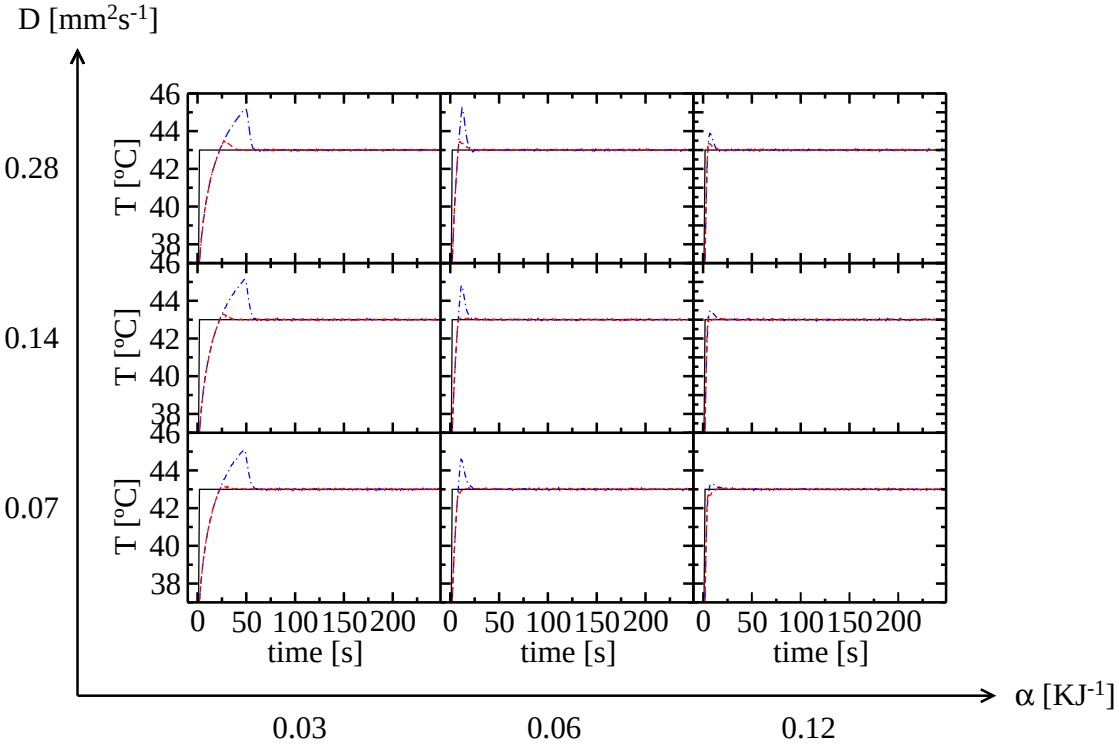

Figure 5.8: Comparison of the responses of the adaptive and the conventional PID controller to a step target temperature function ($\Delta T = 6\,^{\circ}$C, black solid line). The resulting temperatures are shown for different values of the diffusion coefficient ($D_{\mathrm{PID}} = 0.7\times10^{-7}\,\mathrm{m^2s^{-1}}$, $1.4\times10^{-7}\,\mathrm{m^2s^{-1}}$, $2.8\times10^{-7}\,\mathrm{m^2s^{-1}}$) and the absorption coefficient ($\alpha_{\mathrm{PID}} = 0.03\,\mathrm{K\,J^{-1}}$, $0.06\,\mathrm{K\,J^{-1}}$, $0.12\,\mathrm{K\,J^{-1}}$) where the "true" tissue parameters were held fixed at $D_{\mathrm{sim}} = 1.4\times10^{-7}\,\mathrm{m^2s^{-1}}$ and $\alpha_{\mathrm{sim}} = 0.06\,\mathrm{K\,J^{-1}}$. While the conventional PID controller (blue dotted-dashed line) always produced an overshoot, the adaptive controller (red dashed line) only showed a significantly reduced overshoot for an overestimation of the diffusion coefficient. Note that the shown temperature values were averaged over 50 simulations.

Amplifier, T & C Power Conversion Inc., Rochester, NY, USA) and power supply were installed outside the scanner room. All feed lines were isolated and filtered in order to prevent interferences with the radio-frequency of the MR scanner. An agarose-silicon gel (2 % agarose, 3 % silicon) was centered on the transducer and a 15-cm-diameter surface coil was used for signal registration (Fig. 5.9a). In the beginnings, several short test shots with constant power were applied to exactly locate and center the focal point. For PRF-thermometry a simple 2D RF-spoiled gradient recalled sequence ($T_E = 20\,$ms, $T_R = 260\,$ms, flip angle $= 35\,^{\circ}$, voxel size $= 1.72\times1.72\times5\,\mathrm{mm^3}$, 5 slices) was used delivering an image stack every 6.3 s. The reconstructed phase and magnitude images were streamed to an in-house developed user interface (RealTI software, RTech, Bordeaux, France) which performed temperature calculations online (Fig. 5.9b). Once the focal point position was determined, the slice number was decreased to one to achieve a higher temporal resolution ($\Delta t = 1.3\,$s). With the new parameters, another test shot

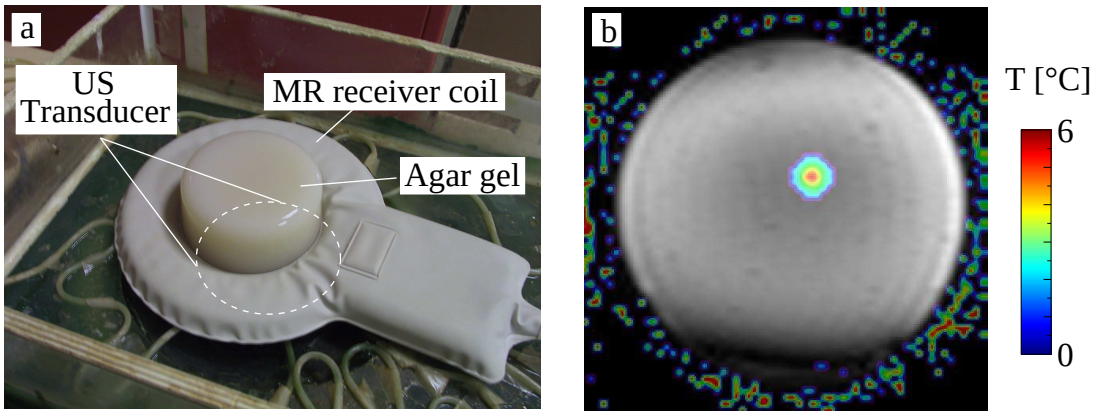

Figure 5.9: a: Experimental setup: The agar gel was placed on the ultrasound transducer integrated in the MR patient bed and a surface coil was placed around the gel for signal registration. b: Magnitude image of the gel with an overlay of the calculated temperature map during ultrasound heating.

with a constant transducer power of 30 W was applied to monitor the heating and cooling process. The acquired temperature values were used to determine the apparent absorption $\alpha_{\text{app}} = 0.06\,\text{K J}^{-1}$ and diffusion coefficient $D = 0.14\,\text{mm}^2\text{s}^{-1}$ of the phantom [25]. To evaluate the performance of the proposed controller algorithm, the controller gains were determined as described before, leading to values of $K_P = K_P^{\min} = 0.77$, $K_I = K_P^2/(4K_D) = 0.145\,\text{s}^{-1}$ and $K_P = K_P^{\min}/K_P^{\max} = 0.77/1.54$, $K_I = 0.0/0.145\,\text{s}^{-1}$ for the conventional PID and the adaptive controller respectively. The uncertainty in the determination of the absorption coefficient was chosen as $\alpha/\alpha_s = 0.5$. For comparison, a PID controller with increased controller gains of $K_P = 3.08$, $K_I = 2.37\,\text{s}^{-1}$ was evaluated. The experiments were carried out for two different temperature noise levels by adapting the flip angle of the sequence. For flip angles of 1° and 35° temporal temperature standard deviations of 0.2 °C and 0.8 °C were measured. The performance of the different PID types was first evaluated for a simple step function as target temperature profile with a temperature change of 6 °C, and in a second experimental part for a more complex target temperature profile including 3 step functions with temperature changes of 6 °C, 4 °C and −4 °C. Figure 5.10 shows the measured and the desired target temperature for a heating experiment with a step function of 6 °C as target temperature profile. It is visible that the adaptive controller gradually approached the target temperature while the two conventional PID's produced overshoots of 3.6 °C and 1.6 °C respectively. As a result of the smoother approach to the target temperature, the adaptive PID took two measurement updates longer in order to reach the set point. After initial oscillations, the adaptive PID established a stable temperature within 24.7 s while the optimized PID took 27.3 s. Once the plateau was reached, the optimized conventional (column one) and the adaptive PID showed a comparable temporal standard deviation of the error $\varepsilon(t)$ of 0.16 °C while the PID with increased controller gains (column three) was not able

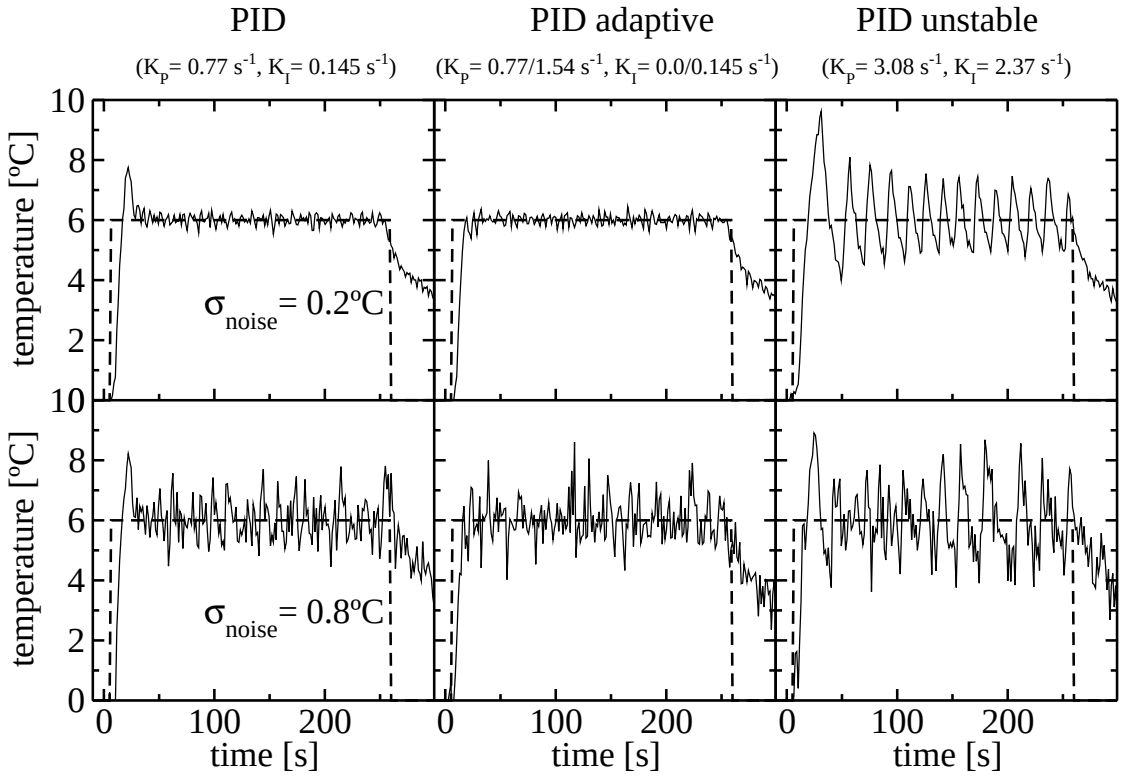

Figure 5.10: Comparison of the measured (solid line) and the target temperature (dashed line) for the conventional PID controller with controller gains calculated on the basis of the temporal resolution of the measurement (first column), the adaptive controller (second column) and the PID controller with increased controller gains in order to demonstrate instability (third column). For better visibility, the scale for the unstable PID was changed as indicated on the right hand side of the graphs. The first row shows the results for a temporal temperature standard deviation of 0.2 °C, whereas the second row presents the results for an increased temperature standard deviation of 0.8 °C. All experiments were performed with a temporal resolution of $\Delta t = 1.3$ s.

to accomplish a stable temperature, but oscillated around the target temperature with amplitudes up to 2 °C and a mean period of 16.5 s. A closer look at the controller components and the applied power during the experiments (Fig. 5.11) reveals the advantages of an adaptive PID control. Due to the high maximal proportional gain of the adaptive controller, a fast increase with maximum power has been be achieved in the beginning. As a result, the proportional term only showed a short pronounced peak, which decayed rapidly after the target temperature was reached. In the initial phase, the integral term remained comparably small without developing a peak as pronounced as for the conventional PID controller. After having reached the target temperature, the conventional PID with the optimized proportional gain exceeded the target temperature due to the accumulated integral error.

When confronted with a more complicated target temperature profile consisting of 3 step functions (Fig. 5.12), the adaptive PID stayed very close to the target temperature

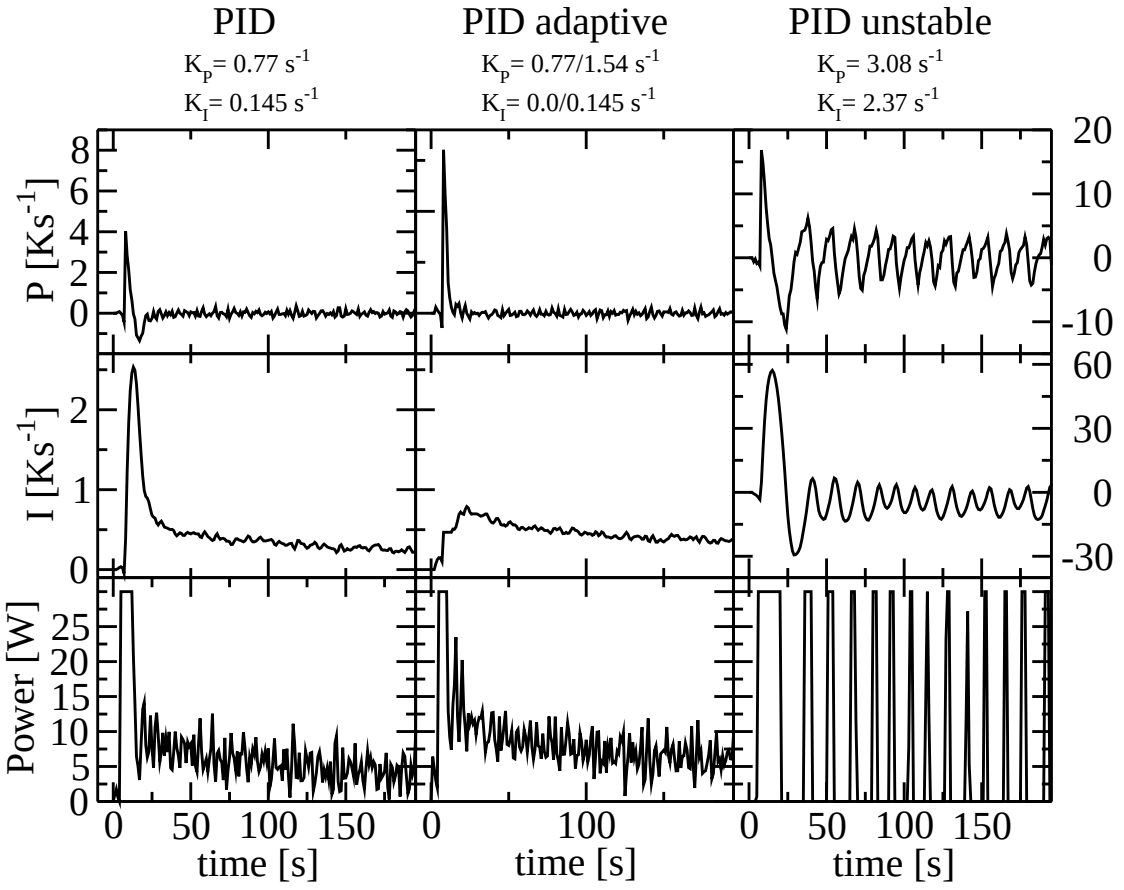

Figure 5.11: Proportional term $K_P(t)P(t)$ (first row), integral term $K_I(t)I(t)$ (second row) and transducer power $P_w(t)$ as calculated by the PID with controller gains calculated on the basis of the temporal resolution of the measurement (first column), the adaptive controller (second column) and the PID with increased controller gains (third column). The experiments were performed with a temporal resolution of $\Delta t = 1.3\,\mathrm{s}$ and a temperature standard deviation of $0.2\,^{\circ}\mathrm{C}$.

with errors of $0.16\,^{\circ}\mathrm{C}$ except for the cases where practical limitations like the maximal transducer power or the delay during the cooling process prevented a better performance. As for the simple step target temperature profile, the conventional PID with optimized controller gains produced overshoots of $2\,^{\circ}\mathrm{C}$ and $1.6\,^{\circ}\mathrm{C}$, and an undershoot of $-1.6\,^{\circ}\mathrm{C}$ every time the target temperature was changed suddenly.

5.4 Discussion

Typical application scenarios for retroactive temperature control are in the emerging fields of non-invasive tumor ablation and localized activation of pharmacological carriers for targeted chemo therapy.

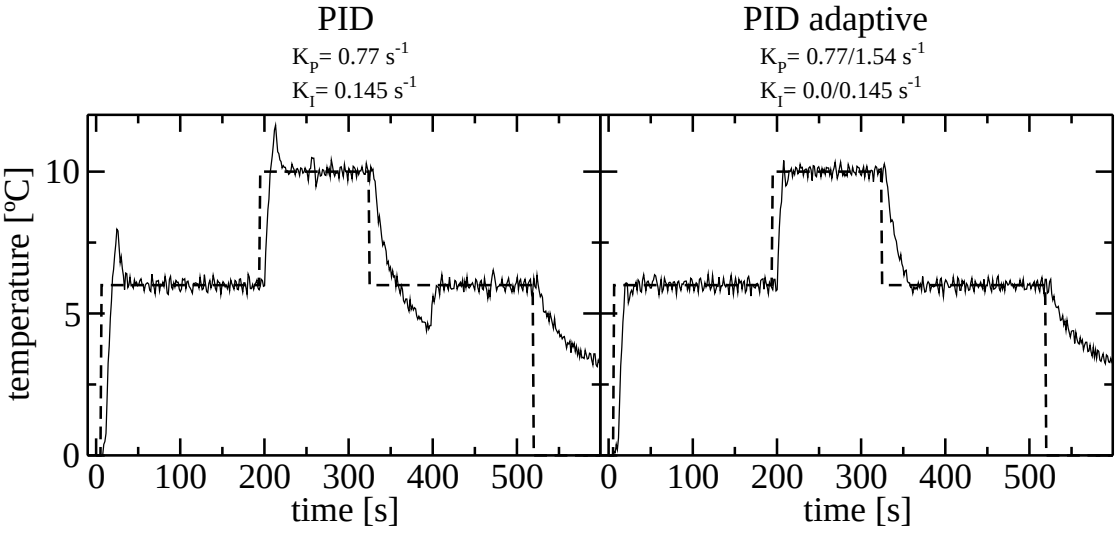

Figure 5.12: Comparison of the measured (solid line) and the target temperature (dashed line) for the PID controller with controller gains calculated on the basis of the temporal resolution of the measurement (first column) and adaptive controller (third column) for a 3-step target temperature profile. All experiments were performed with a temporal resolution of $\Delta t = 1.3\,\mathrm{s}$ and a temperature standard deviation of $0.3\,^{\circ}\mathrm{C}$.

For temperature control during tumor ablation, the controller method has to ensure a sufficient temperature rise in order to achieve a lethal thermal dose (generally 240 EM [26]) in the targeted area. On the other hand, patient safety has to be assured at any time by avoiding damage to adjacent healthy tissue, and by minimizing the treatment time to prevent undesired heat deposition in subcutaneous tissue. This is further complicated by the limited knowledge of the thermal properties of the target tissue. In most cases, the absorption and diffusion coefficients are not precisely known in the entire target area and are likely to change during the intervention due to tissue coagulation. As a result, the tissue parameters for the PID controller are generally chosen conservatively, i.e. the absorption coefficient is preferably overestimated and the diffusion coefficient underestimated, leading to a slow convergence to the target temperature and prolonged interventions. The proposed PID allows to mediate these effects by permitting the choice of more "aggressive" controller gains without the risk of over-control. Despite this, the convergence time to the set point and the robustness against measurement noise are comparable to an optimized conventional PID under ideal conditions.
Contrary to the use of such algorithms for tumor ablation, temperature control during localized activation of pharmacological carriers or gene activation has to fulfill different requirements. In these cases, heat is used as an activator and not for direct tissue ablation, which is why tissue damage due to extensive heating has to be avoided at all costs. Furthermore, the temperature regulation range is limited between $37\,^{\circ}\mathrm{C}$ and $44\,^{\circ}\mathrm{C}$ leading to the requirement of a high precision temperature control. Considering the non-linear behavior of the thermal dose [27], this becomes even more crucial for

prolonged interventions, where long-term accumulation of energy and thus a lethal effect on the tissue has to be avoided. As an example, a stable temperature of 44 °C maintained over a period of 120 s, leads to a thermal dose accumulation of 1.7 % of the lethal thermal dose in human tissue, while the same duration at a temperature of 48 °C already leads to an increase by a factor of 16, namely 26.7 % of the lethal thermal dose. The proposed adaptive integral control has been designed to address the requirements of non-symmetric systems, where the amount of heating can be actively influenced by the controller, whereas heat evacuation is determined by fixed tissue parameters such as perfusion and diffusion. As a result, overshoots are avoided, while a rapid and stable convergence towards the desired target temperature is maintained. Similar to the case of retroactive temperature control during tumor ablations, the absorption and diffusion coefficient are a priori not precisely known. What is more, the determination of the thermal tissue coefficients by applying a test shot is not accessible since this would trigger the activation process.

The analysis of the closed-loop transfer function allowed the description of the PID controller even in a modified form including the heat transfer equation. Stability criteria derived from this analysis were successfully integrated into the concept of the adaptive PID controller and achieved robust temperature control as predicted by the theoretical model.

The presented approach did not take into account the latencies resulting from the acquisition process, data transport and computation time. As this could be a source of instabilities, future work should explore these effects more closely and incorporate them into an extended controller algorithm. The Laplace representation of the modified PID used an approximation of the actual heat evacuation terms represented by diffusion and perfusion in the HTE. Hence, small deviations in the response of the controller are to be expected depending on the diffusion coefficient of the heated tissue. Finally, the assumption of a spatially constant diffusion coefficient used in the simulations and the theoretical description of the HTE may not hold for all applications, i.e. in breast tissue (water/fat interfaces). However, in the case of heterogeneous diffusion coefficients in the target area, a test shot would deliver an averaged value which reflects the observed diffusion behavior in the control point. What is more, small deviations from the “true” diffusion coefficient can be compensated by the integral term of the controller.

6 Volumetric temperature control on moving targets [28, 29]

6.1 Volumetric control strategies

As treatment volumes are generally larger than the focal point size, strategies for volumetric sonications are required. For this purpose, different sonication patterns have been proposed in the past (Fig. 6.1). In the beginnings, a single element transducer was displaced mechanically [22], which was slow and could cause magnetic field variations. Starting with the use of multiple single element transducers [30, 31], recent developments allow efficient volume heating and shorter treatment times. For prostate tumors, which are directly accessible with transurethral ultrasound transducers, efficient volume ablation strategies have been developed. Using planar or multi-sectored tubular ultrasound transducers, cylindrical volumes were heated successfully [15, 32, 33]. Recently, this method has also been applied to interstitial ultrasound ablations in the liver [34]. The emergence of phased-array transducers allowing the electronic displacement of the focal point offers new perspectives. This is because the available short positioning times as compared to the acquisition time of an MR-thermometry image enable the treatment of several points between successive images. Still, the optimization of this trajectory in terms of positioning and applied power remains challenging. Furthermore, the associated longer treatment times and higher power levels lead to increased heating in the near-field. Thus, it is desirable to keep the treatment time as short as possible and to minimize the applied power. As a result, it was proposed to monitor the temperature rise in the near-field by placing an additional image slice in the respective area [35, 36].

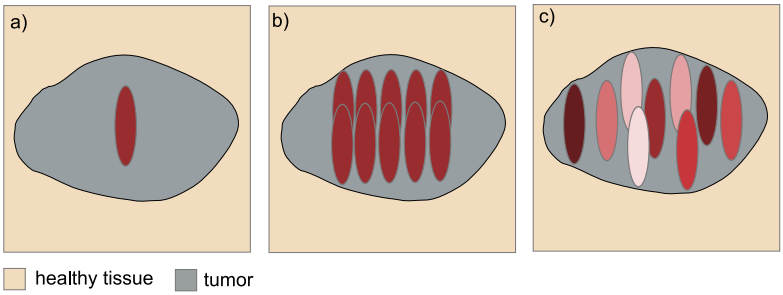

Figure 6.1: Volumetric control strategies: a) single point sonication, b) mechanical displacement of a single sonication point following a pre-defined trajectory, c) adaptive electronic displacement of the focal point position. The different colors of the focal points indicate that the power is adapted during the trajectory optimization.

One possible implementation of such a temperature control strategy relies on a trajectory consisting of multiple outward-moving circles combined with a binary control algorithm which switches to the next sub-circle as soon as a certain target temperature/thermal dose has been reached [35, 36]. As a result, the procedure can be adapted accordingly and the used algorithm does not require any knowledge about the thermal properties of the tissue. However, the heating is limited to circular shaped volumes and the number of acquired slices necessary for sufficient volume coverage leads to a comparable low temporal resolution. Another approach optimizes the position of the trajectory points together with the applied power using a PID controller in order to achieve a predefined spatial target temperature distribution [12].
While the methods presented above are generally based on temperature control, the on-line assessment of the thermal dose [27] has been suggested to determine the therapy endpoint [37]. Monitoring the thermal dose of the treated tissue to ensure a complete destruction of the tumor tissue has already been applied in a feedback algorithm controlling a fixed single-element ultrasound transducer [38]. For this work, the method proposed by Mougenot et al. [12] was further developed to include thermal dose control using a proportional controller. The combination with a 2D motion correction technique [39–41] allows for an effective destruction of the target tissue with minimal energy, time and damage outside the target area in the presence of physiological motion. In order to ensure sufficient volume coverage while maintaining a high temporal resolution, the acquisition of a static image slice for 2D motion estimation was combined with a sweep of a second slice covering the target area. The feasibility of the proposed method was tested experimentally ex vivo under conditions simulating respiratory motion of abdominal organs.

6.2 Implementation

6.2.1 Slice sweep

In order to achieve both sufficient volume coverage and a high image frame rate, which is crucial for precise 2D motion correction and ultrasound beam steering, the acquisition of a static image slice was combined with a slice sweep. For this purpose, one slice was translated by Δs for every image acquisition, thus covering a total range of $S_z = n\Delta s$ in the slice encoding direction for a slice sweep comprising n slice positions (Fig. 6.2). While the static slice was updated for every image acquisition and served for 2D motion estimation, an update of the entire image volume took nt_{dyn} where t_{dyn} is the dynamic scan time of the acquisition. In general, arbitrary displacement schemes are possible, allowing for example to oversample a certain spatial position. For the implementation presented here, however, the slice was continuously translated from $-S_z/2$ to $S_z/2$ with $\Delta s = \Delta z$.

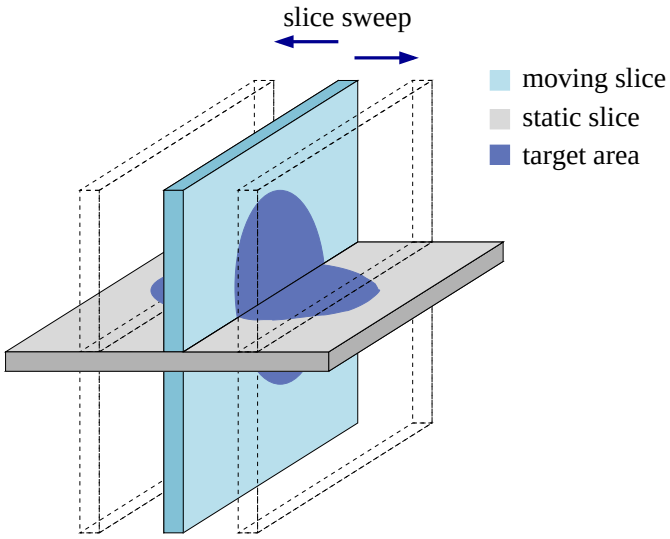

Figure 6.2: Principle of the slice sweep to increase the volume coverage. While one slice remains static, the second slice is moving continuously to cover the whole target area.

6.2.2 2D motion compensation and beam steering

In order to accurately perform MR-guided HIFU heating on moving objects, two conditions have to be fulfilled. Firstly, the accurate estimation of the thermal dose in the heated tissue requires an exact spatial correlation of the respective voxels in time. For this reason, 2D in-plane motion has to be estimated and compensated. This is achieved by estimating the in-plane displacements with respect to a reference image using a gauss-newton algorithm. The retrieved motion coefficients are then used to register the acquired images to the common reference position. Secondly, volumetric heating requires to sustain high power levels for a longer period of time to achieve necrosis, especially in highly-perfused organs like the kidney. Physiological motion would lead to a distribution of the applied thermal energy over a larger volume and as a result reduce the achievable temperature rise. For this reason, the focal point position has to be adapted in real-time. Similar to the motion estimation carried out for image registration, the acquired static slice is used to estimate the motion of the image stack with respect to the static focal point. A more detailed explanation of the concept and implementation of 2D motion compensation and beam steering can be found in [42, 43].

6.2.3 Trajectory optimization

Depending on the pre-defined target volume, a sub-grid of the actual imaging volume, containing the chosen target area, is selected (Fig. 6.3a). For every update of the temperature/thermal dose distribution, the difference from the desired target temperature T_T or thermal dose TD_T is calculated. Then, the thermal energy to be applied E_{th} is

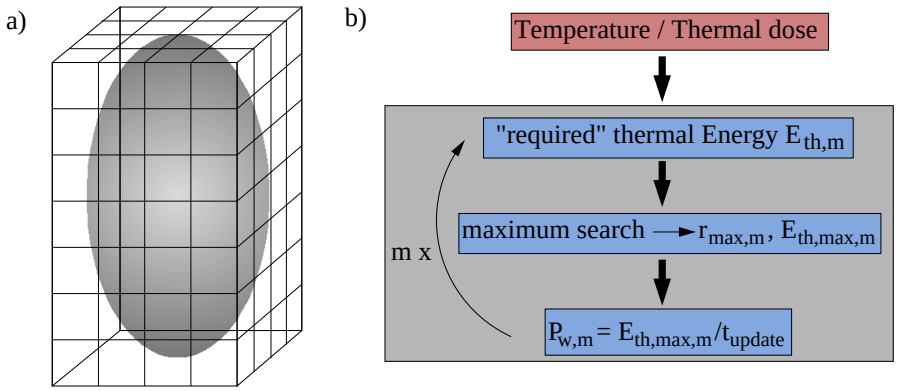

Figure 6.3: a) Choice of the sub-grid for the trajectory optimization depending on the shape of the target area (here for an ellipsoidal shape). b) Scheme of the trajectory optimization algorithm.

calculated from the temperature difference.

$$E_{\mathrm{th}} = \frac{\Delta T}{\alpha} \quad , \tag{6.1}$$

where α denotes the absorption coefficient of the tissue and ΔT is calculated as follows

$$\begin{aligned} \text{T control:} \quad \Delta T &= T_T - T \\ \text{TD control:} \quad \Delta T &= T_L - T_{\mathrm{ref}} - T \\ &- \log\left(\frac{2(\mathrm{TD}_T - \mathrm{TD})}{t_{\mathrm{dyn}}} - \mathrm{R}_1^{(T_L - T_{\mathrm{ref}} - T)}\right) / \log \mathrm{R}_2 \end{aligned} \tag{6.2}$$

with $T_L = 43\,^{\circ}\mathrm{C}$ being the threshold temperature and T_{ref} the reference temperature (body temperature) for the thermal dose calculation and

$$\begin{cases} \mathrm{R}_1 = \mathrm{R}_2 = 0.25 & , T(t) \leq T_L - T_{\mathrm{ref}} - \Delta T_{\max} \\ \mathrm{R}_1 = \mathrm{R}_2 = 0.5 & , T(t) \geq T_L - T_{\mathrm{ref}} \\ \mathrm{R}_1 = 0.25, \mathrm{R}_2 = 0.5 & , T_L - T_{\mathrm{ref}} - \Delta T_{\max} < T(t) < T_L - T_{\mathrm{ref}} \end{cases}$$

with

$$\Delta T_{\max} = \alpha P_{w,\max}\, t_{\mathrm{update}} \quad .$$

Here, $P_{w,\max}$ defines the maximal power to be applied and t_{update} represents the minimal delay between two successive trajectory points due to hardware restrictions. With this, an iterative optimization prodecure is started. In a first step, a maximum search on all voxels included in the selected sub-grid delivers the point $r_{\max,0}$, where $E_{\mathrm{th},0}$ is maximal. Consequently, $r_{\max,0}$ is chosen as the next sonication point and the power to be applied is calculated according to $P_w = E_{\mathrm{th},0}(r_{\max,0}) t_{\mathrm{update}}$. As in general, $t_{\mathrm{update}} \ll t_{\mathrm{dyn}}$, the dynamic scan time of the image acquisition, several sonications can be carried out between two image acquisitions. In order to 'simulate' the sonication process, a thermal

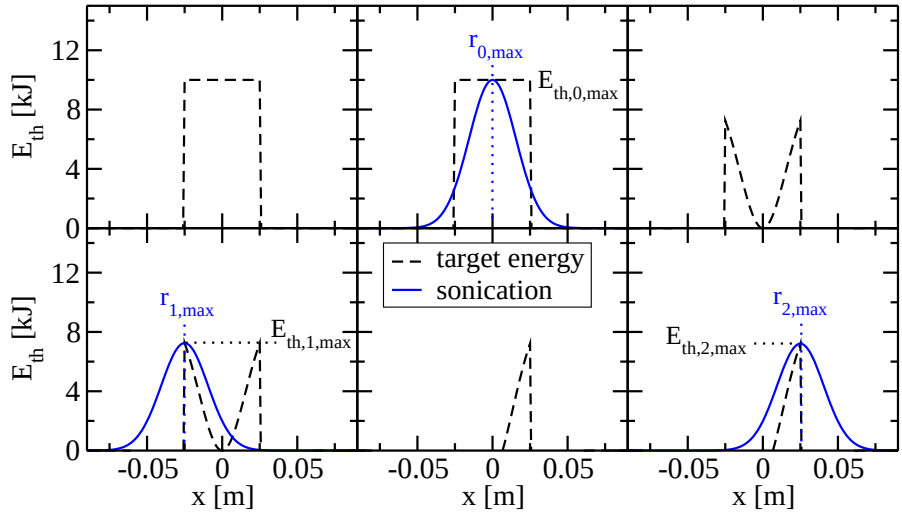

Figure 6.4: Optimization of the sonication coordinates based on the required thermal energy E_{th}.

energy profile resulting from the sonication at the chosen position, which is approximated by a 3D gaussian, is subtracted from the previously calculated distribution of $E_{\mathrm{th},0}$ yielding $E_{\mathrm{th},1}$. In the next iteration step, the maximum search delivers again the voxel position with maximal $E_{\mathrm{th},1}$ and the point is chosen for sonication. This procedure is repeated m times until either $E_{\mathrm{th},m} = 0$ everywhere in the target area or $m\ t_{\mathrm{update}} \geq t_{\mathrm{dyn}}$. A more detailed explanation of this optimization procedure is given in [12] and is displayed schematically in Fig. 6.3b. The difference between the true focal point profile and a gaussian profile is below 1.3 % for an in-plane resolution of 2.4 mm^2 and maximal 11.0 % for a spatial resolution of 0.4 mm^2 (Fig. 6.5). That is why, for the spatial resolutions generally used in MR thermometry, the error in approximating the focal point profile by a 3D gaussian with adapted size is negligible.

6.2.4 Trajectory weighting

In addition to the optimization process described above, an additional weighting factor $w(r, z)$ is introduced in order to account for the different control strategies and the ultrasound attenuation in the tissue

$$w(r, z) = w_{\mathrm{perp}}(r) w_{\mathrm{par}}(z) \quad , \tag{6.3}$$

where $w_{\mathrm{perp}}(r)$ and $w_{\mathrm{par}}(r)$ denote the weighting factors perpendicular and parallel to the beam axis as a function of the radial distance r and the distance from the transducer surface z.

Temperature control Temperature control can be used for two purposes. Either, the objective is to achieve a homogeneous small temperature elevation within a certain target

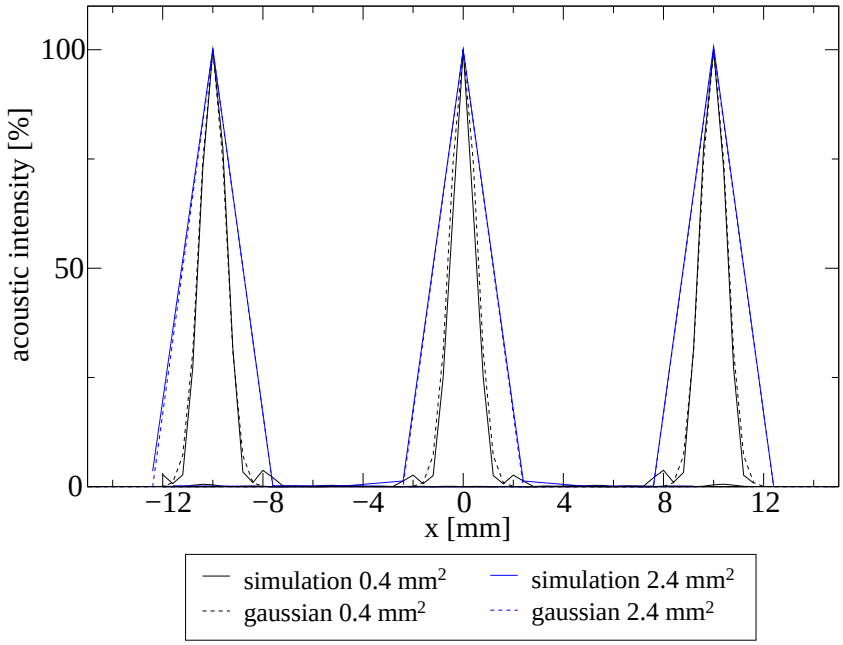

Figure 6.5: Difference between the focal point profile derived from the numerical solution of the Rayleigh integral and a gaussian. The 1D profile in x is shown for a spatial resolution of $0.4\,\mathrm{mm}^2$ (black) and $2.4\,\mathrm{mm}^2$ (blue) for the focal point in its natural position and displaced electronically by $\Delta x = \pm 1\,\mathrm{cm}$.

volume in order to trigger the release of anti carcinogenic drugs in local drug delivery or to activate transgenes in gene expression. In this case, it is essential to precisely control the temperature in the target area in order to avoid the application of a lethal thermal dose. In a second application scenario, temperature control can be used for thermo-ablation with the aim to maintain a certain temperature level over a pre-determined duration in order to apply a pre-defined thermal dose following equation 1.23. For both cases, different weightings can be applied in order to meet the specific requirements. In order to achieve a homogeneous temperature distribution for the first application, an inverse radial weighting can be applied which means that points at the periphery of the target area will be heated preferably while the central points will be heated via heat diffusion (Fig. 6.6 first image) leading to a temperature change $T \leq T_T$. The resulting weighting factor $w_{\mathrm{perp}}(r)$ as a function of the radial distance r has the form

$$w_{\mathrm{perp}}(r) = \begin{cases} r/A & r > 0 \\ 0.1 & r = 0 \end{cases}, \tag{6.4}$$

where A denotes the maximal expansion of the target area perpendicular to the beam axis. The second case, is similar to thermal dose control and will be discussed below.

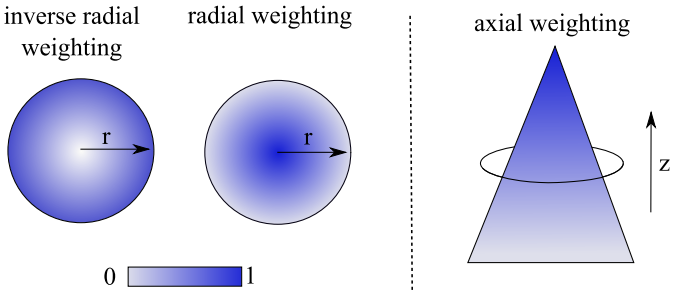

Figure 6.6: Left: Weighting perpendicular to the beam axis for the two different control strategies. For precise temperature control, the voxels situated at the border of the target area are preferred to those in the center leading to an inverse radial weighting. For thermal dose and temperature for ablation on the other hand, heating starts in the center leading to a radial weighting. Right: Weighting parallel to the beam axis to compensate for attenuation effects. In order to prevent overheating in the target regions closer to the transducer surface, heating starts preferably in the most distant voxels.

Thermal dose control In the case of thermal dose control, the objective is to achieve a pre-defined, in general lethal, thermal dose in the whole target area. As surrounding tissue should be spared, heating is applied first in the center of the target area (Fig. 6.6 second image). With this technique, the central points of the target area may be over-treated, but the distribution of a thermal dose $\mathrm{TD} \geq \mathrm{TD}_T$ is assured. The resulting weighting factor $w_{\mathrm{perp}}(r)$ as a function of the radial distance r from the center of the target area has the form

$$w_{\mathrm{perp}}(r) = \begin{cases} r_0/r & r > 0 \\ 1 & r = 0 \end{cases}, \tag{6.5}$$

where r_0 was set equal to the spatial resolution of the acquisition.

Ultrasound attenuation For 3D volume control along the beam axis, the attenuation of the ultrasound in the tissue has to be taken into account. As the tissue attenuation coefficient is not exactly known, an additional weighting factor $w_{\mathrm{par}}(z)$ as a function of the distance from the transducer surface z has been introduced in order to account for these effects (Fig. 6.6 right):

$$w_{\mathrm{par}}(z) = \begin{cases} z/Z & z > 0 \\ 0.1 & z = 0 \end{cases} \tag{6.6}$$

Here Z denotes the maximal expansion of the target area parallel to the beam axis.

6.2.5 Image processing pipeline

For 2D motion compensation in combination with the described trajectory optimization, a dedicated image processing pipeline has been developed (Fig. 6.7). In order to reduce

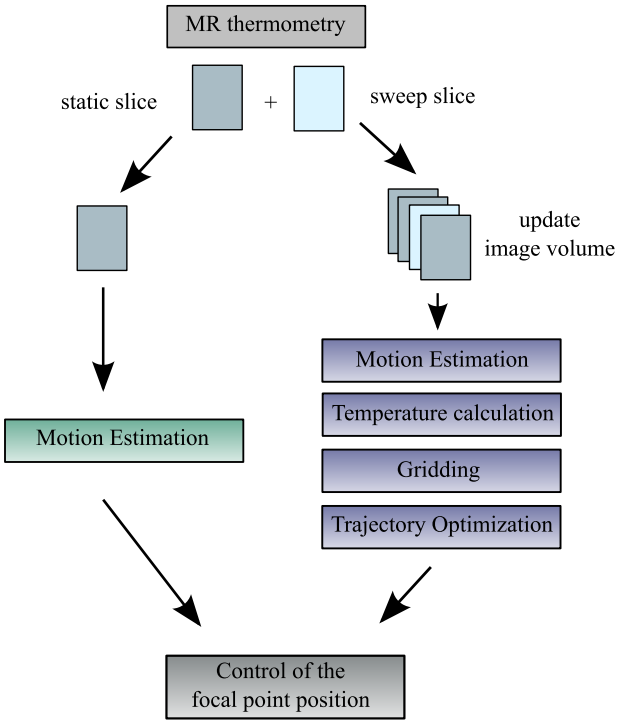

Figure 6.7: Scheme of the Data processing pipeline. The static slice is directly processed in a separate thread (left) which calculates the displacement with respect to the transducer in order to adapt the focal point position accordingly. The sweep slice on the other hand is used to calculate 3D motion compensated temperature and thermal dose maps which are then used to optimize the trajectory of sonication points.

the latency, motion estimation for the adaptation of the focal point position was carried out on the static slice only (left side in Fig. 6.7). The thus retrieved position updates were directly forwarded to a dedicated thread controlling the ultrasound transducer. In a second independent pipeline, both acquired slices were motion compensated and temperature and thermal dose were calculated using a multi-baseline phase correction as described in 1.2.3. Subsequently, the calculated 2D temperature and thermal dose maps were gridded into an imaging volume aligned with the physical axis of the ultrasound transducer. Trajectory optimization was carried out on the 3D temperature and thermal dose maps and the resulting position updates of the trajectory were forwarded to the transducer control thread. This implementation allowed the treatment of a slice sweep covering n=11 slice positions which were gridded into a 3D volume of $96 \times 96 \times 30$ with isotropic resolution of $2.5\,\mathrm{mm}^3$ within a total dynamic scan time of 140 ms for both slices.

6.3 Evaluation experiments

6.3.1 Imaging protocol

All experiments in this chapter were performed on a 1.5 T Achieva MR-scanner (Philips Healthcare, Best, the Netherlands). The Philips Sonnalleve platform containing a 256-element phased array ultrasound transducer was used for HIFU heating and the integrated multi-channel surface coil was used for signal registration. PRF MR thermometry was performed based an a RF spoiled single shot gradient recalled EPI sequence(T_R = 125 ms, T_E = 41 ms, matrix = 128 × 75, voxel size = 2.5 × 2.5 × 5 mm^3, 2 image stacks (both coronal), bandwidth in readout direction = 1561 Hz). If not stated otherwise, experiments were carried out on an agarose phantom. A trajectory of 5 sonication points was optimized and the sonication duration for each point was set to 25 ms and 60 W electronic power were applied.

2D control The volume sweep covered 5 different slice positions with a displacement of 5 mm.

3D control In order to achieve a higher volume coverage, the slice thickness was increased to 6 mm and the volume sweep was extended to cover 11 slice positions with a displacement of 6 mm.

6.3.2 Choice of control strategy

For the comparison of different control strategies for thermal ablation, three separate control experiments were carried out. The first test evaluated the achieved temperature and thermal dose distribution if a constant power of 60 W was applied continuously at the same point. In a second experiment, a circular 2D target area of 2 cm diameter comprising 49 voxels was targeted in order to achieve a homogeneous temperature elevation of $T_T = 10\,^{\circ}\mathrm{C}$ using temperature control and a maximal acoustic power of 60 W. Finally, the same target area was heated using thermal dose control with a target value

		fixed point	T control	TD control
NT	$\mathrm{TD} \geq 10^{-2}\,\mathrm{TD}_T$ [%]	14.1	34.7	33.5
	$\mathrm{TD} \geq 10^{-1}\,\mathrm{TD}_T$ [%]	4.4	9.8	11.1
	$\mathrm{TD} \geq \mathrm{TD}_T$ [%]	2.3	3.2	4.0
T	$\mathrm{TD} \geq 10^{-2}\,\mathrm{TD}_T$ [%]	95.9	100.0	100.0
	$\mathrm{TD} \geq 10^{-1}\,\mathrm{TD}_T$ [%]	79.6	100.0	100.0
	$\mathrm{TD} \geq \mathrm{TD}_T$ [%]	55.1	85.7	93.9

Table 6.1: Percentage of voxels which have received a thermal dose of (TD = $10^{-2}\,\mathrm{TD}_T$, $10^{-1}\,\mathrm{TD}_T$, TD_T = TD_T) within the target area (T, 49 voxels) and in a 3D spherical shell of 3 cm radius surrounding the target area (NT, 1988 voxels).

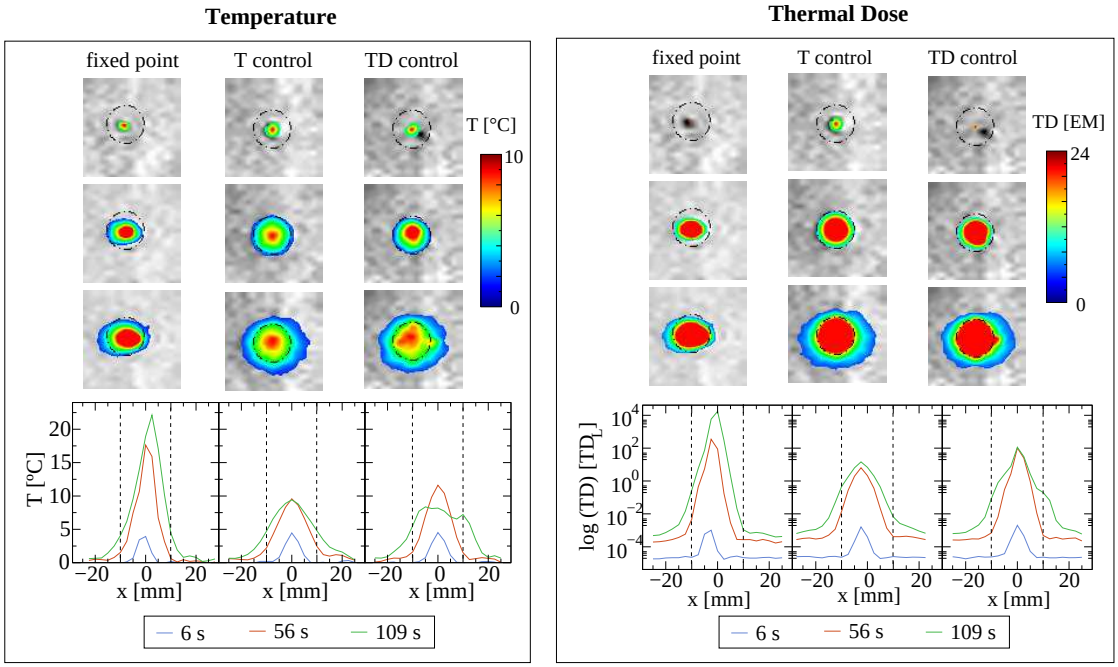

Figure 6.8: Comparison of three different control strategies: fixed point, temperature control and thermal dose control. A circle with diameter 2 cm (black dashed-dotted line) was targeted with $T_T = 10\,°\mathrm{C}$ and $\mathrm{TD}_T = 24\,\mathrm{EM}$ for temperature and thermal dose control, respectively. For the three methods, the temperature maps (left) and thermal dose maps (right) are shown for three time points. Below, the temperature and thermal dose profiles for $y = 0$, $z = 0$ are displayed for the three time points.

of $\mathrm{TD}_T = 24\,\mathrm{EM}$ and the same maximal power. Figure 6.8 shows the resulting temperature and thermal dose maps as well as profiles along $y = 0$, $z = 0$ for the three control strategies and three different time points. The final time point was chosen such that one of the control strategies had achieved its target value, in this case the thermal dose control algorithm. A comparison of the fixed point sonication and the thermal dose control shows comparable temperature and thermal dose maps and profiles for the first time point. In the course of the experiment however, it becomes visible that the single point sonication produces much higher temperature and thermal dose gradients while the thermal dose control achieves a broader temperature and thermal dose distribution with lower maximal values in the center of the target area. As a result, when the target value is achieved for the thermal dose control, the thermal dose for the fixed point sonication has not yet achieved the target value in the whole target area. The temperature control experiment aims at a pre-defined temperature distribution in the target area and, as a result, produces lower temperature gradients than the fixed point or thermal dose control strategies. Nevertheless, the temperature and thermal dose evolution for temperature and thermal dose control are comparable. In total, temperature control required 17 s more to achieve the target value in the entire target area. All three control strategies

applied 60 W acoustic power during 109 s. An evaluation of the achieved thermal doses inside and outside the target area at the end of the experiment is shown in Table 6.1. As expected, the fixed point sonication deposits most of the energy in the target area which leads to very high thermal doses in the center of the target area but to relatively low thermal doses in the peripheral voxels compared to temperature or thermal dose control. Here, thermal dose control achieves a slightly higher percentage of voxels above the target thermal dose $\mathrm{TD}_{\mathrm{target}} = 24\,\mathrm{EM}$ than temperature control. On the other hand, the fixed point sonication shows considerably less heating outside the target circle. For this area, temperature control and thermal dose control achieve comparable percentages. The minor differences between the percentages for both control algorithms indicate that temperature control creates a flatter thermal dose distribution than thermal dose control. This leads for the temperature algorithm to a lower percentage of voxels heated above $10^{-1}\,\mathrm{TD}_T$ and TD_T and a larger percentage of voxels having received the lower thermal dose of $10^{-2}\,\mathrm{TD}_T$.

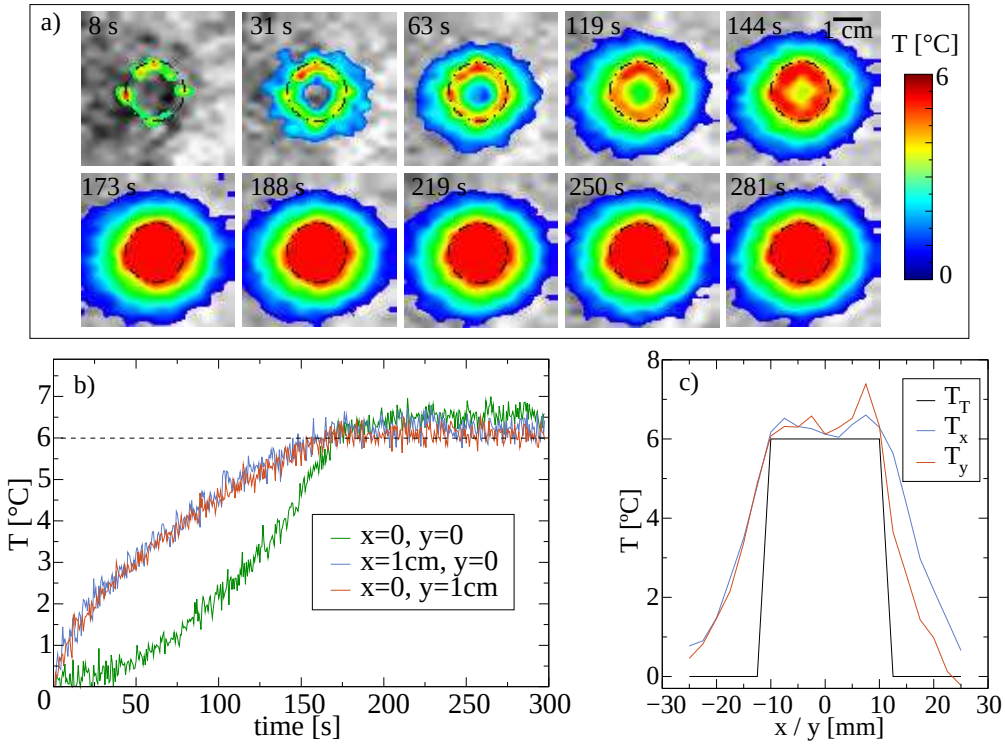

Figure 6.9: Temperature control experiment with target temperature rise of 6 °C. a) Shown are the magnitude images at different time points of the heating experiment with an overlay of the temperature. The circular target area is depicted by a dashed-dotted black circle. b) Temperature profiles in x (blue line) and y (red line) through the center of the target area and the target temperature profile (solid black line). c) Temporal temperature profiles for three different points in the target area. The target temperature is depicted by the black dashed line.

6.3.3 Two-dimensional temperature control: static

A circular area of 2 cm diameter was heated in order to achieve a homogeneous temperature rise of 6 °C. After having achieved the target temperature, it was maintained for 2 min. The evolution of the temperature in the target area for the temperature control experiment with target temperature rise of 6 °C is shown in Fig. 6.9a for different time points as an overlay on the magnitude images. As a result of the introduced weighting, heating starts at the periphery and heating in the central area is mainly accomplished by thermal diffusion. The last images (≥ 173 s) show a homogeneous temperature rise of 6 °C throughout the target area corresponding to a red coloring in the temperature map. The good correspondence between target temperature and measured temperature is visible in the temperature profiles shown in Fig. 6.9b where a maximal error of 1.4 °C for one voxel has been found. Figure 6.9c shows the temporal temperature evolution for three voxels in the target area. The central point shows a temperature error below 1.0 °C once the target temperature is achieved. For the two peripheral points, temperature errors of maximal 0.6 °C have been found.

6.3.4 Two-dimensional thermal dose control: static

A circular area of 2 cm diameter was heated in order to apply a thermal dose of $\mathrm{TD}_T = 24$ EM corresponding to 10 % of the lethal thermal dose in tissue TD_L.
Figure 6.10 shows the thermal dose distribution as a logarithmic overlay on the magnitude images for different time points. The first trajectory points are chosen in the center of the target area and the outer points are heated at last. This strategy leads to

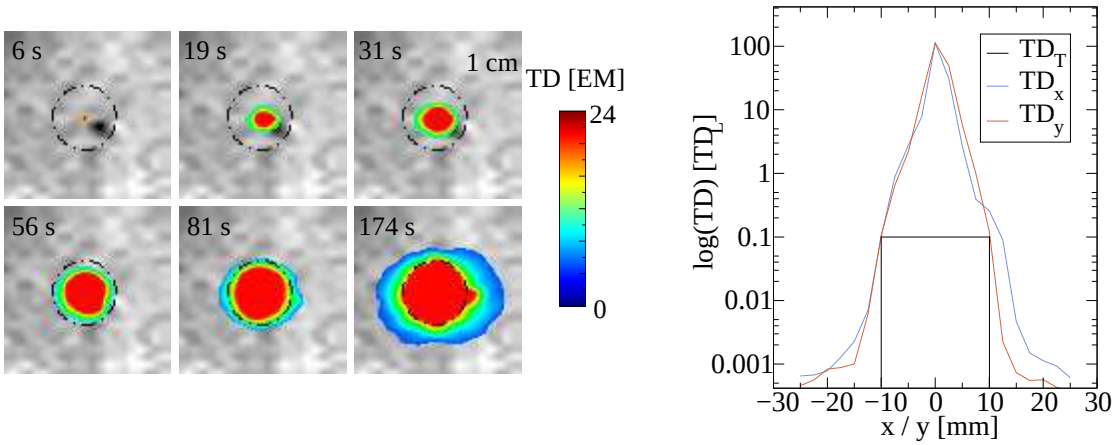

Figure 6.10: Thermal dose control experiment with target thermal dose of 24 EM ($0.1\mathrm{TD}_L$). Left: Shown are the magnitude images at different time points of the heating experiment with a logarithmic overlay of the thermal dose. The circular target area is depicted by a dashed-dotted black circle. Right: Logarithmic thermal dose profiles in x (blue line) and y (red line) through the center of the target area and the target thermal dose profile (black line).

an over-treatment of the inner points as can be seen in the thermal dose profiles on the right hand side. Due to the exponential character of the thermal dose with respect to temperature, the inner points receive a thermal dose which is up to 1000 times larger than the target value $TD_T = 24\,EM$. For this control experiment all points within the target area received a thermal dose $TD \geq TD_T$. In the area around the target circle, one voxel showed a thermal dose above the target value ($TD = 40.8\,EM$). The overall heating time for this experiment was 174 s.

6.3.5 Two-dimensional thermal dose control: with motion

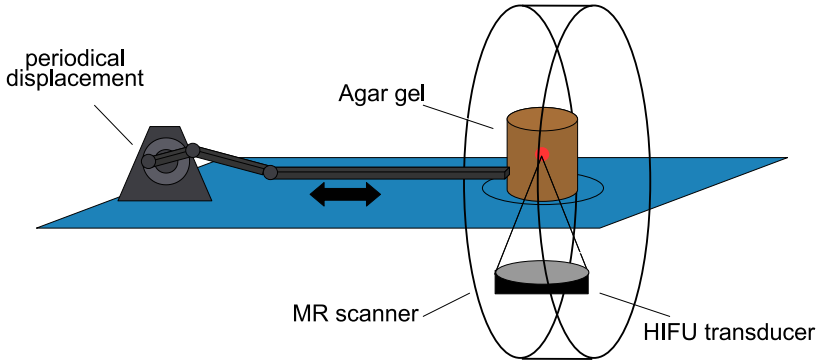

Figure 6.11: Experimental setup for thermal dose and temperature control with simulation of physiological motion.

Physiological motion was simulated by a motorized MR-compatible platform which was attached to the agarose platform to create periodical displacements during the treatment (Fig. 6.11). A circular target area of 15 mm diameter was chosen with a target thermal dose of $TD_T = 24\,EM$. During the treatment, motion amplitudes of 4.5 mm peak-to-peak with a period of 3 s were observed (Fig.6.12c).
Figure 6.12a shows the achieved thermal dose map at the end of the treatment. The resulting thermal dose distribution shows good correspondence with the target area without any motion related effects. All voxels within the target area received a thermal dose $TD \geq TD_T$. Only one voxel outside the target area was heated to that extent ($TD = 41.6\,EM$). The overall heating duration was 88 s.

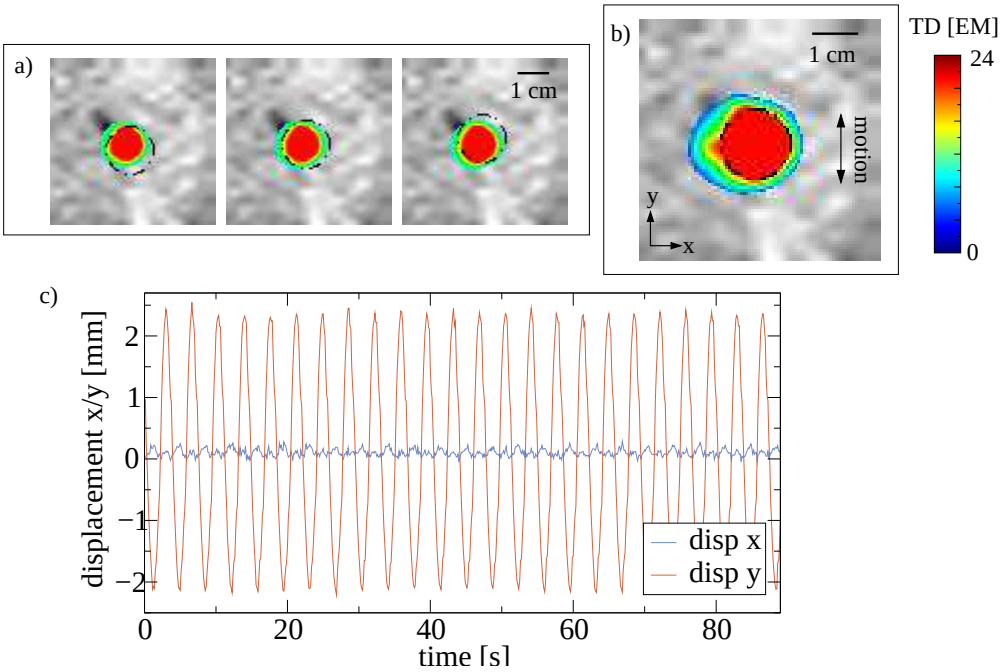

Figure 6.12: 2D thermal dose control experiment with target thermal dose of $\mathrm{TD}_T = 24\,\mathrm{EM}$ ($0.1\mathrm{TD}_L$) and a circular target area of 15 mm diameter. a) Overlays of the thermal dose maps for different points in the motion cycle. The theoretical position of the target area without motion compensation is depicted by the dashed-dotted black circle. b) Thermal dose map at the end of the treatment. The target area is depicted by a black dashed-dotted circle. c) Simulated physiological motion in x and y with a peak-to-peak amplitude of 4.5 mm in y with a period of 3 s.

6.3.6 Three-dimensional thermal dose control

An ellipsoidal target volume (short axis 7.5 mm, long axis 15 mm along the beam axis, 123 voxels) was chosen for thermal dose control with a target value of $\mathrm{TD}_T = 24\,\mathrm{EM}$. Figure 6.13 shows the thermal dose profiles in the three orthogonal planes for four different time points as well as the thermal dose profile at the end of the treatment for the three directions. In order to reduce overheating due to the near-field effect, heating starts in the areas with the largest distance from the transducer surface with a preference of the central voxels of the target ellipsoid. In the radial view (xy), good agreement between the final thermal dose distribution and the target area is visible. Parallel to the beam axis, overheating in adjacent voxels occurred. This is also visible in the thermal dose profile in z which indicates overheating along the beam axis. As a result, 124 voxels outside the target area received a thermal dose above the target value ($\mathrm{TD} = 25.2 - 600.7\,\mathrm{EM}$).

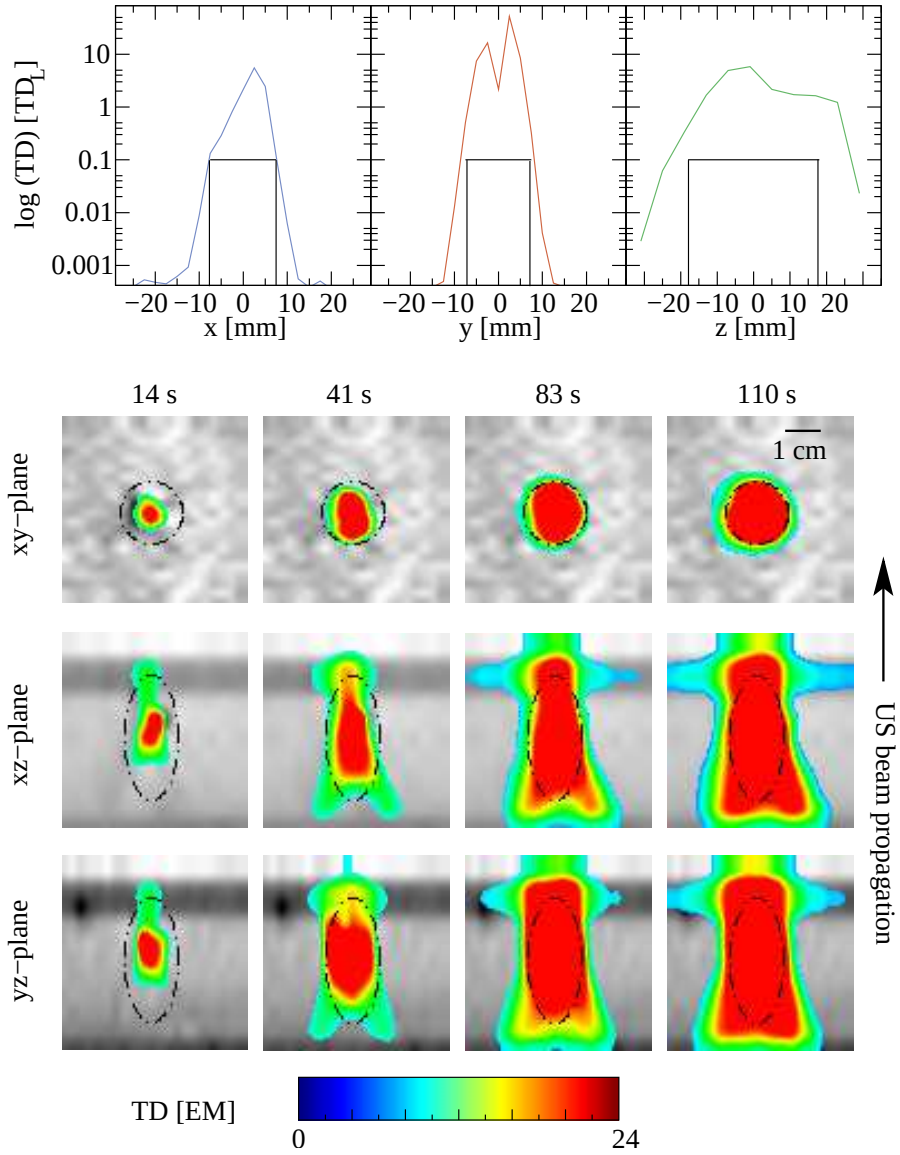

Figure 6.13: 3D thermal dose control experiment with target thermal dose $\mathrm{TD}_T = 24\,\mathrm{EM}$ ($0.1\,\mathrm{TD}_L$) and an ellipsoidal target area of $7.5\,\mathrm{mm} \times 7.5\,\mathrm{mm} \times 15\,\mathrm{mm}$. Top: Thermal dose profiles along x (blue line), y (red line), and z (green line) through the center of the target volume. The target thermal dose TD_T is depicted by a black solid line. Bottom: Color overlay of the thermal dose for different time steps and the xy-plane (first row), xz-plane (second row), and the yz-plane (third row). The borders of the target area are visualized by a black dashed-dotted line.

6.4 Discussion

Choice of control strategy The presented results showed that the choice of the control strategy depends heavily on the application. Temperature control employing inverse radial weighting allows to achieve a homogeneous temperature rise throughout the target volume with minimal temperature overshoots of below 1.4 °C. On the contrary, this strategy leads to longer treatment times and increased heat deposition outside the target area. Consequently, this approach is ideal for applications requiring low homogeneous temperature elevations within the target area, e.g. local drug delivery or gene delivery. The same algorithm using central weighting allows to achieve a pre-defined thermal dose within the target area with high efficiency and minimal damage to the area outside the target volume. A comparison to thermal dose control leads to the following conclusions: Temperature control achieves a slightly more favorable ratio between energy deposited inside and outside the target area. The key advantage of thermal dose control over temperature control lies in the ability to precisely plan the treatment as the target thermal dose is a direct input parameter for the control algorithm. Treatment planning of temperature control can only be based on the equivalent minutes accumulated by maintaining a stable temperature. This approach, however, does not take into account the thermal dose accumulated during the heating process, nor does it consider temperature fluctuations and overshoots during the treatment. Thermal dose control thus allows to achieve a comparable control precision coupled to reliable treatment planning and online adaptation of the treatment parameters. The comparison with a static heating experiment clearly showed that both temperature and thermal dose control are superior if larger target volumes are to be heated. Both methods allow to shorten the treatment time which in return leads to reduced near-field heating and an overall reduction of energy deposition outside the target area.

Volume coverage and 3D control The implementation of a slice sweep made it possible to combine volume coverage with frame rates compatible with the real time constraints of motion compensation and temperature control. As the slice positions covered by the slice sweep can be chosen for each application, volumetric temperature and thermal dose information can be used to monitor the near field or critical areas in the beam path in order to prevent extensive heating. Alternatively, a 3D imaging volume can be constructed using the integrated gridding algorithm. By choosing the displacement $\Delta s < \Delta z$, the principle of superresolution [44] can be used to increase the spatial resolution in the sweep direction.
An example of the feasibility of static 3D control using such 3D volume has been presented and evaluated. It is possible to achieve a pre-defined thermal dose within the 3D target area, but the control precision is reduced compared to 2D control. Deviations are mainly visible along the beam axis as a result of the elongated focal point and the near-field heating which increases with treatment time.

Motion compensation and latency In the presence of periodical displacements comparable to physiological motion, similar precisions for the thermal dose algorithm were

found with no evidence of motion-induced broadening of the heated area. The separation of image processing necessary for real-time beam tracking and the calculations required for temperature monitoring and trajectory optimization led to a lower latency in the adaptation of the beam position. For the current implementation, a refresh-rate of 125 ms was sufficient to reliably follow the periodic motion with period 3 s. A further latency reduction is mainly limited by signal considerations as minimum two slices have to be acquired. The latency for the trajectory optimization mainly depends on the number of slice positions covered by the slice sweep. For 2D control, this delay could be reduced by applying a sweep pattern which oversamples the slice containing the area to be heated with the other slices serving as safety control to prevent overheating in adjacent voxels.

The spherical phased-array transducer used in this work offered only limited possibilities in terms of electronic displacement of the focal point position (± 1.2 cm in x/y and $+1.5/-2.5$ cm along z) coupled to a comparably large focal point size of $\approx 1.2 \times 1.2 \times 8$ mm. For the treatment of larger target volumes, a transducer with a higher ratio of focal length to the size of the single elements may allow to benefit more from the possibilities of volumetric control.

Bibliography

[1] L.A. Zadeh. Fuzzy algorithm. *Informat. Control*, 12(2):94–102, 1968.

[2] C.C. Lee. Fuzzy logic in control systems: Fuzzy logic controller I. *IEEE Trans. Syst., Man, Cybern.*, 20(2):404–418, 1990.

[3] C.C. Lee. Fuzzy logic in control systems: Fuzzy logic controller II. *IEEE Trans. Syst., Man, Cybern.*, 20(2):419–435, 1990.

[4] J. Richalet, A. Rault, J.L. Testud, and J. Papon. Model predictive heuristic control: Applications to industrial processes. *Automatica*, 14(5):413–428, 1978.

[5] K.R. Muske and J.B. Rawlings. Model predictive control with linear models. *AIChE Journal*, 39(2):262–287, 1993.

[6] W.L. Lin, R.B. Roemer, and K. Hynynen. Theoretical and experimental evaluation of a temperature controller for scanned focused ultrasound hyperthermia. *Med. Phys.*, 17(4):615–25, 1990.

[7] J.A. Weinstein, R.L. Margin, M.B. Yatvin, and D.S. Zaharko. Liposomes and local hyperthermia: Selective delivery of methotrexate to heated tumors. *Science*, 204:188–91, 1979.

[8] D. Needham and M.W. Dewhirst. The development and testing of a new temperature-sensitive drug delivery system for the treatment of solid tumors. *Adv. Drug. Deliv. Rev.*, 53(3):285–05, 2001.

[9] R. Deckers, C. Rome, and C.T.W. Moonen. The role of ultrasound and magnetic resonance in local drug delivery. *J. Magn. Res. Im.*, 27(2):400–9, 2008.

[10] D.P. Madio, P. van Gelderen, D. DesPres, A.W. Olson, J.A. de Zwart, T.W. Fawcett, N.J. Holbrook, M. Mandel, and C.T.W. Moonen. On the feasibility of MRI-guided focused ultrasound for local induction of gene expression. *J. Magn. Res. Im.*, 8:101–104, 1998.

[11] R. Deckers, B. Quesson, J. Arsaut, S. Eimer, F. Couillaud, and C.T.W. Moonen. Image-guided, noninvasive, spatiotemporal control of gene expression. *Proc. Natl. Acad. Sci. USA*, 106(4):1175–1180, 2009.

[12] C. Mougenot, B. Quesson, D. Denis de Senneville, P. Laurenço de Oliveira, S.M. Sprinkhuizen, J. Palussière, N. Grenier, and C.T.W. Moonen. Three-dimensional spatial and temporal temperature control with MR thermometry-guided focused ultrasound (MRgHIFU). *Magn. Res. Med.*, 61(3):603–14, 2009.

[13] F.C. Vimeux, J.A. De Zwart, J. Palussière, R. Fawaz, C. Delalande, P. Canioni, N. Grenier, and C.T.W. Moonen. Real-time control of focused ultrasound heating based on rapid MR thermometry. *Invest. Radiol.*, 34(4):190–93, 1999.

[14] C. Mougenot, R. Salomir, J. Palussière, N. Grenier, and C.T.W. Moonen. Automatic spatial and temporal temperature control for MR-guided focused ultrasound using fast 3D MR thermometry and multispiral trajectory of the focal point. *Magn. Res. Med.*, 52(5):1005–1015, 2004.

[15] R. Chopra, K. Tang, M. Burtnyk, A. Boyes, L. Sugar, S. Appu, L. Klotz, and M. Bronskill. Analysis of the spatial and temporal accuracy of heating in the prostate gland using transurethral ultrasound therapy and active MR temperature feedback. *Phys. Med. Biol.*, 54:2615–2633, 2009.

[16] J.G. Hust, J. Filla, and D.R. Smith. A modified digital PID temperature controller for thermal properties measurements. *J. Build. Phys.*, 11:102, 1987.

[17] T. Yucelen, O. Kaymakci, and S. Kurtulan. Adaptive PI-D Controller using Ziegler Nichols based self-tuning method's parameters for programmable logic controllers. In *Proc. 5th Int. Symp. Intell. Manuf. Systems*, volume May 29-31, pages 381–93, 2006.

[18] G.F. Franklin, J.D. Powell, and A. Emami-Naeini. *Feedback Control of Dynamic Systems, 4th edition.* Prentice Hall: Englewood Cliffs, New Jersey, 2002.

[19] D. Hinrichsen and A.J. Pritchard. *Mathematical Systems Theory I - Modelling, State Space Analysis, Stability and Robustness.* Springer, New York, 2005.

[20] B. Davies. *Integral transforms and their applications, 3rd edition).* Springer, New York, 2002.

[21] E.I. Jury. *Sampled-Data Control Systems.* John Wiley & Sons, New York, 1958.

[22] R. Salomir, F.C. Vimeux, J.A. de Zwart, N. Grenier, and C.T.W. Moonen. Hyperthermia by MR-guided focused ultrasound: Accurate temperature control based on fast MRI and a physical model of local energy deposition and heat conduction. *Magn. Res. Med.*, 43:342–47, 2000.

[23] L. Sun, C.M. Collins, J.L. Schiano, M.B. Smith, and N.B. Smith. Adaptive real-time closed-loop temperature control for ultrasound hyperthermia using magnetic resonance thermometry. *Conc. Magn. Res. B*, 27B:51–63, 2005.

[24] N.B. Smith, N.K. Merrilees, K. Hynynen, and M. Dahleh. Control system for an MRI compatible intracavitary ultrasound array for thermal treatment of prostate disease. *Int. J. Hyp.*, 17(3):271–282, 2001.

[25] J. Dragonu, P.Laurenço de Oliveira, C. Laurent, C. Mougenot, N. Grenier, C.T.W. Moonen, and B. Quesson. Non-invasive determination of tissue thermal parameters

from high intensity focused ultrasound treatment monitored by volumetric MRI thermometry. *NMR Biomed.*, 22(8), 2009. 843-851.

[26] D.R. Daum and K. Hynynen. Thermal dose optimization via temporal switching in ultrasound surgery. *IEEE Trans. Ultrason. Ferroelect. Frequ. Contr.*, 43:208–15, 1998.

[27] S.A. Sapareto and W.C. Dewey. Thermal dose determination in cancer therapy. *Int. J. Radiat. Oncol. Biol. Phys.*, 10(6):787–800, 1984.

[28] S. Hey, B. Denis de Senneville, G. Maclair, M.O. Köhler, B. Quesson, C.T.W. Moonen, and M. Ries. Optimization of volumetric MR-guided high-intensity focused ultrasound ablations in moving organs. In *Proc. 17th ISMRM, Hawaii*, 2009. #2539.

[29] S. Hey, B. Denis de Senneville, G. Maclair, M.O. Köhler, B. Quesson, C.T.W. Moonen, and M. Ries. Adaptive volumetric MR-guided high-intensity focused ultrasound ablations in moving organs. In *Proc. of the ISTU 2009, Aix-en-Provence*, 2009. pp. 49-52.

[30] K. Hynynen, R. Roemer, D. Anhalt, C. Johnson, Z.X. Xu, W. Swindell, and T. Cetas. A scanned, focused, multiple transducer ultrasonic system for localized hyperthermia treatments. *Int. J. Hyp.*, 3:21–25, 1987.

[31] W.L. Lin, Y.Y. Chen, S.Y. Lin, J.Y. Yen, M.J. Shieh, and T.S. Kuo. Optimal configuration of multiple-focused ultrasound transducers for external hyperthermia. *Med. Phys.*, 26:2007–16, 1999.

[32] K. Tang, V. Choy, R. Chopra, and M.J. Bronskill. Conformal thermal therapy using planar ultrasound transducers and adaptive closed-loop MR temperature control: Demonstration in gel phantoms and ex vivo tissues. *Phys. Med. Biol.*, 52:2905–19, 2007.

[33] A.M. Kinsey, C.J. Diederich, V. Rieke, W.H. Nau, K. Butts-Pauly, D. Bouley, and G. Sommer. Transurethral ultrasound applicators with dynamic multi-sector control for prostate thermal therapy: In vivo evaluation under MR guidance. *Med. Phys.*, 35(5):2081–93, 2008.

[34] E. Delabrousse, R. Salomir, A. Birer, C. Paquet, F. Mithieux, J.-Y. Chapelon, F. Cotton, and C. Lafon. Automatic temperature control for MR-guided interstitial ultrasound ablation in liver using a percutaneous applicator: Ex vivo and in vivo initial studies. *Magn. Res. Med.*, 63:667–679, 2010.

[35] M.O. Köhler, C. Mougenot, B. Quesson, J. Enholm, B. Le Bail, C. Laurent, C.T.W. Moonen, and G.J. Ehnholm. Volumetric HIFU ablation under 3D guidance of rapid MRI thermometry. *Med. Phys.*, 36(8):3521–3535, 2009.

[36] J. Enholm, M.O. Köhler, B. Quesson, C. Mougenot, C.T.W. Moonen, and S.D. Sokka. Improved volumetric MR-HIFU ablation by robust binary feedback control. *IEEE Trans. Biomed. Eng*, 57(1):103–13, 2010.

[37] O. Seror, M. Lepetit-Coiffé, B. Le Bail, B. Denis de Senneville, H. Trillaud, C.T.W. Moonen, and B. Quesson. Real time monitoring of radiofrequency ablation based on MR thermometry and thermal dose in the pig liver in vivo. *Eur. Radiol.*, 18(2):408–16, 2007.

[38] D. Arora, D. Cooley, T. Perry, M. Skliar, and R.B. Roemer. Direct thermal dose control of constrained focused ultrasound treatments: Phantom and in vivo evaluation. *Magn. Res. Med.*, 50(8):1919–35, 2005.

[39] B. Denis de Senneville, C. Mougenot, and C.T.W. Moonen. Real-time adaptive methods for treatment of mobile organs by MRI-controlled high-intensity focused ultrasound. *Magn. Res. Med.*, 57(2):319–30, 2007.

[40] M. Ries, G. Maclair, B. Denis de Senneville, P. Laurenço de Oliviera, C. Mougenot, E. Vahala, and C.T.W. Moonen. MRI guided focused ultrasound of moving tissues: Accelerated MR-thermometry and motion analysis for subsecond target tracking. In *Proc. 15th Scientific Meeting, ISMRM, Berlin*, page 246, 2007.

[41] M. Ries, B. Denis de Senneville, G. Maclair, M.O. Köhler, B. Quesson, and C. Moonen. Three dimensional motion compensation for real-time MRI guided focused ultrasound treatment of abdominal organs. In *Proc. 17th Scientific Meeting,ISMRM, Honolulu*, page 442, 2009.

[42] S. Roujol, M. Ries, B. Quesson, C.T.W. Moonen, and B. Denis de Senneville. Real-time MR-thermometry and dosimetry for interventional guidance on abdominal organs. *Magn. Res. Med.*, 63(4):1080–7, 2010.

[43] M. Ries, B. Denis de Senneville, and C.T.W. Moonen. Beam steering. *Magn. Res. Med.*, 2010. in press.

[44] H. Greenspan, G. Oz, N. Kiryati, and S. Peled. MRI inter-slice reconstruction using super-resolution. *Magn. Res. Im.*, 20(5):437–46, 2002.

Part IV

Conclusions and Perspectives

MR thermometry in the presence of motion and magnetic field variations

The presented results showed the feasibility of precise PRF MR thermometry for different applications and target organs. For each example, the specific challenges were addressed by adapted phase correction and if necessary motion compensation strategies. Consequently, temperature precisions of 1.4 °C could be achieved on average in the breast of healthy volunteers under free breathing conditions using a model-based phase correction algorithm. For the more complicated case of the ventricular septum in the human heart, temperature stabilities better than 2 °C have been achieved using a model-based phase correction algorithm coupled to an affine motion compensation technique. Advanced phase and motion correction strategies are already being developed and may lead to more robust PRF thermometry in the future. The recently presented hybrid phase correction algorithm discussed in sect. 1.2.3 already benefits from the advantages of referenceless and multi-baseline phase correction together. Furthermore, the applied motion correction can be refined using a combination of local and global motion estimation techniques which may lead to more robust motion compensation. A general issue, which has to be addressed in the future, is the evaluation of the quality of MR thermometry and the used correction techniques. Especially for complex applications like cardiac thermometry, the influences of the different corrections are difficult to separate. Furthermore, a suitable tool to verify the accuracy of motion or phase corrections is still needed in order to assess MR thermometry independent of the applied correction strategies.

The presented results for cardiac thermometry evoke likewise the question whether PRF MR thermometry can benefit from an increased field strength. Of course, according to theory (sect. 1.2.4), several advantages like higher temperature sensitivity, shorter possible echo times, and increased signal are to be expected. However, experiences made at 3 T showed that in most of the cases the benefits did not outweigh the problems encountered due to increased and spatially inhomogeneous magnetic field drift, shortened T_2^* and inhomogeneities of the RF excitation field. What is more, the mentioned limitations require the development of adapted MR thermometry sequences for higher field strengths. As a result, a comparison with MR thermometry at lower field strengths is not straight forward and has not yet been presented in literature.

The application to cardiac thermometry revealed once more the limitations encountered by near-real time MR thermometry. There is still need for improvements in order to increase the signal and to reduce acquisition times. Especially highly-accelerated parallel imaging and inner volume excitation techniques may be a remedy, the latter especially for applications where only a small area containing the hot spot has to be monitored.

Both example applications demonstrated further the potential problems related to blood

flow in the case of the human heart and the presence of fat in the target area for MR thermometry in the breast. The first issue was successfully addressed by evaluating the influence of blood suppression on the temperature stability in the ventricular septum using different blood suppression techniques. The presence of fatty tissue in the breast was treated in two different ways. For this, the potential influence of the temperature dependence of the susceptibility of fat on the local magnetic field and thus the temperature as discussed in sect. 1.2.1, was not considered. First, the traditional approach of avoiding partial volume effects with fat was used by applying fat suppression during MR thermometry. However, as this leads to reduced signal and in general to missing temperature information in large areas of the breast, the second discussion exploited the possibility to use both water-based and fatty tissue for MR thermometry. The developed sequence which allows to simultaneously measure the PRF shift and T_1 has been tested successfully for this purpose. Future work should include an evaluation in vivo or on excised breast tissue containing tumors. The principle of multi-parametric quantitative imaging is also applicable to other application areas as shown for the monitoring of contrast agent release from thermo-sensitive liposomes. Along this line, the acquired temperature and T_1 maps may be combined to improve existing control algorithms in order to achieve the pre-defined release pattern in the target area.
Finally, the underlying sequence may be extended to allow the combination of PRF and T_1 measurements with T_2/T_2^* mapping in the future.

High-precision volumetric temperature control on moving targets

In this work, the specific PID control algorithm used for temperature control during HIFU heating was studied extensively from a stability theory point of view. Even though the combination of a PID controller and the thermal processes in tissue have been treated extensively in literature, the influences of erroneous thermal tissue parameter estimation have not been considered to that extent. The presented adaptive approach incorporated results retrieved from stability analysis in order to improve the stability and the convergence of the controller algorithm. For preliminary studies in gel phantoms, a superior performance compared to a conventional PID controller was found.
The generalization of single-point temperature control consequently led to volumetric heating using a dedicated trajectory optimization strategy. As a result, pre-defined temperature or thermal dose distributions were achieved with high spatial precision and minimal energy deposition and treatment time using a gel phantom. The benefits of the integrated slice sweep were twofold. First, it allows to cover a larger volume without an increase in scan time. The flexible choice of dynamic slice displacements furthermore allows to monitor the temperature in the near field in order to prevent skin burns. Subpixel displacements in the slice encoding direction may also be used to create isotropic voxels using super-resolution. The application for 3D heat control was evaluated and found feasible in the limits of the focal point size and near field heating effects. For this application, a dedicated transducer with a larger ratio of focal length to single element aperture may improve the achievable results. The presented temperature control accuracy suggests as well the application to local drug delivery or gene expression where precise temperature control in a certain target area is required. Here, a combination with the presented adaptive PID controller may further improve the achievable temperature control accuracy.
In the presence of displacements similar to physiological motion, results comparable to those obtained for static experiments were found. Latency was minimized by a dedicated processing pipeline for the position update of the focal point position. For periodical motion, a further latency reduction is imaginable by introducing a certain degree of prediction in the adaptation process using e.g. Kalman filtering. Future work may also explore the possibilities to include the knowledge about periodical displacements into the trajectory optimization in order to achieve larger treatment volumes. The extension to 3D motion compensation using navigator echoes has been presented for single point sonications, but can also be combined with a trajectory optimization algorithm if complex motion patterns have to be corrected. Furthermore, the feasibility of the presented volume control algorithm in vivo still has to be verified. Here, care must be taken if organs like the liver are targeted, as the obstruction of the HIFU beam by the ribs as

well as heterogeneous tissue in the beam path still have to be addressed. Furthermore, the ability to induce necrosis in the target area is still limited by high blood perfusion in organs like the kidney as well as by the risk of subcutaneous burns due to near-field heating.

A Appendix

A.1 Analysis of variance (ANOVA) for statistical evaluation

In cases where different experiments and the corresponding collection of measurements are to be compared for a certain criterion, it is necessary to determine whether observed differences are significant or a result of statistical variances. In general, such a test verifies the null hypothesis that there is no significant difference between the means of the compared groups. This is verified with a pre-defined significance level p. Such an analysis can typically lead to two different types of errors:

- type I error: The null hypothesis is rejected even though it is true.
- type II error: The null hypothesis is not rejected even though it is false.

The following explanations will focus on statistics which follow or can be approximated by a normal distribution.

A.1.1 Student's t-test

In the special case, of two different measurement groups, a Student's t-test [1] can be applied. There are two types of t-tests: dependent (paired) and independent. For the applications discussed in this work, only the independent test was of interest as never exactly the same samples were evaluated. The most general form of an independent t-test assumes that both the sample sizes and their variances are different. The leads to the following t statistic

$$t = \frac{\mu_1 - \mu_2}{\sigma_{\mu_1-\mu_2}} \quad , \tag{A.1}$$

with

$$\sigma_{\mu_1-\mu_2} = \sqrt{\frac{\sigma_1^2}{n_1} + \frac{\sigma_2^2}{n_2}} \quad , \tag{A.2}$$

and degrees of freedom d approximated with the *Welch-Satterthwaite equation* [2, 3]

$$d = \frac{\left(\sigma_1^2/n_1 + \sigma_2^2/n_2\right)^2}{\left(\sigma_1^2/n_1\right)^2/(n_1-1) + \left(\sigma_2^2/n_2\right)^2/(n_2-1)} \quad . \tag{A.3}$$

Here, n_1, n_2 are the two sample sizes, μ_1, μ_2 the sample means, and σ_1, σ_2 the sample standard deviations. The probability density function of the corresponding t distribution is then given by

$$f(t) = \frac{\Gamma\left(\frac{d+1}{2}\right)}{\sqrt{d\pi}\,\Gamma\left(\frac{d}{2}\right)} \left(1 + \frac{t^2}{d}\right)^{-(d+1)/2} \quad , \tag{A.4}$$

where Γ is the Gamma function. For growing d, $f(t)$ approaches a normal distribution.

A.1.2 One way analysis using the F-test

For more than two groups, the multiple application of two-sample t-tests would increase the risk of committing a type I error. In this case, a generalization of the Student's t-test can be applied. The general idea behind analysis of variance is to split the variance σ^2 of all measurements into two separate terms, one originating from inter-group variabilities σ_I^2 and one from within-group variabilities σ_W^2.

$$\begin{aligned}
\sigma^2 &= \sum_{i=1}^{K}\sum_{j=0}^{n_i}\frac{\left(Y_{ij}-\bar{Y}\right)^2}{N} \\
&= \sigma_I^2+\sigma_W^2 \\
&= \sum_{i=1}^{K}\frac{n_i\left(\bar{Y}_i-\bar{Y}\right)^2}{N\left(K-1\right)}+\sum_{i=1}^{K}\sum_{j=0}^{n_i}\frac{\left(Y_{ij}-\bar{Y}_i\right)^2}{\left(N-K\right)} \qquad \text{(A.5)}\\
&\quad Y_{ij}: j^{\text{th}}\,\text{observation in}\,i^{\text{th}}\,\text{out of}\,K\,\text{groups}\\
&\quad \bar{Y}_i: \text{sample mean in}\,i^{\text{th}}\,\text{group}\\
&\quad \bar{Y}: \text{sample mean in group}\,i\\
&\quad n_i: \text{number of samples within group}\,i\\
&\quad K: \text{number of groups}\\
&\quad N: \text{overall sample size}
\end{aligned}$$

The F-statistic is then defined as follows

$$F_{\text{stat}}=\frac{\sigma_I^2}{\sigma_W^2} \quad . \qquad \text{(A.6)}$$

This F statistic follows the F distribution $f(x)$ (Fig. A.1)

$$f(x)=\frac{\sqrt{\dfrac{\left(d_1x\right)^{d_1}\,d_2^{d_2}}{\left(d_1x+d_2\right)^{(}\,d_1+d_2\right)}}}{xB\left(d_1/2,d_2/2\right)} \quad , \qquad \text{(A.7)}$$

with $d_1=(K-1)$ and $d_2=(N-K)$ degrees of freedom under the null hypothesis and the Beta function B.
The probability for the acceptance of the null hypothesis, that means the probability that there is no significant difference between the groups, is then given by

$$p_{\text{stat}}=\int_{F_{\text{stat}}}^{\infty} f(x)\mathrm{d}x \qquad \text{(A.8)}$$

If $p_{\text{stat}}<f(p)$ and the null hypothesis is rejected, additional t-tests between all pairs of groups have to be carried out in order to determine which differences are indeed significant. For the case where $p_{\text{stat}}\geq p$ no further tests are necessary, since the observed differences result from statistical variations of the measurements. In the special case of $K=2$, the F-test and the t-test are equivalent and $F=t^2$.

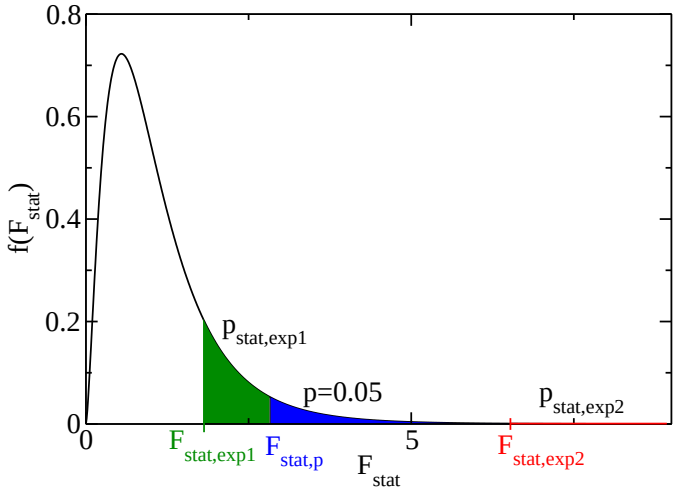

Figure A.1: F distribution of the F statistic for $d_1 = 5$, $d_2 = 20$. The probabilities are given by the integral over the distribution function. If a significance of $p = 0.05$ is applied, the null hypothesis will be rejected for the first example ($F_{\mathrm{stat,exp1}}$) and accepted for the second example ($F_{\mathrm{stat,exp2}}$).

A.1.3 Bonferroni correction

If multiple comparisons are applied to a set of data, the risk of committing a type I error increases with the number of tested hypothesis n. For this reason, it was proposed to test each hypothesis with a significance level reduced by the factor $1/n$ in order to correct for this effect [4, 5]. While this correction reduces the risk of a type I error, the probability of committing a type II error may increase.

A.2 Stability theory

A.2.1 Poles and zeros of the transfer function

For a general transfer function of the form

$$H(s) = \frac{N(s)}{D(s)} \quad , \tag{A.9}$$

with $N(s)$ and $D(s)$ polynomials of the order m and n ($m \leq n$), the zeros are defined as the values of s_z for which $N(s_z) = 0$ and the poles s_p fulfill the relation $D(s_p) = 0$. The evaluation of both allows to draw conclusions about the stability of the system as its output approaches zero for $s \to s_z$ and infinity for $s \to s_p$. In order to characterize the input response in the time domain with the poles of the transfer function, $H(s)$ is

factorized as follows

$$\begin{aligned} H(s) &= \frac{N(s)}{(s-s_{p1})(s-s_{p2})\dots(s+s_{pn})} \\ &= \frac{a_1}{(s-s_{p1})} + \frac{a_2}{(s-s_{p2})} + \cdots + \frac{a_n}{(s-s_{pn})} \quad . \end{aligned} \tag{A.10}$$

The impulse response $h(t) = \mathcal{L}\{H(s)\}$ can then be found by using the relation $\mathcal{L}\left\{\frac{1}{s-\alpha}\right\} = \mathrm{e}^{\alpha t}u(t)$ with the Heavyside step function $u(t)$

$$h(t) = a_1\mathrm{e}^{s_{p1}t}u(t) + a_2\mathrm{e}^{s_{p2}t}u(t) + \cdots + a_n\mathrm{e}^{s_{pn}t}u(t) \quad . \tag{A.11}$$

As s is a complex value, this expression can be rewritten using the decomposition $s_{pn} = \sigma_n + i\omega_n$

$$h(t) = a_1\mathrm{e}^{\sigma_1 t}\left(\cos\omega_1 t + i\sin\omega_1 t\right)u(t) + \cdots + a_n\mathrm{e}^{\sigma_n t}\left(\cos\omega_n t + i\sin\omega_n t\right)u(t) \quad . \tag{A.12}$$

Consequently, the response of the system is influenced by the real and imaginary parts of the poles:

- $\omega_n \neq 0$: the response of the pole is oscillating.
- $\sigma_n < 0$: the response of the pole shows an exponential decay.
- $\sigma_n > 0$: the response of the pole shows an exponential rise.

Thus, the output remains absolutely integrable and fulfills the criterion for BIBO stability if

$$Re(s_{pn}) = \sigma_n < 0 \quad \forall n \quad . \tag{A.13}$$

Furthermore, since oscillations sould be avoided,

$$Im(s_{pn}) = 0 \quad \forall n \quad , \tag{A.14}$$

is desirable.

A.2.2 Stability of a simple PID feedback controller

The closed-loop transfer function of this system was derived as (eq. (5.15))

$$H(s) = \frac{T_m(s)}{\theta(s)} = \frac{G_T(s)G_P(s)}{1 + G_S(s)G_T(s)G_p(s)} \quad .$$

Using eq. (5.8,5.11) and $G_S = 1$ it follows

$$H(s) = \frac{\alpha\left(K_P s + K_I + K_D s^2\right)}{1 + \alpha\left(K_P s + K_I + K_D s^2\right)} \quad . \tag{A.15}$$

The poles s_p of $H(s)$ can be found as the zeros of the denominator

$$\begin{aligned} 0 &= 1 + \alpha \left(K_P s_p + K_I + K_D s_p^2 \right) \\ &= \left(1 + \alpha K_D\right) s_p^2 + \alpha K_P s_p + \alpha K_I \\ &= s_p^2 + \underbrace{\frac{\alpha K_P}{1 + \alpha K_D}}_{p} s_p + \underbrace{\frac{\alpha K_I}{1 + \alpha K_D}}_{q} \end{aligned} \tag{A.16}$$

Consequently, the poles are given by

$$s_{p1/2} = -\frac{p}{2} \pm \sqrt{\frac{p^2}{4} - q} = -\frac{1}{2} \frac{\alpha K_P}{(1 + \alpha K_D)} \pm \underbrace{\sqrt{\frac{1}{4} \frac{(\alpha K_P)^2}{(1 + \alpha K_D)^2} - \frac{\alpha K_I}{1 + \alpha K_D}}}_{\sqrt{D}} \tag{A.17}$$

For convergence without oscillations (eq. (A.14)), the term under the root has to be positive

$$\frac{1}{4} \left(\frac{\alpha K_P}{1 + \alpha K_D} \right)^2 \geq \frac{\alpha K_I}{1 + \alpha K_D} \quad . \tag{A.18}$$

BIBO stability on the other hand requires the relation

$$Re(s_{p1/2}) < 0 \quad , \tag{A.19}$$

has to be fulfilled (eq. (A.13). In order to evaluate this condition, two different cases have to be examined:

- $\frac{p^2}{4} - q > 0$: $\quad Re(s_{p1/2}) = -\frac{p}{2} \pm \sqrt{\frac{p^2}{4} - q}$

$$\begin{aligned} K_I,\, K_P,\, K_D,\, \alpha \geq 0 \;\Rightarrow\; p,\, q \geq 0 \quad &\Rightarrow \quad \frac{p^2}{4} - q < \frac{p^2}{4} \\ &\Rightarrow \quad \sqrt{\frac{p^2}{4} - q} < \frac{p}{2} \end{aligned}$$

$$\Longrightarrow\; Re(s_{p1/2}) < 0$$

- $\frac{p^2}{4} - q < 0$: $\quad Re(s_{p1/2}) = -\frac{p}{2}$

$$p \geq 0 \;\Longrightarrow\; Re(s_{p1/2}) < 0$$

It follows that $Re(s_{p1/2}) < 0$ for all values of K_I, K_P, K_D and α.

A.2.3 Stability of the modified PID feedback controller

The closed-loop transfer function of the modified PID feedback loop is defined as (eq. (5.36))

$$\begin{aligned} H(s) &= \frac{G_{TM}}{G_{AS} + G_{PM} G_{TM} G_S} \\ &= \frac{K_P s + K_I + K_D s^2}{K_P s + K_I + \frac{\alpha_s}{\alpha} K_D \left(s^2 + Bs\right) - K_D B_s s} \quad . \end{aligned}$$

The poles s_p are found by evaluating the zeros of the denominator

$$\begin{aligned} 0 &= K_P s_p + K_I + \frac{\alpha_s}{\alpha} K_D \left(s_p^2 + B s_p\right) - K_D B_s s_p \\ &= \frac{\alpha_s}{\alpha} K_D s_p^2 + \left(K_P + \frac{\alpha_s}{\alpha} K_D B - K_D B_s\right) s_p + K_I \\ &= s_p^2 + \underbrace{\left(\frac{\alpha}{\alpha_s}\frac{K_P}{K_D} + B - \frac{\alpha}{\alpha_s} B_s\right)}_{p} s_p + \underbrace{\frac{\alpha}{\alpha_s}\frac{K_I}{K_D}}_{q} \quad , \end{aligned} \tag{A.20}$$

leading to the following expression for the poles of the closed-loop transfer function

$$\begin{aligned} s_{p1/2} &= -\frac{p}{2} \pm \sqrt{\frac{p^2}{4} - q} \\ &= -\frac{1}{2}\left(\frac{\alpha}{\alpha_s}\frac{K_P}{K_D} + \left(B - \frac{\alpha}{\alpha_s} B_s\right)\right) \\ &\quad \pm \sqrt{\frac{1}{4}\left(\frac{\alpha}{\alpha_s}\frac{K_P}{K_D} + \left(B - \frac{\alpha}{\alpha_s} B_s\right)\right)^2 - \frac{\alpha}{\alpha_s}\frac{K_I}{K_D}} \quad , \end{aligned}$$

Again, it is now possible to evaluate the conditions which have to be fulfilled to ensure convergence without oscillations (eq. (A.14))

$$\begin{aligned} Im(s_{p1/2}) = 0 \quad &\Longrightarrow \quad \frac{p^2}{4} - q \geq 0 \\ &\Longrightarrow \quad \frac{1}{4}\left(\frac{\alpha}{\alpha_s}\frac{K_P}{K_D} + \left(B - \frac{\alpha}{\alpha_s} B_s\right)\right)^2 \geq \frac{\alpha}{\alpha_s}\frac{K_I}{K_D} \end{aligned} \tag{A.21}$$

Furthermore, the convergence is stable if $Re(s_{p1/2}) < 0$ (eq. (A.13)). This is ensured for all parameters if

$$-\frac{1}{2}\left(\frac{\alpha}{\alpha_s}\frac{K_P}{K_D} + \left(B - \frac{\alpha}{\alpha_s} B_s\right)\right) < 0 \quad . \tag{A.22}$$

The only term, which can cause a violation of this condition is $\frac{\alpha}{\alpha_s} B_s$. Consequently, assuming $B_s = 0$ increases the stability of the system and does not interfere with the condition in eq. (A.21))

Bibliography

[1] Student. The Probable Error of a Mean. *Biometrika*, 6(1):1–25, 1908.

[2] F.E. Satterthwaite. An Approximate Distribution of Estimates of Variance Components. *Biometr. Bull.*, 2:110–4, 1946.

[3] B.L. Welch. The generalization of "student's" problem when several different population variances are involved. *Biometrika*, 34:28–35, 1947.

[4] C.E. Bonferroni. Il calcolo delle assicurazioni su gruppi di teste. In *In Studi in Onore del Professore Salvatore Ortu Carboni, Rome, Italy*, pages 13–60, 1935.

[5] J.P. Shaffer. Multiple Hypothesis Testing. *Ann. Rev. Psych.*, 46:561–84, 1995.

Publications

Articles

- Online correction of respiratory-induced field disturbances for continuous MR-thermometry in the breast. S. Hey, G. Maclair, B. Denis de Senneville, M. Lepetit-Coiffé, Y. Berber, M.O. Köhler, B. Quesson, C.T.W. Moonen and M. Ries. *Magn. Res. Med.*, 61(6):1494-99, 2009
- Simultaneous T1 measurements and proton resonance frequency shift based thermometry using variable flip angles. S. Hey, M. de Smet, C. Stehning, H. Grüll, J. Keupp, C.T.W. Moonen and M. Ries.*Magn. Res. Med.*, under review
- Towards Optimized MR Thermometry of the Human Heart at 3T. S. Hey, A. Cernicanu, B. Denis de Senneville, S. Roujol, M. Ries, P. Jaïs, C.T.W. Moonen and B. Quesson. *NMR Biomed.*, under review
- Online temperature control of focused ultrasound heating using an adaptive PID feedback loop. S. Hey, P. Lourenço de Oliveira, C.T.W. Moonen, M. Ries. *IEEE Trans. Ultrason., Ferroelecttr. Frequ. Contr.*, submitted

Conferences

- Real-Time Correction of Respiratory-Induced Field Disturbances for PRFS-Based MR-Thermometry in the Human Breast. S. Hey, G. Maclair, B. Denis de Senneville, Y. Berber, B. Quesson, C.T.W. Moonen and M. Ries. In *Proc. 16th ISMRM, Toronto*, 2008. p. 198
- Optimization of volumetric MR-guided high-intensity focused ultrasound ablations in moving organs. S. Hey, B. Denis de Senneville, G. Maclair, M.O. Köhler, B. Quesson, C.T.W. Moonen and M. Ries. In *Proc. 17th ISMRM, Hawaii*, 2009. poster #2539
- Adaptive volumetric MR-guided high-intensity focused ultrasound ablations in moving organs. S. Hey, B. Denis de Senneville, G. Maclair, M.O. Köhler, B. Quesson, C.T.W. Moonen and M. Ries. In *Proc. of the ISTU 2009, Aix-en-Provence*, 2009. pp. 49-52
- Feasibility of MR-thermometry with blood suppression on the human heart at 3T. S. Hey, A. Cernicanu, B. Denis de Senneville, S. Roujol, M. Ries, C.T.W. Moonen and B. Quesson. In *Proc. 18th ISMRM, Stockholm*, 2010. oral pres. #289

Acknowledgements

The successful completion of this thesis was only possible with the support of several people and organisations which I would like to acknowledge in the following. I would like to stress that all mentioned contributions were of similar value for me regardless of the order of appearance.

First of all, this thesis would not have been possible without the support of Chrit Moonen who accepted me as a PhD student in the first place. While managing the lab, he was always available for discussions and gave more than once valuable advices based on his scientific experience. For all projects dealing with motion and phase corrections Baudouin de Senneville, Sébastien Roujol and Gregory Maclair provided the necessary background and developments which where the basis for the results presented in this thesis. All projects related to HIFU and temperature control would not have been possible without the often time-demanding technical support of Charles Mougenot and his experience in this field. During the project dealing with cardiac thermometry, Bruno Quesson and Alexandru Cernicanu spent a lot of time during sequence optimization, volunteer experiments and the correction of the final publication for which I am very grateful. For the majority of the work presented in this thesis, Mario Ries was the driving force who was always available for a kick in the right direction, good advice for the implementation of the experiments and expertise on almost all subjects. When it came to code implementation, Yasmina Berber was always a patient listener and got never tired of explaining things. In addition she kept the necessary overview over the whole project including the well-intentioned advices what proper C++ coding should look like.

Of course, I also have to thank all the people in the lab for their support and for creating this very friendly atmosphere in which it was a pleasure to work. The organized "outdoor" activities but also every friendly chat during the week made me feel like home in Bordeaux.

I would also like to acknowledge the technical and scientific support, the lab and thus me received from the people of Philips and the contribution of Philips Healthcare France which allowed financing my thesis.

Finally, I would like to thank Gerald for his patience during long phone calls and to give me a reason to finish my thesis as fast as possible, and my mother for always believing in me and for supporting every crazy thing I wanted to do in my life.